University of Warsaw
Faculty of Physics

Tomasz Kardaś

Time-resolved studies of vibronic and vibrational transitions in complex media

PhD thesis in Physics performed in Department of Chemistry, University of Warsaw

Supervisor

dr hab. Bożena Gadomska

Laboratory of Physicochemistry of Dielectrics and Magnetics
Department of Chemistry
University of Warsaw

Warsaw, July 2014

Project operated within the Foundation for Polish Science MPD Programme MPD/2008/1 "International Scholarship Program for Graduate Studies in the Faculty of Chemistry University of Warsaw" co-financed by the EU European Regional Development Fund. Financial support from the PhD grant number N N204 116539 is gratefully acknowledged.

Abstract

The subject of the present dissertation concerns the vibronic and vibrational transitions, generated in complex media by interaction with the ultrashort light pulses. The phenomenon, which always accompanies this interaction is the Impulsive Stimulated Raman Scattering. Two experiments, visualizing this process in different media, have been designed and performed. Herewith their results along with the interpretation are presented. The first experiment depends on the supercontiuum generation in diamond crystal. The sample is subjected to highly intense off-resonant light pulses. It is known that the self-phase modulation, self-steepening and interaction with photoionized free carriers are processes, which play the main role in the supercontinuum generation. In the present thesis the influence of the intrapulse stimulated Raman scattering on the evolution of the pulse in time and space is investigated. It has been found that the crystal lattice vibrations only weekly affect the pulse spectrum, yet the change is observed and discussed in dependence of the pulse fluence. It manifests itself mainly by a peak lying apart from the central pulse frequency at a distance equal to the vibrational frequency of the diamond crystal. The interpretation of the experimental results is supported by numerical simulation. For this purpose the three dimensional nonlinear envelope equation is solved with the split-step Fourier method. The model includes the effects of refractive index dispersion, diffraction, self-phase modulation and its saturation, self-steepening, photoionization, interaction with free-carriers and stimulated Raman scattering. The results of modeling agree well with the experimental observations.

The second experiment concerns the Time-Resolved Femtosecond Stimulated Raman Scattering studies of the trans-β-apo-8'-carotenal molecule. The experimental setup has been constructed for this purpose. The time resolution of the setup is better than 100 fs and the frequency resolution is about 25 cm^{-1}. The trans-β-apo-8'-carotenal molecule was excited electronically to the S_2 state and its relaxation, through S_1 state to the ground state was observed by measuring the FSRS spectra of the C=C symmetrical stretching vibration. The Raman line corresponding to S_2 state decays within 120 fs after excitation, then a long living line at the frequency corresponding to the optically forbidden S_1 state appears. During the first 500 fs this line is negative, which is attributed to the transient vibrational inversion of population in S_1 electronic level. Later the line becomes positive and then it decays with the lifetime of S_1 level. At the same time the frequency of the

line up-shifts. The theoretical model, describing the dynamics of the molecular system, has been created in quantum mechanical approach based on the formalism of projection operators. The results of the experiment are analyzed by comparison with the time resolved signal obtained from theoretical calculations. It is shown that the predictions of the numerical model agree well with the experimental results. The main conclusion of the present thesis is, that no additional electronic level (apart of S_0, S_1 and S_2) is required for explanation of the experimentally observed decay of the excited S_2 state, instead the existence of a set of vibrational sublevels of the S_1 state has been proposed to take part in its energy redistribution.

Streszczenie

W niniejszej dysertacji zostały przedstawione wyniki badań nad przejściami między stanami wibracyjnymi i wibracyjno-elektronowymi (wibronowymi) w materii skondensowanej, wywołanymi oddziaływaniem z ultrakrótkimi impulsami światła. Procesem nierozerwalnie towarzyszącym tym oddziaływaniom jest Impulsowe Wymuszone Rozpraszanie Ramana. W celu zilustrowania różnych aspektów tego procesu zaprojektowano i przeprowadzono dwa eksperymenty oraz zaprezentowano dyskusję ich wyników. Pierwszy eksperyment dotyczy generacji superkontinuum w krysztale diamentu, na który pada ciąg impulsów laserowych o dużej energii. Wiadomo, że głównymi procesami odpowiedzialnymi za to zjawisko w kryształach są samomodulacja fazy, samostromienie impulsu oraz oddziaływanie z ładunkami powstałymi w wyniku fotojonizacji. Celem pierwszego eksperymentu jest zbadanie wpływu Impulsowego Wymuszonego Rozpraszania Ramana na ewolucję impulsu w czasie i przestrzeni w trakcie propagacji w silnie nieliniowym krysztale. Zaobserwowano, że wpływ drgań sieci krystalicznej na widmo impulsu jest niewielki, niemniej występuje i silnie zależy od energii impulsu. W widmie impulsu pojawia się pik odległy od centralnej częstości impulsu o częstość równą częstości drgań własnych diamentu. Interpretacja wyników eksperymentalnych jest wsparta wynikami symulacji numerycznej. Rozwiązano trójwymiarowe "nieliniowe równanie obwiedni" przy pomocy Fourierowskiej metody małych kroków. Model uwzględnia efekty dyspersji współczynnika załamania, dyfrakcję, samomodulację oraz jej nasycenie, samostromienie impulsu, fotojonizację, interakcję z wolnymi nośnikami oraz wymuszone rozpraszanie Ramana. Wyniki modelowania zgadzają się dobrze z wynikami pomiarów.

Drugi eksperyment dotyczył badania przejść wibronowych w cząsteczce trans-β-apo-8'-karotenu przy pomocy czasowo-rozdzielczego, femtosekundowego, wymuszonego rozpraszania Ramana (CR-FWRR). Do tego celu zbudowano układ pomiarowy o rozdzielczości czasowej 100 fs i rozdzielczości spektralnej około 25 cm^{-1}. Cząsteczka trans-β-apo-8'-karotenu była wzbudzana do elektronowego stanu S_2 a jej relaksację poprzez stan S_1 do stanu podstawowego obserwowano rejestrując widma FWRR symetrycznych, rozciągających drgań wiązania C=C. Linia ramanowska odpowiadająca drganiom cząsteczki, będącej we wzbudzonym stanie elektronowym S_2, zanika w czasie 120 fs po wzbudzeniu, następnie pojawia się linia długo żyjącego stanu S_1. Zaobserwowano, że podczas pierwszych 500 fs linia ta jest

ujemna, co zinterpretowano jako przejaw przejściowej inwersji obsadzeń stanów wibracyjnych w elektronowym stanie S_1. Następnie linia staje się dodatnia i dalej zanika w czasie równym czasowi życia poziomu S_1. Jednocześnie częstość linii wzrasta. Aby opisać dynamikę tego procesu stworzono model teoretyczny, przy czym cząsteczkę opisano w obrazie kwantowym za pomocą równań Heisenberga-Langevina, używając formalizmu operatorów rzutowych. Wyniki doświadczenia przeanalizowano poprzez porównanie z wynikami obliczeń teoretycznych. Pokazano, że przewidywania modeli numerycznych są w zgodności z wynikami pomiarów. Wykazano, że do wyjaśnienia wyników doświadczalnych nie było potrzebne wprowadzenie dodatkowych poziomów elektronowych (innych niż S_0, S_1 i S_2). Udowodniono, że istnienie podpoziomów wibracyjnych stanu elektronowego S_1 jest konieczne do wyjaśnienia redystrybucji energii ze wzbudzonego stanu S_2.

Contents

Acknowledgments

I direct many thanks to the Foundation for Polish Science and prof. Renata Bilewicz, the supervisor of the MPD Programme, for the great opportunity of conducting this interesting studies.

I would like to express my sincere appreciation to all those who have assisted me during preparing and writing this thesis. First, I would like to thank my supervisor, dr hab. Bożena Gadomska, who was supportive, trusted in my abilities and has given me the freedom to pursue various projects. Her enthusiastic support, in particular suggesting the line of work and fruitful discussions were very helpful during my studies. Especially the theoretical part of this work could not have been created without the help of my supervisor.

The experiments discussed in this thesis were performed in Italy, however during my studies I constructed a time-resolved reflection/transmission setup, and I studied the dynamics of the extended cavity Ti:sapphire oscillator. During those experiments the help of the head of the laboratory Prof. Wojciech Gadomski was essential. I would like to thank him for his constructive suggestions and for the sense of humor which could lighten the atmosphere in moments of experimental crises.

I want to extend my gratitude to prof. Roberto Righini, the head of the laboratory and my supervisor at LENS in Florence, who enabled me to realize experimental part of the thesis. He was always ready to help with solving the experimental and theoretical problems.

The contribution of my Italian Laboratory colleague doctor Andrea Lapini cannot be underestimated. He was very helpful at the stage of development of the TR-FSRS setup and with interpretation of the first experimental

results. Andrea was always ready to help on the scientific and engineering field and also, with sometimes very prosaic, administrative problems. I also extend my acknowledge to other members of LENS group: Elena Ragnoni, who has taken over the TR-FSRS setup after the end of my apprenticeship and who has confirmed my experimental results, professor Paolo Foggi and doctor Mariangela Di Donato for their valuable comments on the interpretation of the results of the TR-FSRS data of analyzed molecule.

I could always count on support of Kamil Polok and Piotr Piątkowski, my laboratory mates in the Chemistry department. I will always remember the great atmosphere created by them within this group. I also thank Jadwiga Konarska who took over my freshly created time-resolved reflection/transmission setup.

The detector for the TR-FSRS setup in Florence was constructed by Prof. Marco Prevederli. The chopper system for the TR-FSRS setup benefited from the work of the electronic (Marco De Pas and Alessio Montori) and mechanical (Riccardo Ballerini) workshop at LENS.

I also thank Paulina Matuszewska and Anna Łapińska for MPD Programme administration on the University side, there was never a problem which could not be easily solved.

Chapter 1

Introduction

1.1 Motivation

Molecules and atoms in crystal latices oscillate and their particular characteristic vibrations depend on the structure of crystals or molecules. Light of ultrashort, spectrally broad pulses propagating in such media can be coupled with molecular and crystal lattice vibrations. In presence of light with two frequency components, if the frequency difference of these two components is equal to the vibrational frequency of the medium, the energy can flow from one of the frequency components to another, with simultaneous excitation of the appropriate vibration. This is the Stimulated Raman Scattering (SRS), observed [1] and described theoretically [2] for the first time more than 50 years ago. In the case when short pulses with broad spectra are used, many pairs of such components exist in the pulse spectrum and thus the whole spectrum of the pulse evolves during propagation in the medium. This phenomenon is the Impulsive Stimulated Raman Scattering

(ISRS). ISRS has been demonstrated [3] and described theoretically [4] in 1985. There is no laser intensity threshold for ISRS [4], thus, modification of spectrum of broadband pulses, due to ISRS, is inevitable. Therefore, it has to be considered along with other processes occurring in complex media whenever short pulses are used. The motivation of the present dissertation is to study the role of ISRS process in the interaction of ultrashort light pulses with complex media. Two experiments along with interpretation of their results will be presented. In the first experiment the simple crystal of high third order nonlinearity, subjected to highly intense off-resonant light pulses, is considered in order to estimate the influence of ISRS on the evolution of the pulse shape propagating in the medium. The second experiment concerns the resonant interaction of two ultrashort pulses, with frequency difference close to the vibrational frequency of the medium, with a complex molecular liquid. In this case the ISRS process becomes the tool for time-resolved technique to get the information on vibrational population dynamics in molecules.

Evolution of the pulse in time and space and the way, in which the medium shapes the pulse spectrum through ISRS, is the subject of the first experiment. It is the generation of supercontinuum by focusing of intense utrashort pulses in a bulk diamond crystal. The interaction of light with the medium vibrations is only one of many phenomena involved in this extreme process and it is certainly not a dominating one. During the supercontinuum generation the strong and short laser pulse is shaped by nonlinear effects due to almost instantaneous electronic response of the medium. This leads to a class of effects known as self-phase modulation and its spatial manifestation – self-focusing; self-steepening and saturation of self-phase modulation. As

the intensity of the self-focused beam becomes high, the photoionization of the medium occurs. Some part of the light is absorbed and the rest interacts with newly created free currents. As the effect the spectrum of the pulse becomes extremely broad. A pulse with a broad spectrum can enhance crystal vibrations efficiently by means of ISRS and in return the vibrations can influence the shape of the pulse.

In studies of such a complex phenomenon it is difficult to say what is the contribution of the particular process. Moreover, a few processes can cause similar effects and thus it is difficult to distinguish which one is more important. Thus a question arises: do the crystal vibrations influence the supercontinuum generation process significantly? It might seem that this influence is small and, in fact, the ISRS is often neglected in simulations of the supercontinuum generation. The study presented here is aimed to check the validity of this assumption. Therefore, a supercontinuum generation in a special medium: diamond, with its extreme Raman gain is performed. It is shown that the vibrations influence the generation process weakly, yet, in the case of diamond this influence, can be observed.

The second experiment discussed in the present dissertation applies pump-probe technique, a typical time-resolved spectroscopy scheme, to study the vibrational spectra after vibronic excitation of complex molecules of trans-β-apo-8$'$-carotenal. The technique is the Time-Resolved Femtosecond Stimulated Raman Scattering (TR-FSRS). The lifetimes and vibrational frequencies corresponding to particular electronic levels can be obtained with this technique with a great time and frequency resolution. Moreover, the information on paths of excitation energy redistribution within the system

can be gained. A TR-FSRS setup was constructed for the purpose of this thesis.

Trans-β-apo-8$'$-carotenal is one of carotenoids, a family of molecules which take important part in photosynthesis process. Carotenoids are quite complex, during last 40 years the presence of two so called "dark states", optical excitation of which is strongly forbidden, were discovered in between the ground and the first optically allowed state. One of them is known to take part in the relaxation process of the molecule, the role of the other is not obvious for trans-β-apo-8$'$-carotenal. At least one additional, yet not confirmed, "dark state", together with a triplet state awaits in a line to complicate the picture. Thus, TR-FSRS seems to be a perfect tool for solving carotenoid mysteries and it's application for this purpose is described here. Moreover, to explain the experimental results obtained for trans-β-apo-8$'$-carotenal with the TR-FSRS setup, a quantum mechanical model was constructed and solved numerically. The involvement of only one of the "dark" electronic states with a set of its vibrational sublevels is proved here to be sufficient for explanation of the energy transfer in the molecule. An interesting phenomenon of transient vibrational inversion of population, which is believed to be present during the excited molecule relaxation, is also discussed.

1.2 Thesis outline

The dissertation is organized as follows. In the present introductory chapter a basic classical theory of Impulsive Stimulated Raman Scattering is pre-

sented in the section "Classical theory of coupling of light with molecular vibrations". First the problem of interaction of a single molecule with the electric field of light pulse is formulated in terms of a harmonic oscillator picture. The general solution for arbitrary light intensity time profile is expressed by use of Green's function. Next the formula for nonlinear polarization due to light interaction with vibrating medium is presented. Finally some simple examples of ISRS are discussed.

The Stimulated Raman Scattering in supercontinuum generation in diamond is described in chapter 2. In the introductory part the history of studies on supercontinuum generation in different media is briefly described and the motivation for the current study is argued. Next, the simple experimental arrangement for supercontinuum generation studies is described. Experimental results for a range of input pulse energies are presented, together with a peak emerging at a frequency shifted from the main spectral feature of the supercontinuum by the vibrational frequency of diamond. Next, a model of supercontinuum generation is described. First a brief review of master equations used in models of propagation of short laser pulses is presented. Next the derivation of Nonlinear Envelope Equation used herewith as a master equation and the assumptions validating it are described. The terms corresponding to different effects: material refractive index dispersion, self-phase modulation and it's saturation, ISRS and interaction with the free current are described. Next the symmetrical split step Fourier method with adaptive step size controle used for solution of the master equation is explained. The details on discretization of the pulse envelope, evaluation of linear and nonlinear parts of the master equation and error estimation are described to-

gether with the way, in which the equation of free current density is solved, the implementation details and model testing. Finally the results of modeling of supercontinuum generation in diamond crystal are presented. The good correspondence with experiment results is emphasized. The Raman feature is reproduced in the model. Next the pulse evolution during the propagation, the value of self-focusing saturation and the presence of chirp and intensity dependent fringes in supercontinuum spectrum are discussed. The chapter ends with "Conclusions" section.

Intramolecular vibrational relaxation and transient vibrational inversion of population in trans-β-apo-8'-carotenal is the subject of the third chapter. The history of studies and current state of knowledge on carotenoid molecules is briefly discussed in the introductory part of the chapter. It is followed by the description of the Time-Resolved Femtosecond Stimulated Raman Scattering technique, used in present thesis. Next the TR-FSRS setup constructed by the author in European Laboratory for Nonlinear Spectroscopy is described. The probe and reference, actinic and Raman pump pulse paths through the setup are presented together with the method of detection and data acquisition, the problem of data analysis is analyzed. Next more details on the structure of particular carotenoid: trans-β-apo-8'-carotenal are presented.

The results of the TR-FSRS experiment in trans-β-apo-8'-carotenal are discussed next. Following the excitation of the sample a Raman line corresponding to the C=C symmetrical stretching vibration of the molecule is observed. Due to vibronic coupling of the electronic states, the frequency of this vibration differs significantly in ground and excited states. Therefore

it is easy to observe the dynamics of three states which, as it is postulated, take part in the transition. Most interesting is the behavior of the line corresponding to S_1 state of the molecule. The frequency of this line changes suggesting vibrational cooling but at the same time it appears that the line is first negative (Raman losses) within first 500 fs. This second fact suggests that transient vibrational inversion of population is present in the molecule.

In order to describe the above phenomenon a model of the molecule in a quantum mechanical approach was created. To explain it the quantum mechanical theory of coupling of light with molecular vibrations is discussed in the next section. First a simple 2 vibrational level system is described. The unperturbed molecular Hamiltonian and the perturbed Hamiltonian of the system are presented. Later, the time dependent operators in the Heisenberg picture, Heisenberg-Langevin equations of the two-level system are introduced. Many basic calculations supporting those sections are presented in the appendix. Discussion of the two-level model and the three-level model created by analogy to the first one is presented next. Finally the model of trans-β-apo-8'-carotenal molecule is constructed and some numerical aspects of model fitting are discussed. The results of modeling, confirming the possibility of involvement of only two electronically excited states and of presence of transient vibrational inversion of population are then discussed. The chapter ends with the "Conclusions" section.

In the last chapter the conclusions of the thesis are presented.

1.3 Classical theory of coupling of light with molecular vibrations

In this section a classical theory of coupling of molecular and crystal vibrations with light pulses is revised. The goal is to model a propagation of the light pulse in the medium disturbed by the very same pulse. The shape of the pulse has to be assumed arbitrary as it will change in a priori unknown way during the propagation. In the next chapter the partial differential equation for propagation of the electric field pulse will be presented. This equation will have to be solved numerically. Fortunately some analytical simplifications can be done to avoid numerical solution of the matter equation,what will be presented in the present section. Within the Born-Oppenheimer approximation [5, 6] the electronic and nuclear motion of a molecule or a crystal lattice can be separated. The normal coordinates and corresponding normal vibrations can than be introduced. In such a case the classical harmonic oscillator model can be used for description of the dynamics of these normal modes. In particular case of diamond it is easy to describe the medium by a harmonic oscillator model with a single resonant frequency. The harmonic oscillator model can be solved analytically with the Green's function approach and the convolution of such a Green's function (or Raman response function) with the pulse intensity can be included in the equation for the electric field. This way no differential equation for the medium has to be solved numerically and all the information about it is kept in the Raman response function. The solution of the matter equation of motion will be also discussed in this section for a number of example pulses.

In this section, first, the induction of the electric dipole in a molecule by electric field and the force due to the electric field acting on this dipole is discussed. The useful expression for this force for the envelope of the electric field is derived. Second, the equation of motion of matter in the form of the forced and damped harmonic oscillator is introduced and its general solution for arbitrary force with use of Green's function is presented. The dependence of the normal mode vibrational amplitude on the spectrum of the light pulse is also discussed. Finally the results of the two first subsections are combined to formulate the expression for the nonlinear medium polarization resulting from stimulated Raman scattering. The section is concluded with several examples of pulse induced vibrations.

1.3.1 The force due to the electric field

If $\vec{p_i} = \hat{\alpha}\vec{E}$ is the induced dipole moment, where $\vec{E}$ is the electric field and $\hat{\alpha}$ is the medium polarizability tensor, then the potential energy of the molecule is $E_P = -\frac{1}{2}\hat{\alpha}\vec{E}\vec{E}$[1] [7]. Here the dynamics of molecules and crystals is described in terms of normal mode amplitudes $q(t)$. Therefore, the driving force for a given normal mode can be obtained from the potential energy by taking its gradient [8]:

$$\vec{F} = \frac{1}{2}\left(\frac{\partial\hat{\alpha}}{\partial q}\right)_{q=0}\vec{E}\vec{E}. \tag{1.1}$$

Here the assumption is made that the light wavelength is much longer than the normal mode amplitude and thus its gradient can be neglected [9]. If an electric field has nonzero component along only one axis of the coordinate

[1]The permanent dipole moment and resulting infrared absorption phenomenon will be disused later in this section.

system at which the polarizability tensor is diagonal, the Eq. 1.1. takes the following form [10]:

$$F(t) = \frac{1}{2}\left(\frac{\partial\alpha}{\partial q}\right)_{q=0} E^2(t). \tag{1.2}$$

It is convenient to introduce the slowly varying amplitude of the pulse. In such a case the electric field is presented as a product of the term oscillating with pulse central (optical) frequency $e^{i\omega t}$ and the slowly varying amplitude of the pulse $A(t)$:

$$E(t) = \frac{1}{2}(A(t)e^{i\omega t} + A^*(t)e^{-i\omega t}), \tag{1.3}$$

or

$$E(t) = \frac{1}{2}|A(t)|(e^{i(\omega t+\varphi(t))} + e^{-i(\omega t+\varphi(t))}), \tag{1.4}$$

where $\varphi(t)$ is the slowly varying phase of the pulse.

If the relation 1.4. is used the Eq. 1.2. becomes:

$$F(t) = \frac{1}{4}\left(\frac{\partial\alpha}{\partial q}\right)_0 |A(t)|^2(1 + \cos(2\omega t + 2\varphi(t))). \tag{1.5}$$

The molecular vibrations (10^{12} – 10^{14} Hz) can be forced at frequencies being the difference of those contained within the ultrashort pulse spectrum rather than directly by the light pulses carrier frequency (10^{14} – 10^{15} Hz). Thus, as the vibrational transitions are considered, the $\cos(2\omega t + 2\varphi(t))$ can be omitted [4, 8] in Eq. 1.5. giving:

$$F(t) = \frac{1}{4}\left(\frac{\partial\alpha}{\partial q}\right)_0 |A(t)|^2. \tag{1.6}$$

As can be seen from Eq. 1.6. in presence of the ultrashort pulse the force that excites the vibrations, is proportional to the pulse intensity.

1.3.2 Equation of pulse driven motion

In the classical approach, in harmonic approximation, the equation of motion for a chosen normal vibrational mode in a molecule or a crystal takes the following form:

$$\ddot{q} + 2\gamma\dot{q} + \Omega^2 q = F(t), \tag{1.7}$$

where q(t) is the normal mode amplitude, $\vec{F}(t)$ is the driving force (Eq. 1.1.), γ is the vibrational damping coefficient and Ω is the angular frequency of the mode.

To solve this equation efficiently for forces described by Eq. 1.6. the approach of Green's function is preferable [11, 12]. The retarded Green's function for the harmonic oscillator is [13]:

$$G(t) = \frac{1}{\bar{\omega}} e^{-\gamma t} \sin \bar{\omega} t \ \Theta(t), \tag{1.8}$$

where $\bar{\omega} = \sqrt{\Omega^2 - \gamma^2}$ is the resonance frequency of damped oscillator and $\Theta(t)$ is the Heviside function. This retarded function is used in situations when there were no vibrations before appearance of the force. Now Eq. 1.7. can be solved by convolution of the Green's function with the force:

$$q(t) = \int_{-\infty}^{\infty} G\left(t - t'\right) F(t') dt' = G * F \tag{1.9}$$

(here $G * F$ is the convolution of G and F) or for the force defined by Eq. 1.6:

$$q(t) = \int_{-\infty}^{\infty} G\left(t - t'\right) \frac{1}{4} \left(\frac{\partial \alpha}{\partial q}\right) \left|A\left(t'\right)\right|^2 dt'. \tag{1.10}$$

It is interesting to examine the frequency dependence of the vibrational amplitude $q(t)$ by performing its Fourier transform:

$$F_T\left\{q(t)\right\} = \frac{1}{4} \left(\frac{\partial \alpha}{\partial q}\right) F_T\left\{G * |A|^2\right\} \tag{1.11}$$

where F_T stands for Fourier transform. The equation 1.11. is solved with use of the convolution theorem:

$$F_T\left\{G * F\right\} = F_T\left\{G\right\} F_T\left\{F\right\}, \tag{1.12}$$

therefore:

$$F_T\left\{q(t)\right\} = \frac{1}{4} \left(\frac{\partial \alpha}{\partial q}\right) F_T\left\{G\right\} F_T\left\{|A|^2\right\}. \tag{1.13}$$

The Fourier transform of the Green's function is:

$$F_T\left\{G\right\} = \frac{1}{\bar{\omega}} \left(\frac{1}{i(\omega + \bar{\omega}) - \gamma} - \frac{1}{i(\omega - \bar{\omega}) - \gamma}\right), \tag{1.14}$$

and a convolution theorem can be used for calculation of $F_T\left\{|A|^2\right\}$:

$$F_T\left\{|A|^2\right\} = F_T\left\{A^* A\right\} = F_T\left\{F_T^{-1}\left\{\hat{A}^*\right\} F_T^{-1}\left\{\hat{A}\right\}\right\} = \hat{A}^* * \hat{A}, \tag{1.15}$$

where $\hat{A}$ and $\hat{A}^*$ are Fourier transforms of A and A^*, respectively. Finally, the Fourier transform of $q(t)$ is:

$$\hat{q}(\omega) = \frac{1}{2}\left(\frac{\partial\alpha}{\partial q}\right)\frac{1}{\bar{\omega}}\int_{-\infty}^{\infty}\left(\frac{A^*(\omega')A(\omega-\omega')}{i(\omega+\bar{\omega})-\gamma} - \frac{A^*(\omega')A(\omega-\omega')}{i(\omega-\bar{\omega})-\gamma}\right)d\omega'. \tag{1.16}$$

Obviously the denominators in the above equation are the smallest in the case of resonance: $\omega = \pm\bar{\omega}$. Anyway the value of the convolution:

$$\int_{-\infty}^{\infty} A^*(\omega')A(\bar{\omega}-\omega')d\omega'. \tag{1.17}$$

also has to be significant if the vibrational amplitude is supposed to be high. This happens when a pair or pairs of spectral components with spectral separation close to $\bar{\omega}$ are present in the spectrum of the pulse envelope [4].

1.3.3 Polarization

The electric dipoles, induced in the material, become a source of a new wave. Therefore to study the deformation of the laser pulse further investigation of the medium polarization is required. The total dipole moment of a molecule or a crystal unit cell contains both: the induced dipole moment $\vec{p_i} = \hat{\alpha}\vec{E}$ and the permanent dipole moment $\vec{\mu}$ [7, 9]:

$$\vec{p} = \vec{\mu} + \hat{\alpha}\vec{E}, \tag{1.18}$$

or in present simplified consideration when all vectors have the same direction parallel to an axis of the coordinate system in which $\hat{\alpha}$ is diagonal:

$$p = \mu + \alpha E, \tag{1.19}$$

In the case when the frequency of electric field is far from the electronic resonance [8], both μ and α can be expanded into Taylor series with respect to small vibrational amplitudes [10, 14]:

$$\mu = \mu\left(0\right) + \left(\frac{\partial \mu}{\partial q}\right)_0 q + ..., \tag{1.20}$$

$$\alpha = \alpha\left(0\right) + \left(\frac{\partial \alpha}{\partial q}\right)_0 q + ..., \tag{1.21}$$

where for simplicity only one vibrational mode q is considered. If the third and higher order terms of the Taylor series in equations 1.20. 1.21. are neglected the equation 1.19. takes the following form [8]:

$$p = \mu(0) + \left(\frac{\partial \mu}{\partial q}\right)_0 q(t) + \alpha(0)E(t) + \left(\frac{\partial \alpha}{\partial q}\right)_0 q(t)E(t), \tag{1.22}$$

the second and third terms in the above equation are the "infrared absorption" (absorption of light of frequency close to that of the vibrations) and the Rayleigh scattering (where no change of frequency of incoming light is present), respectively. The last term in equation 1.22. is responsible for the Raman scattering.

In the case of interaction with ultrashort pulse $q(t)$, given in the form defined by Eq. 1.10, has to be substituted to Eq. 1.22. Together with the

slowly varying amplitude, the Raman part of the dipole moment becomes:

$$p_R = \frac{1}{4}\left(\frac{\partial\alpha}{\partial q}\right)_0^2 \left(A(t)e^{i\omega t} + A^*(t)e^{-i\omega t}\right) \int_{-\infty}^{\infty} G\left(t-t'\right)\left|A\left(t'\right)\right|^2 dt'. \quad (1.23)$$

And thus the nonlinear polarization of light in this case is:

$$P_R = N\frac{1}{4}\left(\frac{\partial\alpha}{\partial q}\right)_0^2 \left(A(t)e^{i\omega t} + A^*(t)e^{-i\omega t}\right) \int_{-\infty}^{\infty} G\left(t-t'\right)\left|A\left(t'\right)\right|^2 dt', \quad (1.24)$$

where N is the density of molecules (or unit cells in a crystal).

1.3.4 Examples

Several simple examples on the subject of vibrations of crystal driven by light pulse will be presented in this section. In the later simulation, a Green's function will be used for description of the vibrational amplitudes behavior, however, it is instructive to leave a normal mode amplitude as a variable for a moment. In the section 2.3.1. the pulse propagation equation (Eq. 2.3.) will be introduced in details. Here a simplified equation is presented:

$$\frac{\partial A}{\partial z} = iC_1 p^+ + \ldots, \quad (1.25)$$

for propagation of the envelope $A(z,t)$ in the unrealistic medium, where the nonlinear polarization is just due to stimulated Raman scattering (from Eq. 1.23.), wheras:

$$p^+ = C_2 q(t) A(z,t), \quad (1.26)$$

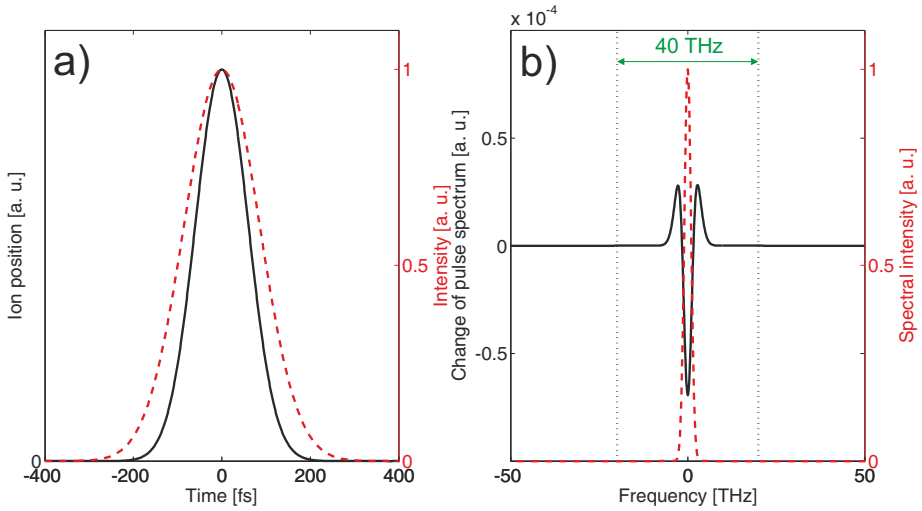

Figure 1.1: The time profile of the normalized pulse intensity (red dashed curve), and the normalized vibrational amplitude (black curve) (a) and the spectral intensity of the pulse (red dashed curve) and the relative change of the spectrum due to propagation in the Raman medium (black curve) (b) for the case of 200 fs long pulse.

and C_1 and C_2 are constants. The equation of motion 1.7. with the light intensity dependent force given by Eq. 1.6. is used to obtain $q(t)$, which is required in Eq. 1.26. After solution of Eq. 1.25. the relative change of the pulse spectrum:

$$\frac{|F_T\{A(z+\Delta z,t)\}|^2 - |F_T\{A(z,t)\}|^2}{|F_T\{A(z,t)\}|^2} \tag{1.27}$$

where $A(z+\Delta z,t)$ is the solution of Eq. 1.25. and F_T stands for Fourier transform can be calculated. A few examples for different pulse amplitudes $A(z,t)$ are given below, in all of them the diamond with its frequency 1332 cm^{-1} and decay time 5.7 ps is used as a medium and Fourier limited Gaussian pulses are used.

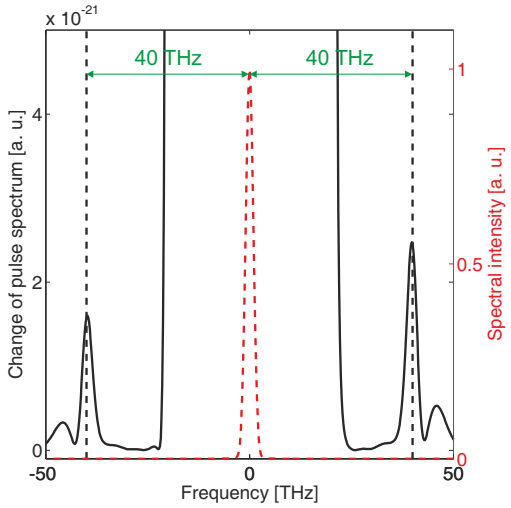

Figure 1.2: Enlarged Fig. 1.1. The relative change of the spectrum due to propagation in the Raman medium for the case of 200 fs long pulse.

The first example is calculated for a 200 fs pulse. The time profile of a pulse intensity together with the time dependance of the normal mode amplitude are presented in Fig. 1.1. (a). As the pulse is long the material system has enough time to follow the envelope of the light intensity and no significant vibrations are induced. The spectrum of the pulse together with it's relative change (Eq. 1.27.) are presented in Fig. 1.1. (b). The spectrum of the pulse is narrow and fits in between the two vertical lines separated by vibrational frequency of diamond. It broadens slightly but, as discussed in section 1.3.2, the vibrations can't be forced efficiently [15]. The pairs of spectral components with spectral separation close to resonant frequency are very weak in the spectrum of A. Still, small peaks separated by 40 THz from the central frequency appear in the spectrum which is visible in Fig. 1.2.

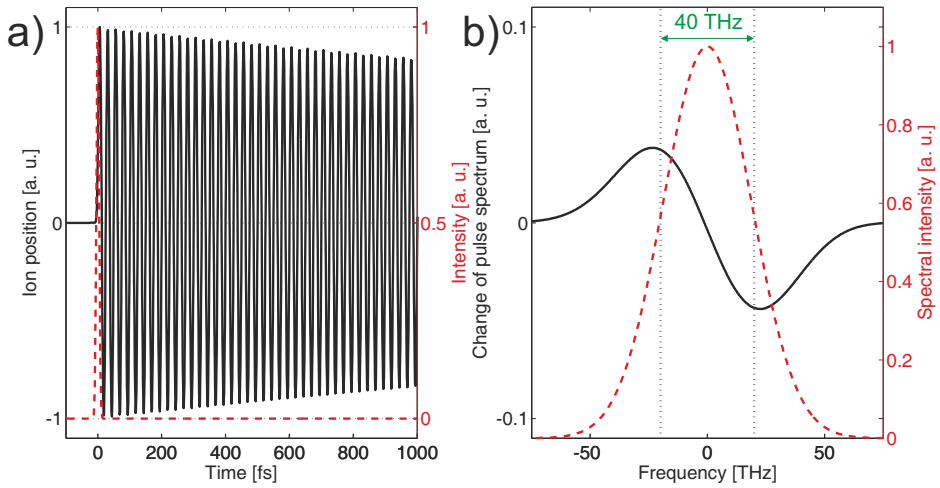

Figure 1.3: The time profile of the normalized pulse intensity (red dashed curve), and the normalized vibrational amplitude (black curve) (a) and the spectral intensity of the pulse (red dashed curve) and the relative change of the spectrum due to propagation in the Raman medium (black curve) (b) for the case of short, 10 fs pulse.

Extremely short, 10 fs, pulse displaces the system from the equilibrium position and leaves the sample. Thus, the system comes back to the equilibrium position performing relaxation oscillations with its eigen frequency. In fact, it was only in the year 2006 that the coherent optical phonons in diamond, induced by ISRS with sub-10fs pulses were observed experimentally [16]. This situation is presented in Figure. 1.3. (a). The spectrum of a short pulse is broad (see Fig. 1.3. (b)), thus it contains a frequency components that give a difference frequency equal to the resonant frequency of the normal mode in a crystal. In such a case the stimulated Raman gain is significant and the red shift of the pulse spectrum occurs [4, 17]. The spectrum is modified in quite homogenous way [18] and no spectral features, like for example Raman lines, are present. This is because there are many frequency pairs that give a difference of frequency equal to the resonance frequency in the pulse spectrum and those pairs have similar intensities. In fact the transformation of Eq. 1.26. gives:

$$F_T\{C_2 q(t) A(z,t)\} = C_2 \int_{-\infty}^{\infty} \hat{q}(\omega) A(z, \omega' - \omega) d\omega', \tag{1.28}$$

which is the convolution of the two spectra: $\hat{q}(\omega)$ and $A(z, \omega' - \omega)$.

The next example is for two overlapped in time 100 fs pulses of different frequencies. The difference of frequencies was chosen to be equal to the resonance frequency of the material system. The result is presented in Figure 1.4. The two pulses interfere and an interference pattern can be observed in the time profile of the pulse intensity (Fig. 1.4 (a)). The period of the fringes is equal to the resonance frequency thus every next fringe drives the normal vibrations of atoms. In such a situation the energy flows from one pulse

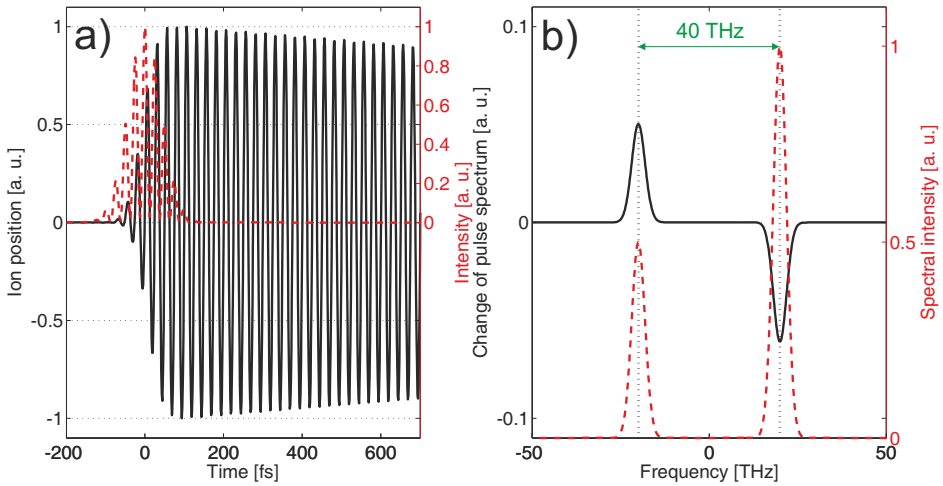

Figure 1.4: The time profile of the normalized pulse intensity (red dashed curve), and the normalized vibrational amplitude (black curve) (a) and the spectral intensity of the pulse (red dashed curve) and the relative change of the spectrum due to propagation in the Raman medium (black curve) (b) for the case of two 100 fs pulses with different frequencies.

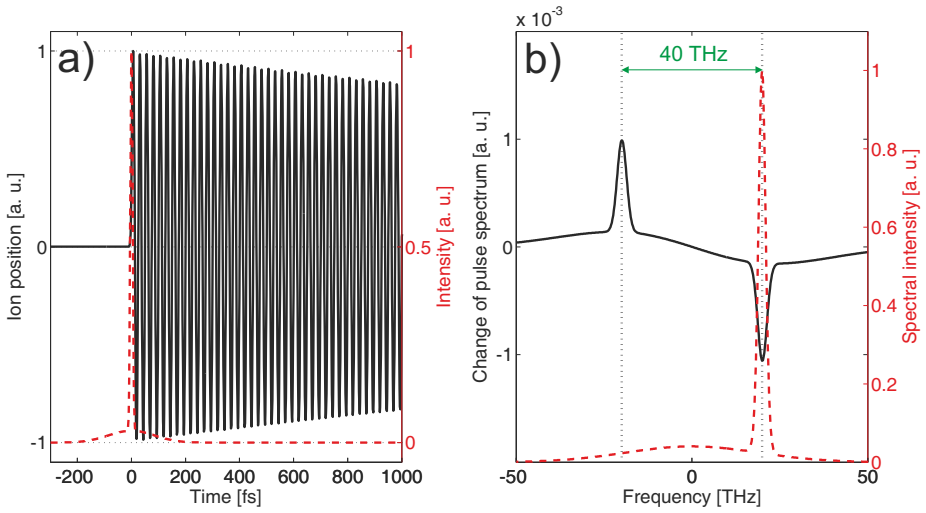

Figure 1.5: The time profile of the normalized pulse intensity (red dashed curve), and the normalized vibrational amplitude (black curve) (a) and the spectral intensity of the pulse (red dashed curve) and the relative change of the spectrum due to propagation in the Raman medium (black curve) (b) for the case of two (200 and 10 fs) overlapped pulses.

to another through the coupling with atomic vibrations (Fig. 1.4 (b)). A higher frequency pulse experiences losses while the lower frequency pulse is amplified.

The final interesting example is presented in Figure 1.5. Here a narrow-band pulse is overlapped with a broadband, the first one is 200 fs while the second one is 10 fs long. The slope of the long pulse reaches the system first but it is the short pulse that initiates the vibrations (Fig. 1.5 (a)). It is visible in the spectrum (Fig. 1.5 (b)) that it is the long, narrow-band pulse that experiences losses in favor of a spectral region of the short, broad-band pulse separated by resonance frequency from the frequency of the long pulse.

Therefore a presence of a Raman line in this region is expected after long propagation.

The conclusion from the examples given above is that a broad-band spectrum is required to initiate vibrations of a diamond. Moreover, in such a case, the energy can flow in between the spectrum features of the pulse.

As will be discussed later, in the case of supercontinuum generation the initial spectrum of the pulse entering the diamond will be to narrow to force the vibrations efficiently. This is a situation similar to that of the first example. This spectrum will however evolve due to self-phase modulation, and the interaction with free carriers, and its shape will become similar to that of the last example. The time profile of the pulse will differ significantly from the one presented in the last example, but, still, the Raman gain on the long wavelength side of the main spectral peak will be expected, as is presented in Fig. 1.5.

The last example presents also the idea behind the construction of the probe pulse in the Time-Resolved Femtosecond Stimulated Raman Scattering experiment. Here the broadband pulse is combined with strong narrow band pulse, and the presence of Raman lines is expected in the spectrum of such a pulse after propagation in the sample.

Chapter 2

Stimulated Raman Scattering in supercontinuum generation in diamond

In this chapter the supercontinuum generation process in bulk diamond is studied experimentally and by means of numerical simulation. In particular the question of the influence of diamond vibrations, excited through stimulated Raman scattering, on the supercontinuum generation is considered.

The broadening of the spectrum of intense laser light in media was first observed in 1960' [19–23]. Broadening as high as of 100 cm^{-1} was found for pulses from Q-switched lasers in liquids [23] and later supercontinuum of 10 000 cm-1 for ps pulses in transparent media was observed [24, 25]. First and most important effect, which was found responsible for broadening, was self-phase modulation (SPM) [19, 21, 23, 26, 27] and its spatial manifestation – self-focusing [28, 29].

The theoretical problem of light propagation in a medium with self-focusing together with SPM and dispersion is complex, thus first experiments were aiming at SPM studies in absence of the self-focusing. Therefore, studies on generation in fibers [30–33] were performed. Here a beam with intensity below self-focusing threshold could be propagated through several meters of the medium and acquire the nonlinear phase due to SPM. In addition to SPM the presence of features attributed to stimulated Raman scattering were observed in those studies [31]. An alternative was to study light propagation in thin films where self-focusing can be neglected. The effect of "self-steepening" has been revealed by those studies [34–37].

From the beginning of the studies on supercontinuum generation it was suggested that the ionization takes part in the process [38], however, experiments in gasses suggested that this aspect is negligible [33]. Anyway, only in 1990' when the advance of computer technology made multidimensional numerical studies of the topic possible, it was found that all processes: SPM, self-focusing, self-steepening, photoionization and interaction with free charges and, in case of gasses, stimulated Raman scattering [39] have to be included in simulations to obtain results comparable with experiments [39–41].

It is obvious that SRS plays a significant role in supercontinuum generation in long media, like for example fibers [31–33, 42], where intensity of light pulse is moderate and the nonlinear effects slowly buildup during the propagation. It is also included in the simulations of generation in gasses [39]. But it has been argued in many recent works on supercontinuum generation, that in thin solid samples the Raman response of the medium might be neglected [40, 43–46]. The question arises whether this assumption is

valid. To answer this question, herewith the diamond crystal is put under study. Diamond seems to be a perfect material for SRS study. The Raman response of diamond is orders of magnitude higher than that of fused silica and other solids [47]. It is thus used in Raman lasers [48] and in four wave mixing sources [49]. Moreover, its Raman response can be easily resolved as diamond has a single first order Raman line at 1332 cm^{-1}.

The presence of free-current causes defocusing of the beam [40] and thus can stop the self-focusing process. Recently the 5th order nonlinear processes (self-phase modulation saturation) has been shown to play a significant role in supercontinuum generation in gases [50, 51] and that the defocusing due to free-current was overestimated. Therefore, it is currently unclear whether free-current or 5th order non-linearity affects the self-focusing more significantly. The self-phase modulation saturation was included in the simulation presented in the present dissertation. This additional term has improved the resamblance of the simulation results with the experimental ones.

The main results of studies described in this chapter were published [52].

The chapter is constructed as follows. In first section the setup for supercontinuum generation experiment constructed in European Laboratory for Nonlinear Spectroscopy in Florence is described. Second, the experimental results from measurements in the diamond crystal are presented. In section 2.3. the model of supercontinuum generation based on the nonlinear envelope equation along with contributions corresponding to different phenomena is discussed. Next details on the implementation of the model are presented. Finally the results of the simulation and the experiment are compared and discussed.

2.1 Experimental arrangement

The usual way of generation of supercontinuum for spectroscopic purposes is first to filter the light intensity and then to filter the beam spatially with the iris of variable diameter and finally focusing it with a lens on the bulk medium. The light intensity, the diameter of iris and the position of lens or the medium in the direction of propagation are controlled in order to achieve most stable and broad supercontinuum spectrum. The experimental setup in the present study (see Figure. 2.1) was simplified to make a comparison of modeling results with the experiment more direct. So the aperture was not placed in order to avoid the difficulty of determining its actual diameter and position. The position of the crystal was the same for the whole set of measurements for various intensities. The beam was attenuated with neutral density filters.

The supercontinuum generation experiment was performed in European Laboratory for Nonlinear Spectroscopy in Florence. The light source was a Ti:sapphire regenerative amplifier (Coherent Inc. Legend Elite) with repetition rate of 1 kHz. The spectrum of the pulses was centered at 800 nm and its full width at half maximum was close to 25 nm and the pulse length was close to 40 fs. The beam with waist of 4.8 mm was focused on the sample with 125 mm lens.

The sample was illuminated with relatively intense pulses with easily measurable energies from 8 to 30 μJ (10 - 40 GW/cm^2). For such high energies multiple filamentation and damage of the sample placed in the focus could occur. Therefore, the sample was displaced from the focus by 3.7 mm

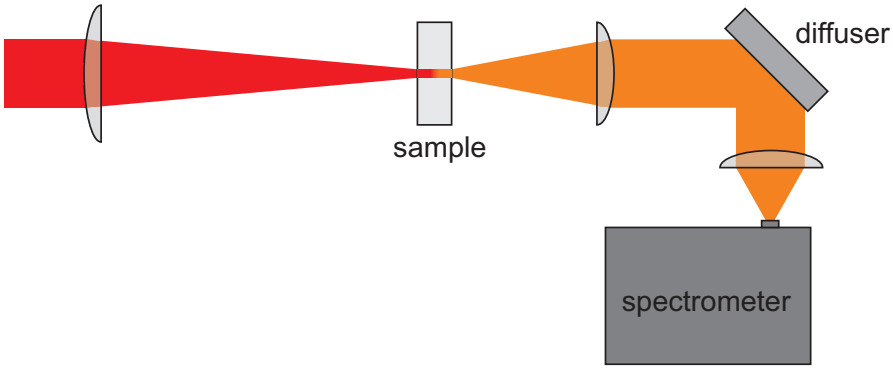

Figure 2.1: The setup for studying the generation supercontinuum in diamond.

towards the lens, so that the beam size at the entrance of the sample was about 150 μm. The sample was a 2 mm thick diamond crystal of type IIa.

The outgoing beam was imaged on the ground glass plate and diffused light was gathered by a spectrometer. The spectrometer was Ocean Optics USB2000 with useful spectral range from 340 to 1020 nm. The spectrometer sensitivity was calibrated with a black body spectrum. The spectra of outgoing light were acquired for different input pulses energy.

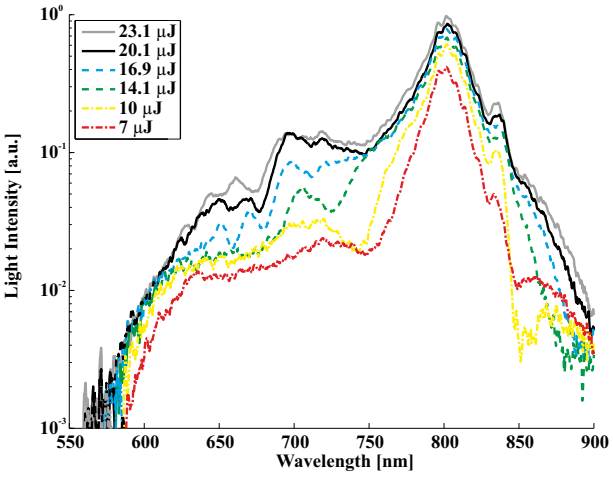

Figure 2.2: Selection of spectra of supercontinua generated in diamond for different input energies.

2.2 Experimental Results

A selection of supercontinua spectra, generated in the experiment for different input energies, are presented in Fig. 2.2. and all acquired spectra are presented on the map in Fig. 2.3. For energies below 8 μJ only slight broadening of the spectrum is observed. The spectrum broadening becomes significant for energies close to 15 μJ. For energies over 30 μJ the interference fringes appear in the supercontinuum beam pattern. The interference fringes may be caused by multiple filamentation or multiple beam refocusing in the sample. The spectra obtained at energies higher than 10 μJ contain fringe-like features. The period and position of those features are intensity dependent, what suggests that their origin results from self-phase modulation [32].

As shown by Brodeur and Chin [53] the energy difference between the blue edge of the supercontinuum and the pump central frequency is a mono-

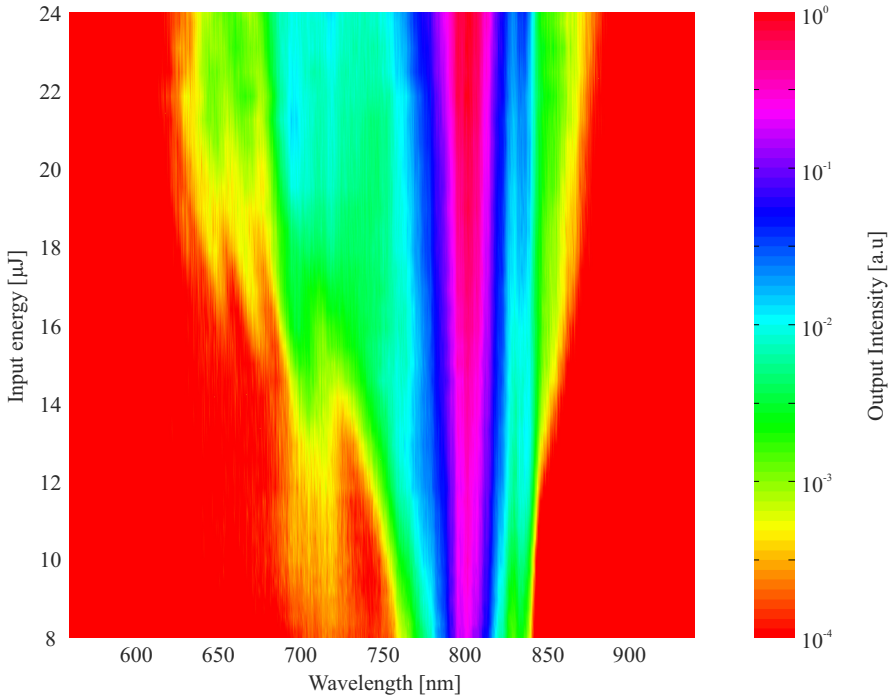

Figure 2.3: Spectra of generated supercontinua as a function of input energy measured in experiment.

tonicaly growing function of the material band gap energy. This observation was confirmed by studies of supercontinuum generation in laser host crystals [54]. The blue edge of the supercontinuum generated in diamond was found to be close to 600 nm. Although this value is high, it does not stand out from the set of accumulated data for different media [54, 55].

For input energies over 17 μJ a growing peak at wavelength of 720 nm can be observed. Fig. 2.4 presents close-up on this peak in several spectra acquired for different input intensities. The wavelength of the peak does not depend on the input intensity and therefore is not alike the features described before. The frequency separation between the peak and the central frequency

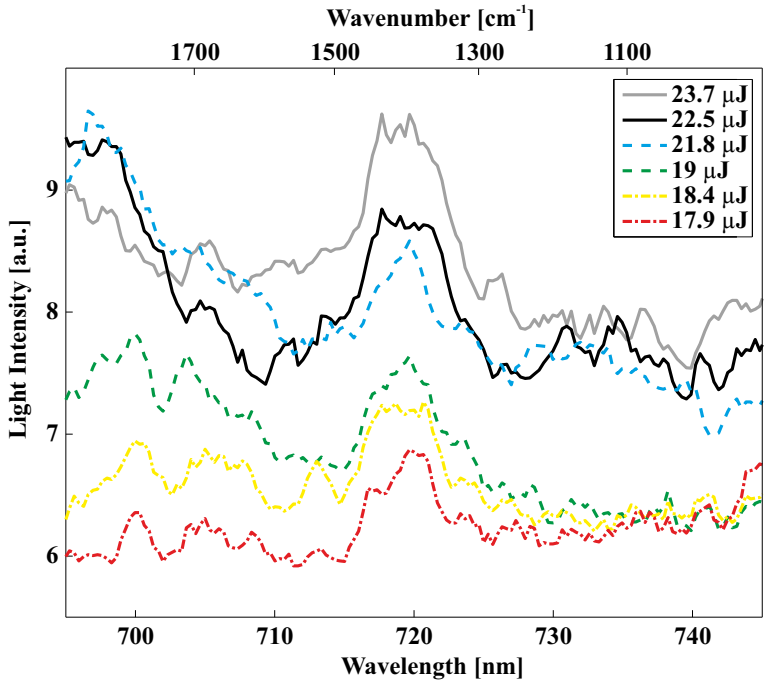

Figure 2.4: and peak in supercontinua spectra in vicinity of expected anti-Stokes Raman line (b)

of the input light is close to frequency of the only diamond vibration at 1332 cm^{-1}. Therefore, the peak was attributed to the consequence of stimulated Ramman scattering.

2.3 Model

The propagation of light is governed by Maxwell equations, thus all models of pulse propagation are based on the Maxwell equations and the wave equation resulting from them [32, 33, 39, 40, 46, 56–61].

Numerical solution of the complete wave equation which is of the second order in, both, time and space require finite difference or finite element methods [62]. In those methods the whole spatial domain in which the propagation occurs has to be represented. With the current advance of computer technology, it is possible to perform simulations of ultrashort pulse propagation in dispersive and even nonlinear media with those methods [63]. However, the problem becomes extremely complicated when the memory of the medium has to be considered [63, 64]. This is the case when stimulated Raman scattering or free current dynamics is considered.

The problem is significantly simplified when the wave equation is transformed into the equation of the first order with respect to the propagation direction. This can be done by assumption that the pulse envelope varies slowly [57] or that the electric field component along the direction of propagation is negligible and by considering only one direction of wave propagation [59].

First models of nonlinear propagation were created with intention of analytical solution, they were, therefore, as simple as possible. They form a class of single dimensional models based on the, so called, Nonlinear Shrödinger equation (NLSE) [32, 33]. These are still very useful for simulations of light propagation in fiber optics. The NLSE extended by diffraction was later

introduced to study the effects of self-focusing with the unrealistic result of "catastrophic collapse" of the beam into a singularity [33].

The NLSE requires the pulse amplitude to be slowly varying in both space and time. In the case of ultrashort pulses this second approximation has to be relaxed. This was done by Brabec and Krausz in 1997 [57] when they proposed the nonlinear envelope equation (NEE), which is the equation used for simulations in the present dissertation.

Other equations, very similar to NEE are: the Partially Corrected Nonlinear Shrödinger equation [50, 58] with diffraction frequency dependence included in the approximated way and modified Kadomtsev–Petviashvilli equation of type 1 [46], which differs from NEE by the form of dispersion presentation.

In the NEE the "catastrophic collapse" of the beam can be blocked by 5'th order non-linearity and interaction with the free-current [40, 61]. However a class of equations where the the "catastrophic collapse" is arrested by higher orders of diffraction exists. These are the unidirectional pulse propagation equation (UPPE) [59], forward Maxwell equation [58] and others [60, 65].

In this section the model for supercontinuum generation based on the nonlinear envelope equation [57] will be presented. The consecutive terms corresponding to dispersion, diffraction, SPM, self-steepening, SRS, multiphoton ionization and interaction with free current will be discussed for the case of diamond crystal.

2.3.1 Master equation

The phenomenon of supercontinuum generation is modeled in this thesis with use of nonlinear envelope equation. In this section the process of derivation of this equation will be briefly described. First, the original derivation by T. Brabec and F. Krausz expanded by J. R. Gulley and W. M. Dennis to include free charge carriers will be explained. Then the derivation from more general unidirectional pulse propagation equation done by M. Kolesik and J. V. Moloney will be summarized in order to explain the main approximations and resulting advantages and disadvantages of the nonlinear envelope equation approach.

The nonlinear envelope equation was derived by T. Brabec and F. Krausz in 1997 [57] for simulation of propagation of single-cycle pulses. This derivation was later revised by J. R. Gulley and W. M. Dennis [41] to include free-carrier effects. The derivation starts with wave equation obtained from Maxwell laws:

$$\nabla^2 \vec{E}(\vec{r},\tau) - \frac{1}{c^2}\partial_\tau^2 \int_{-\infty}^{\tau} \epsilon(\tau-\tau')\vec{E}(\vec{r},\tau')d\tau' = \mu_0 \partial_\tau^2 \vec{P}_{nl}(\vec{r},\tau) + \mu_0 \partial_\tau \vec{J}(\vec{r},\tau), \tag{2.1}$$

where the linear in electric field ($\vec{E}(\vec{r},\tau)$) part of the polarization was already included into the absolute permittivity $\epsilon(\tau)$, μ_0 is the magnetic constant, $\vec{P}_{nl}(\vec{r},\tau)$ is the nonlinear polarization, $\vec{J}(\vec{r},\tau)$ is the current density and τ is the real time. The envelopes of the electric field, nonlinear polarization and

current density are then introduced:

$$\begin{aligned}
\vec{E}(\vec{r},\tau) &= \vec{e}\tfrac{1}{2}\left(A(\vec{r}_\perp,\zeta,\tau)e^{i(k_0 z-\omega_0\tau)}+c.c\right),\\
\vec{P}_{nl}(\vec{r},\tau) &= \vec{e}\tfrac{1}{2}\left(p_{nl}(\vec{r}_\perp,\zeta,\tau)e^{i(k_0 z-\omega_0\tau)}+c.c\right),\\
\vec{J}(\vec{r},\tau) &= \vec{e}\tfrac{1}{2}\left(j_{fc}(\vec{r}_\perp,\zeta,\tau)e^{i(k_0 z-\omega_0\tau)}+c.c\right),
\end{aligned} \tag{2.2}$$

where A, p_{nl} and j_{fc} are the appropriate complex envelopes, $\vec{e}$ is the direction of the electric field polarization, ω_0 is the reference frequency, usually chosen to be the central frequency, $k_0 = Re\{k(\omega_0)\}$ is the real part of the propagation constant taken at reference frequency ($k(\omega) = \omega/c\sqrt{\epsilon(\omega)}$, ζ is the coordinate along the propagation axis. The integral in Eq. 2.1. is Fourier transformed into frequency space, where the complex propagation constant k is expanded in Taylor series in the frequency domain, and then Fourier transformed back into time space. Additionally the change of variables: $z = \zeta$, $t = \tau - \zeta/v_g$ is performed to introduce the reference frame moving with the pulse group velocity v_g. Finally the slowly-varying-envelope approximation is used to omit some higher order and mixed envelope derivatives and other terms (which physical meaning will be explained later) and the nonlinear envelope equation is obtained as follows:

$$\frac{dA}{dz} = \left(i\hat{D} + \frac{i}{2k_0}\hat{T}^{-1}\nabla_\perp^2\right)A + i\frac{\omega_0\hat{T}}{2n_0\epsilon_0 c}p_{nl} - \frac{1}{2n_0\epsilon_0 c}j_{fc}, \tag{2.3}$$

here $\hat{D}$ is the dispersion operator coming from Taylor series expansion of the propagation constant, $\hat{T} = \left(1 + \frac{i}{\omega_0}\frac{\partial}{\partial t}\right)$ is, so called, steepening operator, $\nabla_\perp^2$ is the transverse Laplace operator, n_0 is the value of the refractive index at reference frequency, ϵ_0 is the vacuum permittivity, and c is the speed of light.

This equation can be derived with slowly-varying-envelope approximation, but as shown by Brabec and Krauszmit can also be derived with weaker assumptions – so called slowly-evolving-wave approximation. The slowly-varying-envelope approximation requires the pulse envelope not to change significantly after passing distances as small as the optical wavelength:

$$|\partial_z A| << k_0|A|, \tag{2.4}$$

and the pulse duration to be significantly longer than optical oscillation period:

$$|\partial_t A| << \omega_0|A|. \tag{2.5}$$

In the slowly-evolving-wave approximation this second condition is not required. Thus, even propagation of single-cycle pulses can be simulated with NEE. Instead of Eq. 2.5 the slowly-evolving-wave approximation requires the phase of the pulse envelope (φ) not to vary significantly along the propagation direction:

$$|\partial_z \varphi| << k_0. \tag{2.6}$$

The two conditions 2.4 and 2.6 for envelope and phase respectively can be gathered into one concerning the elctric field:

$$|\partial_z E| << k_0|E|. \tag{2.7}$$

The derivation of T. Brabec and F. Krausz is straightforward. However, to see what optical effects are neglected in nonlinear envelope equation, it is convenient to study another approach for its derivation.

In 2002 M. Kolesik, J. V. Moloney and M. Mlejnek presented another propagation model, so-called unidirectional pulse propagation equation [59]. This model was developed for simulations of extremely tight focused beams, where the focus size approaches the wavelength of light. Those situations could not be well described by nonlinear envelope equation and other models. Namely, extremely tight focusing leads to intensity "blowup" where the size of the beam shrinks towards a singularity. This problem is solved by taking into account the nonzero component of the field along the propagation axis in the complete vectorized version of UPPE. In the case of supercontinuum generation, however, the excitation of plasma (the presence of the current density term) prevents the catastrophic self-focusing [40]. Therefore fully vectorized approach is not required in the present case and the scalar version of UPPE can be used. The scalar UPPE in frequency and wavenumber domain is as follows:

$$\partial_z E(\vec{k}_\perp, z, \omega) = ik_z E(\vec{k}_\perp, z, \omega) + \frac{i\omega^2}{2\epsilon_0 c^2 k_z} P_{nl}(\vec{k}_\perp, z, \omega) - \frac{\omega}{2\epsilon_0 c^2 k_z} J(\vec{k}_\perp, z, \omega), \tag{2.8}$$

where the component of the propagation constant along propagation axis is evaluated from the other two components as:

$$k_z = \sqrt{k^2 - k_x^2 - k_y^2},\ k^2 = \frac{\omega^2 \epsilon(\omega)}{c^2}. \tag{2.9}$$

This equation can be derived directly from Maxwell equations with only two assumptions [58]. First, the backward propagating field is neglected and, therefore, it is not used for polarization and current evaluation. Second, as

has been already stated, the component of the field along the propagation is neglected.

The nonlinear envelope equation can now be obtained from unidirectional pulse propagation equation in a few following steps. First, the propagation constant coordinate along propagation axis can be expanded into the Taylor series around $\omega = \omega_0$, $k_x = 0$ and $k_y = 0$:

$$k_z(\omega) = \sum_{j=0}^{\infty} \frac{1}{j!} \left. \frac{\partial^j k}{\partial \omega^j} \right|_{\omega=\omega_0, k_x=0, k_y=0} (\omega - \omega_0)^j + \sum_{j=0}^{\infty} \frac{(-1)^j}{(2j)! k(\omega_0)^{2j-1}} \left(k_x^{2j} + k_y^{2j}\right) \tag{2.10}$$

The first sum in the above equation is actually equal to expansion of $k(\omega)$ and it will be kept while the terms from the second sum for $j > 1$ are neglected:

$$k_z(\omega) \approx k(\omega) - \frac{1}{2k(\omega_0)} \left(k_x^2 + k_y^2\right), \tag{2.11}$$

this approximation is used in the first term in the right hand side of equation 2.8. One can now explicitly see that higher order diffraction terms are neglected, this is in fact a paraxial approximation. Second, the propagation wavevector coordinate along propagation axis, which is present in the nonlinear polarization and the current density term, is approximated as follows:

$$\frac{1}{k_z} \approx \frac{c}{\omega n_0}, \tag{2.12}$$

where, the dependence on the transverse coordinate of the wavevector is neglected completely, additionally refractive index dispersion is also neglected. The Eq. 2.3. can be obtained by Fourier transformation of Eq. 2.8. with these approximations.

Finally, from the above analysis one can see that the nonlinear envelope equation can be derived from the unidirectional pulse propagation equation with a paraxial approximation and by taking constant refractive index in the denominator in front of the nonlinear polarization and current density terms.

In 1999 L. Gaeta [40] considered the phenomena of multiphoton absorption resulting in ionization of the material during supercontinuum generation. The equation for plasma density with multiphoton absorption and avalanche ionization and the modification of nonlinear envelope equation by inclusion of current density was then proposed[1]. Gaeta showed that in the case of supercontinuum generation the catastrophic self focusing towards a singularity is stopped by phenomenon of photoionization. Therefore, the assumptions of paraxiality and negligence of the field vector component along the propagation axis are justified. The constant refractive index in the denominator has a very small influence on the simulation results in the conditions considered here [46,56,59]. Finally as pointed out by M. Kolesik and J. V. Moloney [58] it is not a priori known, whether the backward propagating wave is negligible. This last assumption is, however, required for all known propagation models [58]. The nonlinear envelope equation was used for supercontinuum generation simulation many times since its formulation [40, 41, 44, 46, 50, 59, 67]. Its validity was verified and, therefore, it was chosen for the master equation in the present thesis.

[1]The plasma contributions of similar form to that proposed by Gaeta were earlier considered for master equations not suited for single-cycle pulse propagation [39,66].

2.3.2 Dispersion

The dispersion operator in Eq. 2.3 is:

$$\hat{D} = \sum_{m=2}^{\infty} \frac{k_m}{m!} (i\partial_t)^m, \tag{2.13}$$

where:

$$k_m = Re \left(\frac{\partial^m k}{\partial \omega^m} \right)_{\omega_0} \tag{2.14}$$

are the real parts of the propagation constant derivatives over the frequency detuning ω from the central frequency ω_0. The imaginary part of propagation constant (linear absorption) is neglected in this study. Of course it is impossible to use the whole infinite set of k_m, thus usually a few number of terms from the above series (Eq. 2.13.) are used in simulation. In reality the number of terms is reduced, mainly because one cannot measure k_m for $m > 4$ precisely. For our particular study it is however useful to follow back the origins of this form of dispersion operator.

The dispersion operator as in Eq. 2.13. comes from the Taylor series expansion of the propagation constant in Fourier space:

$$k(\omega_0 + \omega) = \sum_{m=0}^{\infty} \frac{k_m}{m!} \omega^m. \tag{2.15}$$

During the derivation of NEE the term k_0 and ωk_1 are reduced when field envelope and local time are introduced, thus one finds the dispersion operator to be:

$$\hat{D} = F_T^{-1} \left\{ k - (k_0 + \omega k_1) \right\}, \tag{2.16}$$

which equals:

$$F_T^{-1}\left\{\sum_{m=2}^{\infty}\frac{k_m}{m!}\omega^m\right\}, \tag{2.17}$$

here F_T^{-1} stands for inverse Fourier transform. The inverse Fourier transform can be evaluated and the equation 2.16 becomes 2.13.

In this study, however, it is preferable to use the Fourier space form of the dispersion operator (Eq. 2.16.). This is because, as will be shown later, the computational algorithm evaluates the dispersion operator in the Fourier space. Thus, the propagation constant $k = k(\omega_0 + \omega)$ for various frequencies and its derivatives k_0 and k_1 at central frequency are calculated using Sellmair formula for diamond [68]:

$$n^2 = A + \frac{B\lambda^2}{\lambda^2 - C} + \frac{D\lambda^2}{\lambda^2 - E}, \tag{2.18}$$

where n is the diamond refractive index and λ is the light wavelength in vacuum, the values of the parameters can be found in table 2.1.

Table 2.1: Coefficients of in the Sellmair formula for diamond [68].

A	2.30982863
B	3.35656148 μm^{-2}
C	0.0173019053 μm^2
D	3.25669602 μm^{-2}
E	2500 μm^2

2.3.3 Nonlinear Polarization

Historically the self-phase modulation was considered to be the main factor of spectrum broadening during the supercontinuum generation [25,33,69].

There are, however, indications that also higher order non-linearities can play a significant role in generation process [50, 51]. It was shown that not only plasma generation but also the 5th order non-linearity – Kerr lensing saturation, can influence the defocussing of filaments in air. The 5th order nonlinear refractive index n_4 of diamond [6] is one order of magnitude higher than that of the air [70], thus it is included in the present study. The nonlinear polarization envelope contains also the stimulated Raman scattering term as discussed in section 1.3. Thus:

$$\frac{\omega_0}{2n_0\epsilon_0 c}p_{nl} = \gamma_e|A|^2A + \theta|A|^4A + \gamma_R A\int_{-\infty}^{t} R(t-\tau)|A(\tau)|^2 d\tau. \tag{2.19}$$

The three consecutive nonlinear contributions in Eq. 2.19. are:

- self-phase modulation with $\gamma_e = k_0\epsilon_0 c n_2/2$, where n_2 is the nonlinear refractive index [19, 21, 23, 26, 27],
- self-phase modulation saturation with $\theta = k_0\epsilon_0^2 c^3 n_4/4\omega_0$ [50, 51, 71],
- stimulated Raman response with Raman responce strength coefficient (see section 1.3.):

$$\gamma_R = \frac{1}{\bar{\omega}^2+\gamma^2}\frac{\omega_0}{2n_0\epsilon_0 c}\frac{1}{2}N\left(\frac{\partial\alpha}{\partial q}\right)_0^2. \tag{2.20}$$

The medium response function in equation 2.19 is the Green's function of the forced and damped harmonic oscillator Eq. 1.8. normalized in such a way that its integral over time gives one [47, 72]:

$$R(t) = (\bar{\omega}^2+\gamma^2)G(t). \tag{2.21}$$

The value of nonlinear refractive index n_2 and Raman response strength coefficient γ_R at 800 nm were extrapolated from experimental data from reference [73] giving:

$$\gamma_e = 2.9 \times 10^{-17} \ \frac{\mathrm{m}}{\mathrm{V}^2} \tag{2.22}$$

and

$$\gamma_R = 1.1 \times 10^{-17} \ \frac{\mathrm{m}}{\mathrm{V}^2}. \tag{2.23}$$

From theoretical calculations [6] the value of higher order nonlinear coefficient is:

$$\theta = -6.9 \times 10^{-36} \ \frac{\mathrm{m}^3}{\mathrm{V}^4}. \tag{2.24}$$

The angular frequency of the diamond's single Raman line is $\bar{\omega} \approx 251$ THz (1332 cm^{-1}) and the vibration was measured [74] to decay with time constant of 5.7 ps, thus $\gamma \approx 175$ GHz.

2.3.4 Free current contribution

The ultrashort pulse of high intensity can photoionize the medium and thus create the free current even if the energy of light photons is below the ionization energy. This happens due to multiphoton absorption for low intensities and tunneling effect for high intensities. There is however no good model that would provide exact information on the shape of the photoionization rate as a function on the light intensity.

In this study the model developed by L. V. Keldysh in 1964 [75] for photoionization rate (W_{PI}) is used. Although results of some measurements differ even by four orders of magnitude from the results of Keldysh theory

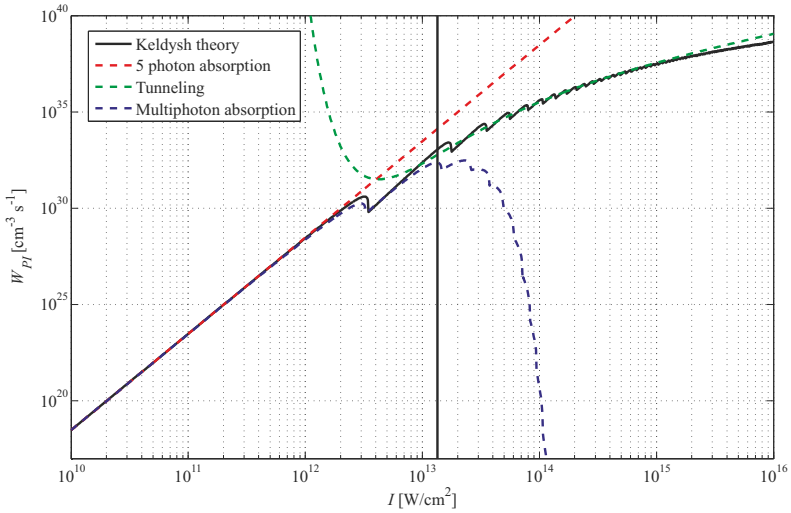

Figure 2.5: The photoionization rate of bulk diamond at 800 nm as a function of light intensity as calculated from Keldysh theory (black curve), the value of intensity for Keldysh parameter equal to 1 is indicated with black vertical line. The photoionization rates calculated from approximated formulas: tunneling for $\gamma << 1$ (green curve) and multiphoton absorption for $\gamma >> 1$ (blue curve) are also indicated together with the simplest approximation of five photon absorption (red curve). Non of the approximations is good in vincinity of intensity corresponding to $\gamma = 1$.

[76], and some alternative models have been developed [77] (but yet not verified), it is the most widely used model in supercontinuum generation simulations [39, 41, 43, 44, 51, 67].

The expression derived by Keldysh can model not only both: multiphoton absorption and tunneling intensity regimes at the same time, but also the transition region between the two processes. This is a special advantage as the supercontinuum generation in bulks can occur close to border between those regimes, where none of the approximations is valid.

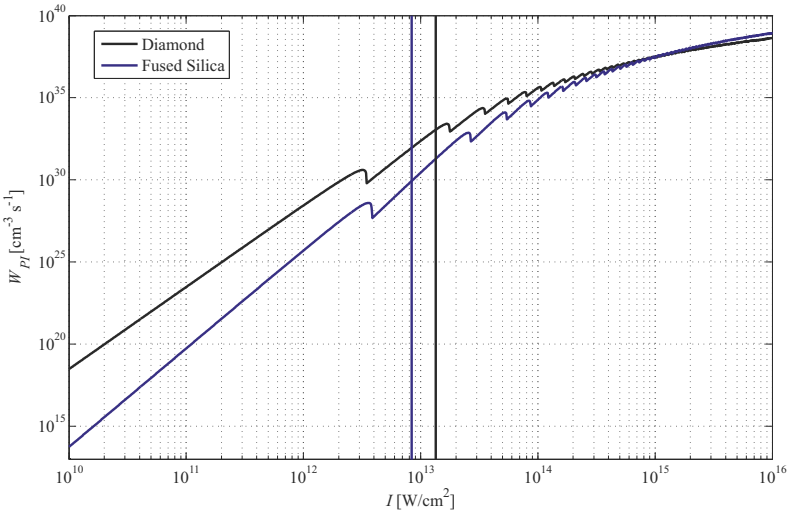

Figure 2.6: The photoionization rates of bulk diamond (black) and fused silica (blue) at 800 nm as a function of light intensity as calculated from Keldysh theory. Value of intensity for Keldysh parameter equal to 1 is indicated with black and blue vertical lines for diamond and fused silica, respectively.

The medium parameters required by Keldysh formula are the light angular frequency ω, the hole-electron reduced mass $m \approx 0.18 m_0$ [78], where m_0 is the free electron mass and the bang gap energy $E_g = 7.3$ eV [78]. From those parameters the dimensionless Keldysh parameter is formed:

$$\gamma = \omega \frac{\sqrt{m E_g}}{e|A|}, \tag{2.25}$$

where e is the elementary charge and A is the electric field amplitude. The two regimes: multiphoton absorption and tunneling effect can be recognized as limit cases of Keldysh theory for $\gamma >> 1$ and $\gamma << 1$, respectively.

The Keldysh expression for photoionization rate (number of carriers created in one second per unit volume) is as follows [75]:

$$W_{PI} = \frac{2\omega}{9\pi}\left(\frac{m\omega}{\gamma_1\hbar}\right)^{\frac{3}{2}} Q e^{-w\lfloor x+1\rfloor}, \tag{2.26}$$

where:

$$\gamma_1 = \frac{\gamma}{\sqrt{1+\gamma^2}},\ \gamma_2 = \frac{1}{\sqrt{1+\gamma^2}}, w = \pi\frac{K_1 - E_1}{E_2},\ x = \frac{2E_gE_2}{\pi\hbar\omega\gamma_1} \tag{2.27}$$

and

$$Q = \sqrt{\frac{\pi}{2K_2}}\sum_{n=0}^{\infty} e^{-nw}\Phi\left(\pi\sqrt{\frac{2\nu+n}{2K_2E_2}}\right), \tag{2.28}$$

with the Dawson function:

$$\Phi(z) = e^{-z^2}\int_0^z e^{y^2}dy, \tag{2.29}$$

where $\nu = \lfloor x+1\rfloor - x$ and $\lfloor a\rfloor$ stands for previous largest integer of a and

$$K_1 = K(\gamma_1^2),\ E_1 = E(\gamma_1^2),\ K_2 = K(\gamma_2^2),\ E_2 = E(\gamma_2^2), \tag{2.30}$$

where K and E are complete elliptic integrals of the first and second kind.

The photoionization rate of diamond at 800 nm as a function of light intensity calculated from above expressions is presented in Fig. 2.5. The rates calculated from approximated formulas [75] for tunneling and multiphoton absorption are also presented together with the simplest approximation of 5

photon absorption valid for low intensities:

$$W_{PI} = aI^5; \tag{2.31}$$

where $a = 3 \cdot 10^{-52} \left(\frac{\mathrm{m}^2}{\mathrm{W}}\right)^5$.

The comparison of photoionization rate of diamond and fused silica is shown in Fig. 2.6. In low intensity region the photoionization rate of diamond is much higher than that of fused silica. This is directly connected with the difference in band gap energy of two materials [53]. In diamond more charge carriers will be excited and faster defocusing than in fused silica should occur. In effect the generated spectrum should be less broad than that generated in fused silica. Indeed, this is exactly what was observed in the present study and discussed in section 2.2. Vibronic transitions exist in diamonds with impurities [79] and vacancies [80] they are however not expected in the present case.

Apart from the photoionization, the interaction of light with plasma fluid has to be included into the nonlinear envelope equation. This is accomplished by use of the Drude model [81], where the Newton's law for the free charge is used:

$$m\frac{\partial^2 \vec{x}}{\partial t^2} + \frac{m}{\tau_c}\frac{\partial \vec{x}}{\partial t} = q\vec{E}, \tag{2.32}$$

where m is the charge mass, $\vec{x}$ its coordinates, t is the time, τ_c is a carrier collision time, q is the charge value and $\vec{E}$ is the electric field of light. If the current $\vec{J} = \rho\frac{\partial \vec{x}}{\partial t}$, where ρ is the free-carrier plasma density, is used, the

above equation becomes:

$$\frac{\partial \vec{J}}{\partial t} + \frac{1}{\tau_c}\vec{J} = \frac{q^2}{m}\rho\vec{E}. \tag{2.33}$$

This equation can be solved to give the expression for current envelope:

$$\frac{1}{2n_0\epsilon_0 c}j = \frac{\sigma}{2}(1 + i\omega_0\tau_c)\hat{G}^{-1}\rho A, \tag{2.34}$$

where $\sigma = \frac{e^2\tau_c}{n_0 c\epsilon_0 m(1+\omega_0^2\tau_c^2)}$ is the cross section of inverse Bremsstrahlung (inverse deceleration radiation [66]) and

$$\hat{G}^{-1} = \sum_{m=0}^{\infty}\left(\frac{-ig}{\omega_0}\partial_t\right)^m \approx \left(1 - \frac{ig}{\omega_0}\partial_t\right) \tag{2.35}$$

is the inverse of the free-charge dispersion operator as derived in [41] with $g = (-i\omega_0\tau_c)/(1 - i\omega_0\tau_c)$. The terms with higher order derivatives can be neglected if g is small. If fact as the collision time in diamond was found to be $\tau_c = 360$ ns [82], the g is close to 1. Thus, to simplify numerical calculations we use only two first components of $\hat{G}^{-1}$ expansion.

Finally, the following expression for free-current similar to that derived by Gulley et al. [41] is used for the slowly varying free-current envelope:

$$\frac{1}{2n_0\epsilon_0 c}j_{fc} = \frac{W_{PI}(|A(t)|)E_g}{2I(t)}A + \frac{\sigma}{2}(1 + i\omega_0\tau_c)\hat{G}^{-1}\rho A, \tag{2.36}$$

where $I(t) = n_0\epsilon_0 c|A(t)|^2/2$ is the light intensity.

2.3.5 Plasma density

As the plasma density is included in the nonlinear envelope equation, additional equation has to be solved in the simulation. In fact, this additional equation is the rate equation for the medium. The three important phenomena can be included in the equation for plasma density: the photoionization, avalanche ionization and plasma decay. Avalanche ionization occurs when photoionized electrons accelerated in the electric field collide with ions or electrons in the valence band and excite new charge carriers. Avalanche ionization is considered to have minor effect for pulses shorter than 100 fs [45], thus the avalanche ionization is neglected in this study. The plasma decay is a slow effect and, thus, it is also neglected. Finally the free-carrier plasma density equation used in this study includes only photoionization:

$$\frac{\partial \rho}{\partial t} = W_{PI}(|A|). \tag{2.37}$$

2.3.6 The input pulse

The quality of the beam from the amplifier allows one to use the Gaussian function to model its spatial and temporal shape. As diamond is isotropic, the field intensity can be modeled as cylindrically symmetric. To create the input beam distribution first, the beam with the flat wavefront (the beam in the focus) is calculated:

$$A(r,t) = A_0 e^{-\frac{r^2}{w_0^2} - \frac{(1+iC)t^2}{2\sigma^2(1+C^2)}}, \tag{2.38}$$

where r is the distance from the optical axis, A_0 is the maximum of the electric field, $w_0 = 7\mu$m is the beam waist in the focus, C is dimensionless time chirp parameter and σ is the time width of the pulse. Then it is numerically back-propagated in vacuum conditions by 3.7 mm to generate the pulse of similar waist (150 μm) and convergence as in the experiment.

2.4 Simulation details

Most common method of solving propagation problems, also used in this thesis, is the split-step Fourier method [32]. The NEE can be presented in the following form:

$$\frac{\partial A}{\partial z} = (\hat{L} + \hat{N}(A))A, \tag{2.39}$$

where $\hat{L}$ is a linear operator:

$$\hat{L} = \left(i\hat{D}\frac{i}{2k_0}\hat{T}^{-1}\nabla_{\perp}^2 \right), \tag{2.40}$$

and $\hat{N}(A)$ is a nonlinear operator:

$$\hat{N}(A) = \frac{1}{A}\left(i\frac{\omega_0\hat{T}}{2n_0\epsilon_0 c}p_{nl} - \frac{1}{2n_0\epsilon_0 c}j_{fc} \right). \tag{2.41}$$

The equation 2.39 can be transformed into

$$\frac{dA}{A} = \left(\hat{L} + \hat{N}(A) \right) dz, \tag{2.42}$$

and solved approximately for small dz:

$$A(z+dz) \approx A(z)e^{\left(\hat{L}+\hat{N}(A(z))\right)dz} \approx A(z)e^{\hat{L}dz}e^{\hat{N}(A(z))dz}, \tag{2.43}$$

where the dz^2 and higher order dependent contributions coming from Baker-Campbell-Hausdorff formula, proportional to commutator of the two operators $[\hat{L}, \hat{N}(A)]$ were neglected. The split-step Fourier method of obtaining the solution at $z_{k+1} = z_k + dz$, knowing the solution at distance z_k is as

follows:

$$A(z_{k+1}) = e^{\hat{N}(A(z_k))dz}\ \hat{S}_T^{-1}\left\{e^{\tilde{\hat{L}}dz}\ \hat{S}_T\left\{A(z_k)\right\}\right\}, \tag{2.44}$$

where $\hat{S}_T$ is the operator of transformation into the spectral space and $\tilde{\hat{L}} = \hat{S}_T\{\hat{L}\}$.

The scheme of the method is simple, however there are a few aspects of the method which require further discussion. These are:

- The main advantages of the split-step Fourier method which is the evaluation of the linear operator $\hat{L}$ in the spectral space.

- The way of transformation into the spectral space in case of cylindrical symmetry.

- The fact that in-spite that all the derivatives in $\hat{L}$ are evaluated in the spectral space, the derivative operator in $\hat{N}$ is calculated with use of finite-difference method.

- the way of error estimation.

- The marching scheme – the method of choosing of the step size dz.

- The way of solution of the free-current equation.

After a short note on discretization of the field envelope, above subjects are discussed in the next few sections, later the details on implementation of the method and its tests are given.

2.4.1 Discretization

The nonlinear envelope equation 2.3. is a partial differential equation, of the first order in the propagation coordinate and of higher order in time and radial coordinate. For its numerical solution the discretization of electric field envelope in both space and time is required. The complex amplitude of the electric field is discretized over time and radial coordinate to form a grid (or matrix) of equally separated points:

$$A_{ij}(z) = A(t_i, r_j, z), \tag{2.45}$$

the nonlinear envelope equation is solved to obtain $A_{ij}(z_k)$ for different not equally separated points (z_k) along the propagation coordinate.

2.4.2 Evaluation of the linear operator $\hat{L}$ – pseudospectral method

Split-step Fourier method is a pseudospectral method [83]. This means that the derivatives with respect to time and space are evaluated in the spectral space:

$$\partial_t^m \xrightarrow{F_T} (i\omega)^m, \quad \nabla_\perp^2 \xrightarrow{H_T} -k_r^2. \tag{2.46}$$

where F_T and H_T are Fourier and Hankel transform (see below), respectively. The linear operator for NEE:

$$\hat{L} = i\hat{D} + \frac{i}{2k_0}\hat{T}^{-1}\nabla_\perp^2, \tag{2.47}$$

contains second order derivatives over spatial coordinates ($\nabla_\perp^2 = \frac{1}{r}\partial_r(r\partial_r)$ in cylindrical coordinates) but it also contain an infinite set of derivatives over time (due to dispersion operator $\hat{D}$ see section 2.3.2.), and an inverse of the steepening operator $\hat{T} = \left(1 + \frac{i}{\omega_0}\frac{\partial}{\partial t}\right)$. Therefor obviously it can't be evaluated in time space and has to be transformed into spectral space with use of Eq. 2.46. then:

$$\tilde{\hat{L}}(\omega, k_r) = i\left(k(\omega) - (k_0 + \omega k_1)\right) - \frac{i\omega_0 k_r^2}{2k_0\left(\omega_0 - \omega\right)} \tag{2.48}$$

While transition from time to frequency is done with Fourier transform, transition to wavevector space with cylindrical variables has to be done with Discrete Hankel Transform of order 0 [84]. Hankel Transform expresses a function as the weighted sum of an infinite number of Bessel functions of the first kind:

$$\tilde{A}(k_r) = 2\pi \int_0^\infty r A(r) J_\nu(k_r r) dr, \tag{2.49}$$

$$\tilde{A}(r) = 2\pi \int_0^\infty k_r \tilde{A}(k_r) J_\nu(k_r r) dk_r, \tag{2.50}$$

where J_ν is the Bessel functions of the first kind of order ν.

The Fourier transform could be evaluated with so called Fast Fourier Transform (FFT) algorithm, which requires $O(N \log N)$ operations with N being the number of signal discrete points. There is however no accurate "fast" Hankel transform [85] and thus the discreet algorithm equivalent to matrix multiplication with $O(N^2)$ operations has to be used. Since the multiplication by Hankel transform's matrix is already required there is no advantage of using FFT, instead the matrix for Fourier Transform is combined

with that of Hankel transform:

$$\tilde{A}_{lm} = \left\{ \sum_j H_{mj} \left\{ \sum_i F_{li} A_{ij} \right\}^T \right\}^T = \sum_i j H_{jm} F_{li} A_{ij}, \tag{2.51}$$

where $A_{ij} = A(t_i, r_j)$, $\tilde{A}_{lm} = \tilde{A}(\omega_l, k_{rm})$ and H_{mj} and F_{li} are the elements of the Hankel and Fourier transform, respectively. Then:

$$\tilde{A} = \hat{H}^T \hat{F} \hat{A} = \hat{S}_T \hat{A}, \tag{2.52}$$

where $\hat{S}_T = \hat{H}^T \hat{F}$ is a combined single transform operator whose elements can be calculated once before the simulation.

The nonlinear operator of NEE:

$$\hat{N}(A) = \frac{1}{A} \left(i \frac{\omega_0 \hat{T}}{2 n_0 \epsilon_0 c} p_{nl} - \frac{1}{2 n_0 \epsilon_0 c} j_{fc} \right), \tag{2.53}$$

contains time derivatives over local time: the $\hat{T}$ in polarization and $\hat{G}$ in the free current operators. In this study those derivatives are evaluated directly in the time space with use of so called "five-point stencil" approximation (finite difference approximation of order 4) [86]:

$$f'(t) \approx \frac{1}{12h}(f(t-2h) - 8f(t-h) + 8f(t+h) - f(t+2h)), \tag{2.54}$$

where h is the time step between points of function f discretization. The error of this derivative approximation scales with h^4. The motivation of

using "five-point stencil" and therefore mixing of a pseudospectral and finite difference method is the speed of the evaluation.

2.4.3 Method accuracy, error estimation and the marching scheme

The error of the split-step Fourier method as formulated above scales with $\frac{1}{dz^2}$ for a single step This can be improved with use of so called symmetric split-step Fourier method [32] with scheme:

$$A(z_{k+1}) = \hat{S}_T^{-1}\left\{e^{\tilde{\hat{L}}\frac{dz}{2}}\ \hat{S}_T\left\{e^{\hat{N}(A(z_k))dz}\ \hat{S}_T^{-1}\left\{e^{\tilde{\hat{L}}\frac{dz}{2}}\ \hat{S}_T\left\{A(z_k)\right\}\right\}\right\}\right\}, \quad (2.55)$$

where application of linear operator is done in half-steps before and after application of nonlinear operator. The error of the symmetric split-step Fourier method for single step scales with $\frac{1}{dz^3}$. Additional improvement can be obtained by combination of forward and backward propagation or by summing solutions obtained in different ways with appropriate weights. For example, a 5th order method, where error for single step scales with $\frac{1}{dz^5}$, can be obtained, if after four forward steps of size dz, a single $2dz$ step backward and another four forward dz steps are made [42]. In this case the 4th order contributions to the error cancel out.

The other option, used in this study, is as follows. Basing on the solution from the previous step $A(z_{k-1})$ the solution at the next point $A(z_k)$ is calculated in two ways. One, so called coarse solution A_c, is obtained by the single step $dz = z_k - z_{k-1}$ with the split-step symmetrical method of order 3. The other on, called a fine solution A_f, is obtained similarly but in two

steps of size $\frac{dz}{2}$. The final solution is calculated as a weighted sum:

$$A(z_k) = \frac{4}{3}A_f - \frac{1}{3}A_c, \tag{2.56}$$

giving a method of order 4 [87]. The main reason for using this method will become easy to understand after discussion of possible step-size control schemes.

The way, in which the size of the steps taken along the propagation direction is determined, is crucial when the split-step Fourier method is used. The wrong choice of step control method can influence both the computation time and accuracy of the result dramatically. Here two major strategies: constant step size and "local-error step-size control", are reviewed while some other methods are mentioned.

The step size can be set as constant at the beginning of simulation and may be changed after simulation if for example some error estimation condition is not met. In such a case the whole simulation has to be performed once again from the beginning with the new step size. The advantage of constant step-size method is that not only the linear operator but the whole expression $e^{\hat{\tilde{L}}dz}$ is constant and, thus, can be evaluated once per simulation. This method is optimal for problems where $\frac{\partial A}{\partial z}$ vary little in consecutive steps. This is the case, for example, of nonlinear propagation and supercontinuum generation in fibers where diffraction is not considered. It is, however, far from optimal when the beam focusing is modeled. The intensity of convergent and divergent beams far from the focus changes quadratically with distance and so the nonlinear phase change is very position dependent. It is

thus preferable to perform dense steps in vicinity of the focus while sparse steps should be made far from this region.

Some interesting methods can be developed for constant step size strategy. These are in particular Predictor-Corrector split-step methods of different orders [42]. In those methods, in order to evaluate solution at z_k the solutions at multiple previous steps z_{k-1}, z_{k-2}, ... , z_{k-m} (where m is the method's order) are used. This way, with keeping the computation speed constant, the accuracy of the method is improved.

The variable step size methods require a suitable error estimation scheme. A common approach used often for co-propagation of beams, subjected to second order mixing processes, is the energy conservation condition. In supercontinuum generation process, however, the energy is not conserved. Other common approach, called Nonlinear Phase-Rotation Method, is to monitor and limit the nonlinear phase acquired by the pulse in a single step with its maximal allowed value φ_{NL}^{Max}. Then the size of the step is calculated as:

$$dz \leq \frac{\varphi_{NL}^{Max}}{\Im \hat{N}(A)}, \tag{2.57}$$

where $\Im \hat{N}(A)$ stands for imaginary part of $\hat{N}(A)$. This method is particularly good in problems where $\hat{N}(A)$ is purely imaginary, for example soliton propagation [87]. In supercontinuum generation process this is also not the case, mainly because of the photoionization term present in $\hat{N}(A)$.

Thus, another approach is required and this approach will use the coarse and fine solutions as calculated in the manner explained at the beginning of this section. This method is called "local-error step-size control" and was

developed by Sinkin et. al. [87]. Then, so called relative local error can be calculated for each step:

$$\delta = \frac{\|A_f - A_c\|}{\|A_f\|}, \tag{2.58}$$

where:

$$\|A\| = \int_{-\infty}^{\infty} |A|^2 dt, \tag{2.59}$$

is the norm of the solution. The relative local error can be used for step-size correction. The step-size is reduced or increased to keep the relative local error close but always below some given goal error. The "local-error step-size control" method has the crucial advantage over other discussed ones for the case of supercontinuum generation. Namely no considerations on physical properties of the system, like energy or nonlinear phase, are required here. Figure 2.7. presents the step-size chosen by the local-error step-size control algorithm together with the change of the pulse energy during propagation in diamond. In vicinity of the region, where the beam is most focused and thus most energy is absorbed by multiphoton ionization, the steps are dense.

An important alternative to the split-step approach is to threat the equation 2.39 as a set of ordinary differential equations in Fourier space. Then it can be solved by standard explicit methods like Runge-Kutta of the 4th order or by Adams-Bashforth method of the 3th order with constant step size[2]. Adaptive step-size Runge-Kutta of order 5 would be the method of choice for the supercontinuum generation problem, where the step size should vary significantly. However, these methods require more random access memory than the split-step method [56]. In the present study the calculations were

[2]Most of the second order methods were shown to poses computational instabilities for pseudospectral methods [83].

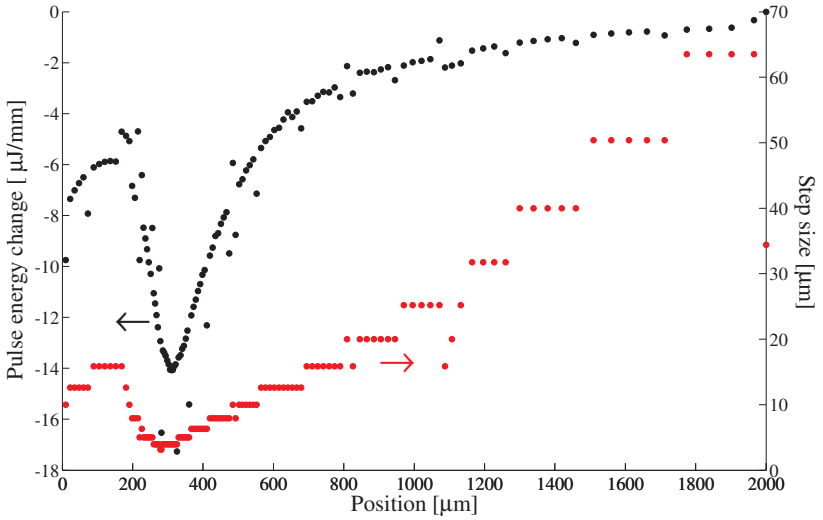

Figure 2.7: The step-size chosen by the local-error step-size control algorithm and the change of the pulse energy during propagation in diamond. The steps are dense in of the region where the most energy is absorbed by multiphoton ionization.

performed on the graphical processing unit with a limited random access memory, therefore, the split-step method was chosen.

2.4.4 The ordinary differential equation of plasma density

The solution of ordinary differential equation of plasma density Eq. 2.37. is the most computationally intensive part of the simulation, even thou all plasma density dependent terms from the right side of the equation were neglected in this study (see section 2.3.5).

For a given radial coordinate r_j the nonlinear function of local time $W_{PI}(|A_j(t)|)$ has to be evaluated and the equation:

$$\frac{\partial \rho_j(t)}{\partial t} = W_{PI}(|A_j(t)|), \tag{2.60}$$

has to be solved to give the plasma density $\rho_{ij} = \rho(t_i, r_j)$ at every local time point t_i. During solution of this equation the value of function $W_{PI}(|A_j(t)|)$ at times other than t_i (therefore in between the grid points) is calculated for linearly interpolated value of slowly varying envelope A.

It was found that for pulses with high intensities this equation becomes stiff [88]. It means that the explicit methods used for ordinary differential equations fail to solve it as the time step required becomes too small for numerical calculations to work. Thus an implicit method of solution was implemented.

The implicit methods of solving ordinary differential equations require an approximate solution of the nonlinear algebraic equations system. This is done with a Newton iteration method which requires matrix inversion. The implementation of this kind of method is in general complicated thus the simplest approach with a constant time step-size and a fixed number of Newtonian iterations was implemented. As will be explained in the next section the equation 2.3.5. is solved for many radial coordinate values in parallel. This is an additional reason for above simplifications.

As the step-size is kept constant it is good to use a high order method to ensure high accuracy of solution. The implicit Runge-Kutta Radau IIA method [88], which is of order 5 (the error of the method scales with 5th power of step-size), was chosen for this study. This is a three stage method,

which means that to compute the solution at $t_{i+1} = t_i + dt$ the right side of equation 2.3.5. is evaluated three times (at $t_i + 0.2586\ dt$, $t_i + 0.5414\ dt$ and $t_i + dt$ for Radau IIA).

Radau IIA is an L-stable method [88] which means that it is particularly accurate for the case of fast changing $W_{PI}(|A_j(t)|)$.

2.4.5 Implementation

The symmetric split-step Fourier method with local-error step-size control was implemented in MATLAB environment and in the graphical card native CUDA C programming language The computation can be performed both with use of computers central processor units (CPU) and on the graphical card processing units (GPU). When CPU is used for computation the plasma equation is solved with MATLAB build in implicit solver. Special implementation of Radau IIA method for GPU was created. It performs parallel solution of a given equation for different values of parameters and initial conditions (see appendix A). The plasma equation (2.37) is solved at every propagation step for all r's and t's with Runge-Kutta method. The field envelope $A(r, t)$ is discretized into grid of 1024 time points and 512 radial points (524288 points all together). For local error of 10^{-3} about 150 steps were made with step sizes going from 40 to 100 μm.

2.4.6 Model testing

The model of propagation based on nonlinear envelope equation has the advantage of modularity. The consecutive terms in the equation can be removed to test the simulation code against known numerical or analytical

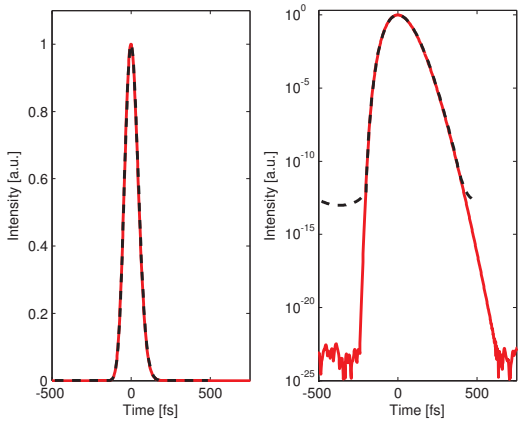

Figure 2.8: Temporal profile of the intensity of a 10 fs Fourier limited pulse which traveled through 10 mm fused silica, all orders of dispersion are modeled. The results of the present model - red solid curve, and of Lab2 simulation - black dashed curve are presented both in linear and logarithmic scale. Differences (at levels close to 10^{-12}) between the two plots visible in the log scale are caused by the higher accuracy of the present model.

results. Such tests were performed for the present code. For most cases only one term (like for example only dispersion term, or only self-phase modulation term) is left in the equation for the test.

First a set of tests were performed for plain waves – a one dimensional simulation. The common error in propagation codes (observed by the author in students' and coworkers' codes) is the wrong assignment of the time and frequency axes directions. This is indeed not intuitive and can be easily missed as it is frequently enough to consider only the second order of dispersion and self-phase modulation in the model and both of these effects cause symmetrical modification of the pulse. The propagation of a Gaussian pulse in the medium with self-phase modulation and self-steepening term is a good test for presence of this flaw. It is well known [32] that the self-steepening

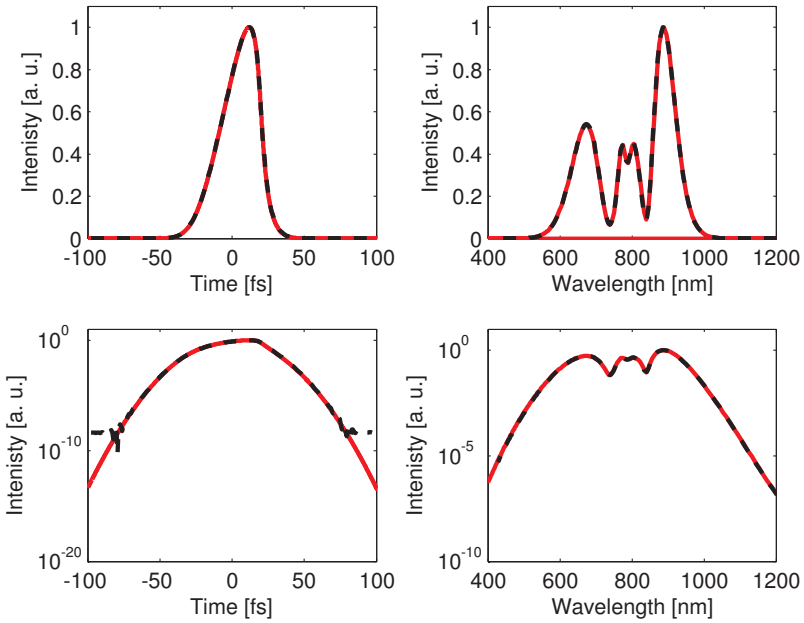

Figure 2.9: Intensity time and wavelength profiles of a 40 nJ, 30 fs Fourier limited pulse which traveled through 5 mm of fused silica plate with a $10\mu m$ beam waist. Both self-phase modulation and self-steepening effects are included. Results of the present model - red solid curve, and of the Lab2 simulation - black dashed curve are presented both in linear and logarithmic scale.

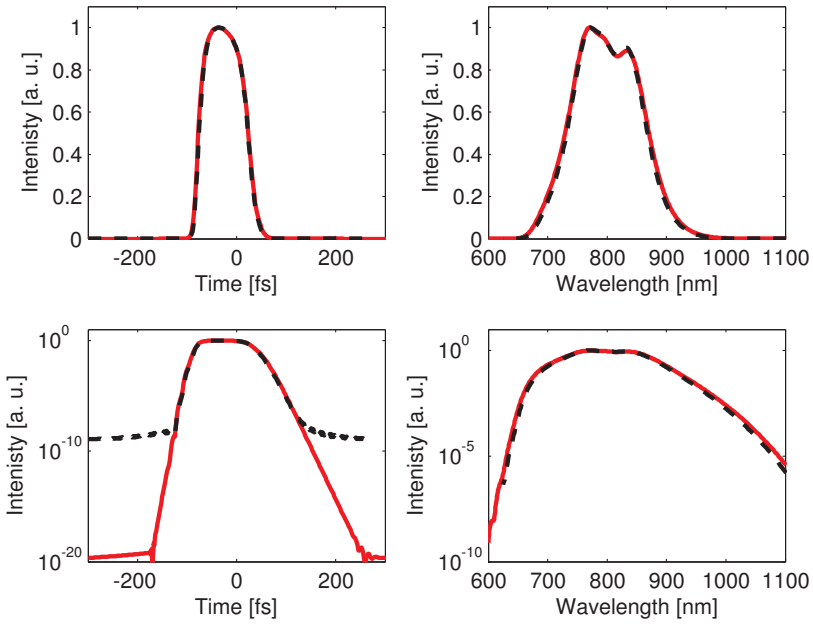

Figure 2.10: Same as figure 2.9. but with dispersion included.

alone leads to the formation of the shock – an extremely steep edge of the pulse and this edge is located at the back of the pulse. Additionally the spectrum of such a pulse is asymmetrical with respect to the initial central frequency, namely – the spectrum is elongated towards high frequencies [32]. The presence of the third order dispersion causes just the creation of fringes at the tail of the pulse [32] and it is much easier to introduce it in the simulation than the self-steepening term. However the flaw in the propagation in the medium with the third order dispersion can be masked by simultaneous wrong assignment of the directions of the two axes. The result of propagation of a Gaussian pulse in the dispersive medium with second order dispersion was calculated analytically. The results of propagation of arbitrary pulse in dispersive medium with all orders of dispersion included (Fig. 2.8.), effect of self-phase modulation, self-steepening (Fig. 2.9. and 2.10.) and stimulated Raman scattering in fused silica were compared with the results obtained by use of the Lab2 Library [89]. The ordinary differential equation of the free-current generation was solved for tests with number of MATLAB built in routines. The blue shifting and absorption of highly intense light due to interaction with the current was checked.

The two dimensional test of the diffraction of different spatial Gauss-Lageure modes in vaccume and medium was compared with analytical solutions.

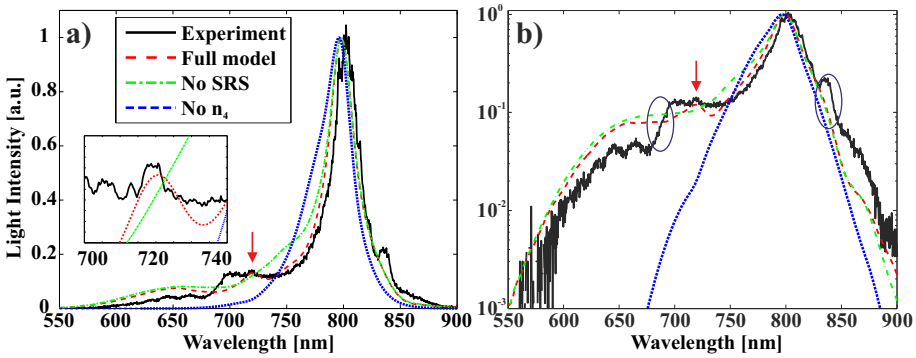

Figure 2.11: Experimentally measured spectrum of supercontinuum (solid black line), simulation with all contributions included (red dashed line), without stimulated Raman scattering term (green dashed and dotted line), without n_4 nonlinearity (blue dotted line) in linear (a) and logarithmic (b) scale. The stimulated Raman scattering peak is designated with red arrow. The inset presents enlarged vicinity of that peak. The features which could not be reproduced by simulation are marked with circles.

2.5 Modeling results

2.5.1 Correspondence with experiment results

The comparison of simulation results for different simulation conditions with experimental spectrum measured for input energy 22.5 μJ is presented in Fig. 2.11. The inclusion of higher order nonlinearity is crucial for obtaining resemblance between the model and the measured data. The simulation result for the case when this term is neglected is presented in Fig. 2.11 with a blue curve.

It was found that only with inclusion of the stimulated Raman response the model reproduces anti-Stokes peak around 720 nm. The red and green curves in Fig. 2.11 present the simulation results with and without this term, respectively. This fact confirms the belief that the stimulated Raman scat-

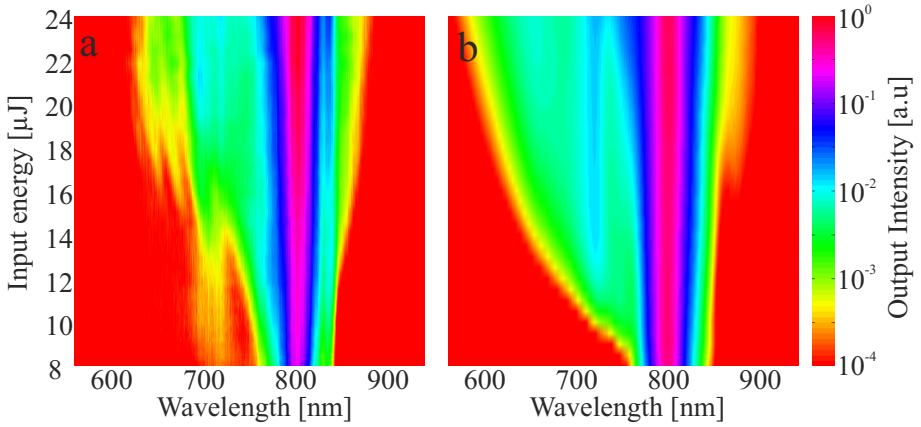

Figure 2.12: Spectra of generated supercontinua as a function of input energy measured in experiment (a) and reconstructed from the simulation (b).

tering can be easily observed in the spectrum of supercontinuum generated in diamond.

The simulation with all terms included resembles the experimental results in the best way, this can be seen both in linear and logarithmic scale in 2.11. (a) and (b), respectively. The origin of the intensity slope around 675 nm and the feature around 840 nm (marked with circles in Fig. 2.11.) could not be resolved in the present model.

The simulation with all terms included was performed for the range of input pulse energies. The results of this simulation are presented in Fig. 2.12. (b) next to experimental data (Fig. 2.12. (a)). The general behavior is well reproduced. But as seen here the intensity slope around 675 nm is not reproduced for all the energies. Consequently the simulated short wavelengths plateau extends further into the short wavelengths direction than the measured one. Also the intensity dependent fringes on the short wavelengths

side of the spectrum are not reproduced in the simulation. Their possible origin will be explained in section 2.5.3.

2.5.2 The pulse evolution during the propagation – importance of self-focusing saturation

The inclusion of higher order nonlinearity is crucial for obtaining resemblance between the model and the measured data. In absence of the self-focusing saturation the strong focusing occurs through the whole sample length (see blue curve in Fig. 2.13). In this case the intensity grows and causes excessive self-phase modulation and self-steepening. The self-phase modulation itself would cause generation of new frequencies on both sides of central frequency but as self-steepening is also considered the high frequencies are created more efficiently than the low ones. With strong focusing the absorption due to photoionization efficiently reduces the intensity of newly created frequencies and the central peak. The result of interplay of this effect is a substantial broadening of the spectrum towards the blue side while the blue side plateau is absent (see blue curve in Fig. 2.11).

In the present study the value of n_4 was a free parameter. Its final value ($n_4 = -3.3 \cdot 10^{-40} \frac{\mathrm{m}^4}{\mathrm{V}^4}$) was found to be higher from theoretically calculated (-$0.24 \cdot 10^{-40} \frac{\mathrm{m}^4}{\mathrm{V}^4}$) [6] by one order of magnitude. The inclusion of n_4 contribution suppresses self-focusing in the critical moment when the short wavelength plateau is created. But both: the 4th order nonlinearity and the plasma effect can suppresses self-focusing. It is thus difficult to distinguish which of the two processes is in fact underestimated. It is easy to alter the value of a parameter n_4 while it is difficult to develope the photoionization model.

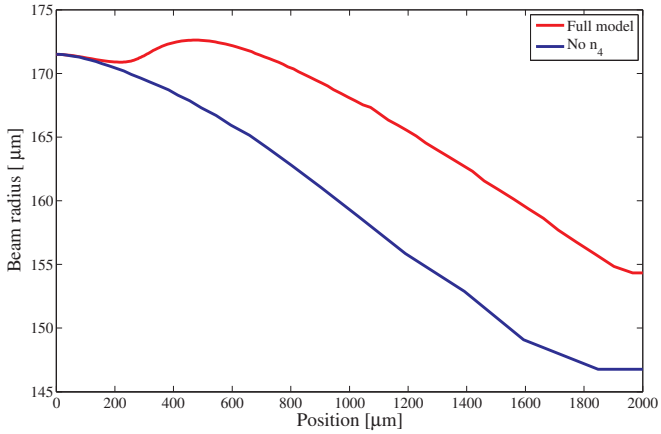

Figure 2.13: The simulated evolution of the beam radius during propagation in diamond with all contributions included in the calculation (red curve) and with neglected self-focusing saturation (blue curve). In the first situation the local minimum of the beam radius is visible at 300 μm, further focusing is stopped by saturation of self-focusing and the beam diverges until 500 μm when it becomes convergent again.

Therefore the decision of keeping the Keldysh model and varying the value of n_4 was made for the purpose of this study. The possibility of higher (than in Keldysh theory) photoionization rate in high laser field intensities regime has been, however, discussed in other studies (see [77] and the references therein) and thus it should be kept in mind.

The behavior of supercontinuum beam radius with and without self-focusing saturation is presented on Fig. 2.13. The beam radius R is defined here to fulfill the energy condition:

$$\int_0^R r|A|^2 dr = (1 - e^{-2}) \int_0^\infty r|A|^2 dr,$$

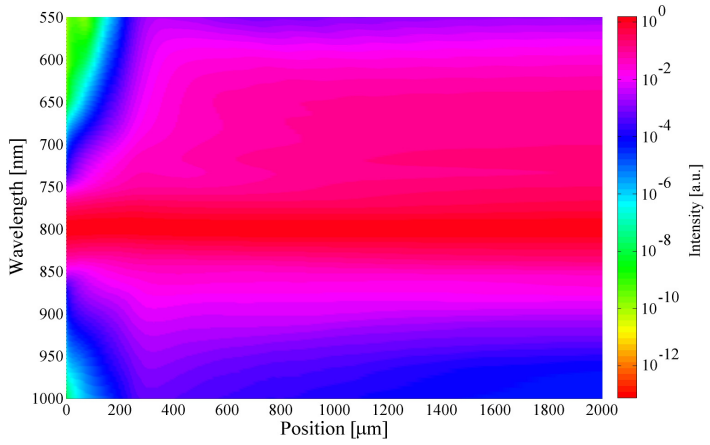

Figure 2.14: The simulated evolution of the pulse spectrum during propagation in diamond. The significant broadening occurs at a short distance at about 300 μm.

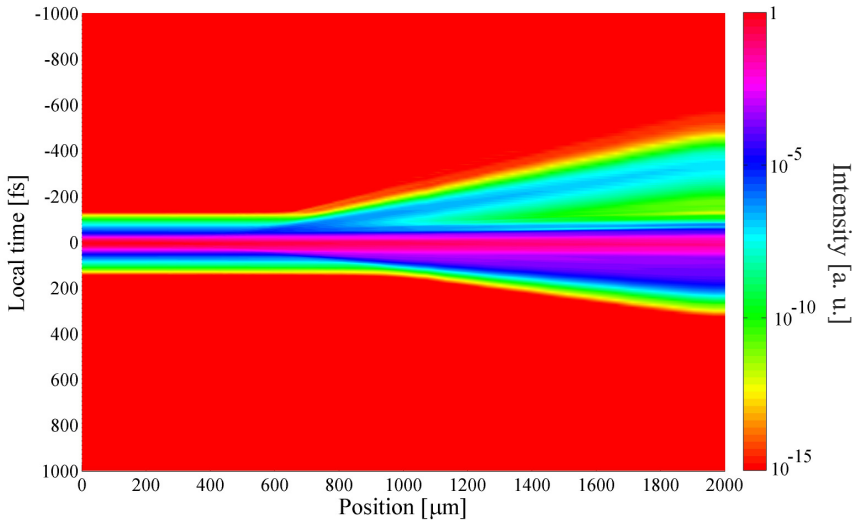

Figure 2.15: The simulated evolution ot the pulse time profile during propagation in diamond. Newly created frequencies travel at different velocities in the medium and the pulse becomes broad in time.

thus in circle of radius R the e^{-2} of the beam energy is situated (for Gaussian beam R is equivalent to beam width). If all the contributions are kept in the simulation the beam radius has a local minimum situated close to 300 μm. At this distance the actual generation of the broad spectrum occurs. This can be seen in Fig. 2.14 where the simulated evolution of the spectrum through the sample is visualized. Here the photoionization is most efficient causing significant pulse energy change (see Fig. 2.16. and Fig. 2.7.). As the pulse energy is reduced the energy dependent self-focusing also becomes less significant. After this point the focusing is stopped and the beam diverges until the self-focusing term again becomes more significant than its saturation term (500 μm see Fig. 2.13). The newly generated frequencies travel at different velocities in the medium and the pulse becomes longer (see Fig. 2.15). Finally, the beam focuses again, but its energy is already too low and the pulse itself is too long for the second extreme broadening to occur within the medium length.

The simulation result, showing that the actual supercontinuum generation (spectrum broadening) in the standard experimental configuration occurs at a short distance, several hundred microns from the medium interface, is consistent with the experimental [53, 55] observations and modeling [50, 67] from supercontinuum generation in other media.

2.5.3 Chirp and the intensity dependent fringes

By changing the pulse chirp in the simulation, one can reproduce intensity dependent spectral fringes which are visible on the short wavelength side in the experiment. Figure 2.17 presents the results of the simulation for different

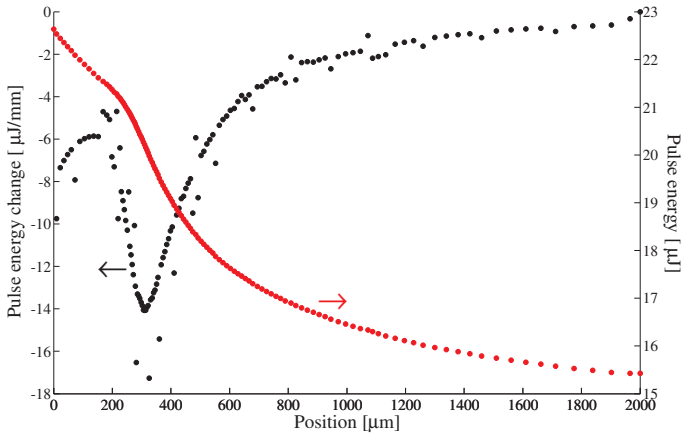

Figure 2.16: The simulated pulse energy and it's change along the sample. The beam is attenuated (due to photoionization and interaction with plasma) the most around 300 μm.

values of chirp parameter. For negative values the spectral fringes become stronger. However, as the exact shape of experimentally observed fringes (see Fig. 2.12(a)) could not be reproduced, for clarity, unchirped pulses in the above considerations.

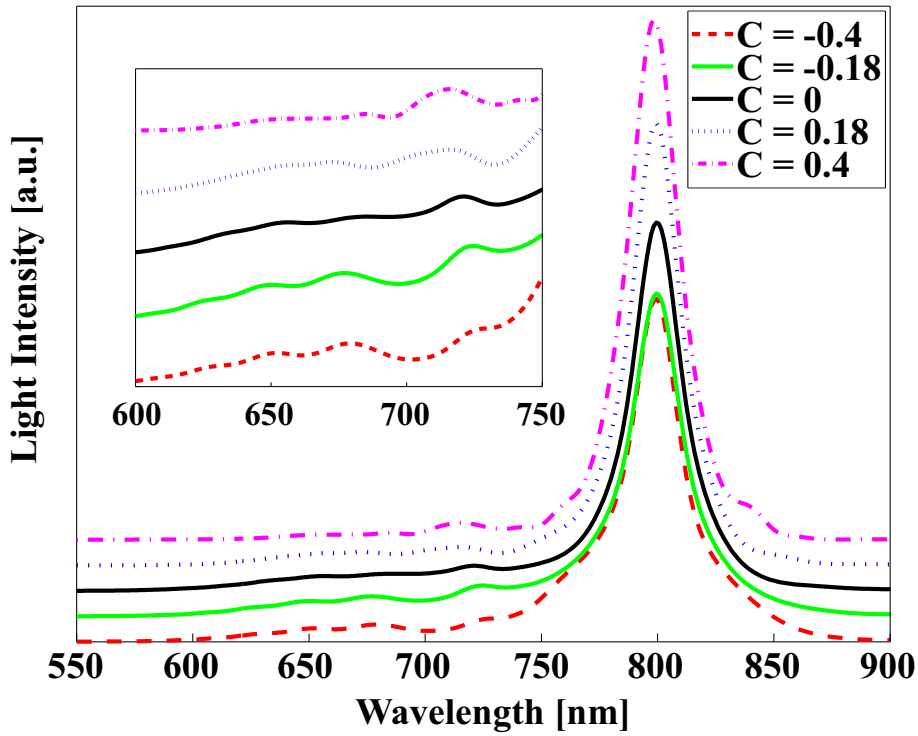

Figure 2.17: Results of the simulation for different values of chirp parameter C. The fringes on the short wavelength site of the spectrum become more pronounced for negative values of chirp (see the inset). For clarity the spectra are vertically shifted from each other.

2.6 Conclusion

In this chapter the experimental data on supercontinuum generation in the bulk diamond crystal were presented. The experimental results were described by means of the nonlinear envelope equation and particular nonlinear effects were analyzed showing that in the case of diamond the effects of stimulated Raman scattering on the supercontinuum spectrum can be observed. In the experiment it manifests itself mainly in the presence of a peak shifted by 1332 cm^{-1} from the pulse central frequency, what has been successfully reproduced by the model. The fact, that in the case of diamond the stimulated Raman response weakly influences the generated supercontinuum spectrum, confirms reasonability of neglecting its influence in other bulks, like fused silica or sapphire, where Raman gain is much weaker.

The data cover a wide range of input energies from below the supercontinuum generation threshold to the range where multiple filamentation appears. The spectrum of supercontinua generated in this range are limited to 600 nm at their blue side, therefore, it seems that diamond can not compete with sapphire, fused silica, CaF_2 r other media broadly used for white light generation with pulses from laser amplifiers. This fact, however, do not exclude the possibility of using diamond supercontinuum in various applications, like spectroscopy, optical coherent tomography or carrier-envelope phase stabilization. No studies of supercontinuum generation in diamond were performed in the infrared region and with other sources of pulses like femtosecond laser oscillators. As the yterbium based laser systems become more and more popular a specially interesting subject would be the generation with infrared pulses from such systems.

Chapter 3

Intramolecular vibrational relaxation and transient vibrational inversion of population in trans-β-apo-$8'$-carotenal

Carotenoids are one of the most frequent natural pigments [90]. The dynamics of the electronic states of carotenoids attracts much interest due to the crucial role it plays in photosynthesis processes. Carotenoids absorb green and blue light efficiently and the energy of their excitation can be transfered to chlorofills. Some of the carotenoids also act as photo-protectors against dangerous singlet oxygens and triplet chlorofill states [91]. These states appear during the photosynthesis when the intensity of light is significant and

can damage the reaction center of the light-harvesting protein complexes, The excess energy can however be absorbed and emited by carotenals as heat.

The light-harvesting function of carotenoids was discovered in 1943 [92], and it was shown that the quantum yield of the energy transfer to chlorofills can be as high as 90 % [91]. In 1972 the presence of the first "dark" state lying between ground and absorbing state, now known as S_1, was discovered [93,94] (see Fig. 3.1). It is now known [91, 95, 96] that the mechanism of the energy transfer to chlorofills involves two excited electronic states: a short living S_2 state, to which the excitation occurs and a long living S_1 from which the energy can be efficiently transferred.

In the resent years the nature of the fast $S_2 \longrightarrow S_1$ transition, preceding the energy transfer to other molecules, is under extensive study. All: infrared transient absorption techniques [90, 96–103], visible transient absorption [103–116], transient fluorescent up-conversion [117], pump degenerate four wave mixing [118–122] photon echo [123], 2D electronic spectroscopy [124] and time-resolved femtosecond stimulated Raman scattering [100, 101, 125–130] where used for these purpose. During those studies at least two additional "dark" states were proposed. First a state $1B_u^-$ was discovered. Footprints of this state where observed in resonance Raman scattering in 1999 [131] and in visible transient absorption [110] in all-trans-spheroidenes and it's presence was later confirmed [132, 133]. The $1B_u^-$ state was first frequently designated as S^*, but now as yet another dark state with unknown nature was discovered (see section 3.4.), this name is no longer used for $1B_u^-$ [123].

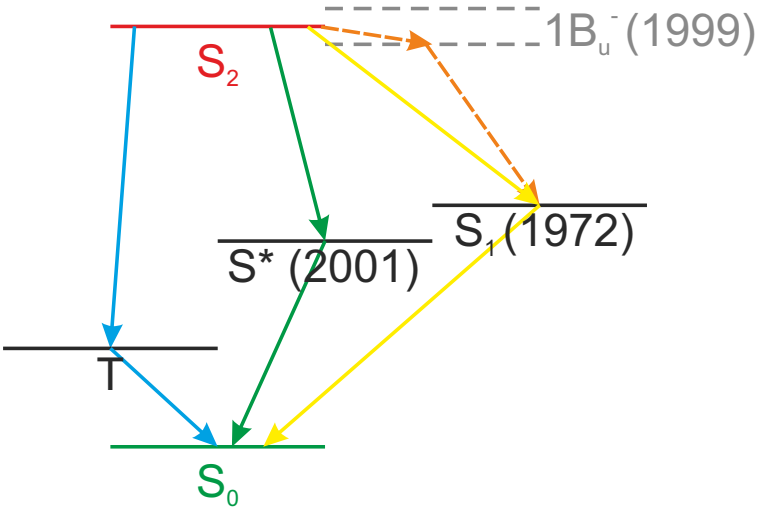

Figure 3.1: Simplified electronic levels scheme of carotenoids. The electronic levels are marked with their common names, in brackets the dates of particular level discovery are presented. The possible paths of relaxation of excitation of S_2 state towards ground S_0 state are marked with arrows. The exact possition of $1B_u^-$ state in trans-β-apo-8′-carotenal is unknown, this state lies in between the S_2, S_1 for carotenoids with conjugation length higher than 8, while for shorter molecules it is above the S_2 state. The S^* is believed to by the S_1 state with different carotenoid conformation. Significant population of the triplet (T) state is also considered in recent models.

The energy of the three states S_2, S_1 and $1B_u^-$ was found to depend on the conjugation length (the length of the molecule backbone chain) of the carotenoid molecule [100,113,123,134,135]. For carotenoids with conjugation length higher than 8 the $1B_u^-$ lies in between the S_2, S_1 while for shorter molecules $1B_u^-$ is above the S_2 state. Therefore for trans-β-apo-8′-carotenal (conjugation length 8) and β-carotene (conjugation length 9) the $1B_u^-$ state could be taking part in the $S_2 \longrightarrow S_1$ transition [107,135]. During last decade a controversy on this subject arose [123]. Spectral features that do not fit into a simple direct $S_2 \longrightarrow S_1$ internal conversion transition were presented [100,105,112,116–118,120–122,125–127,129–131,134,136–139]. Many authors tried to explain the presence of those features by $1B_u^-$ involvement in the transition [100, 125, 126, 131, 134, 136–139] but many arguments against this thesis were also proposed [105, 112, 116–118, 120–122, 127, 129, 130].

One possible scheme of $1B_u^-$ involvement is the following: while $1B_u^- \longrightarrow S_1$ transition happens on the time scale of a picosecond while the $S_2 \longrightarrow 1B_u^-$ transition is very fast (around 10 fs) [100, 125, 126, 138, 140, 141]. This concept however was deeply analyzed and criticized in favor of concept that the features should be assignment to hot (vibrationally highly excited) long living S_1 state [105, 123, 142–144]. Other possible options are that S_2 lives for about 100–200 fs, while it is the $1B_u^-$ state which lives for a very short time [123,145] and that a conical intersection rather than internal conversion happens between S_2 and S_1 [123].

In the present chapter an attempt to support the thesis that $S_2 \longrightarrow S_1$ transition in trans-β-apo-8′-carotenal molecule does not involve additional electronic level (like $1B_u^-$) will be held. The spectral features, observed by

means of the TR-FSRS setup build for this purpose by the author, are explained by involvement of multiple vibrationally excited sublevels of electronic level S_1. The thesis is supported by quantum mechanical model derived by dr hab. B. Gadomska by use of formalism of projection operators [146, 147] and solved numerically by the author. Additionally the time constants of the electronic and vibrational relaxation within the molecule are revealed and a phenomenon of transient vibrational inversion of population and it's influence on the TR-FSRS signal is discussed.

The chapter is organized as follows. First the Time-Resolved Femtosecond Stimulated Raman Scattering technique is described in section 3.1. Second the construction of the TR-FSRS setup build by the author in LENS is presented in section 3.2. Next the trans-β-apo-8$'$-carotenal molecule and the results of it's measurements are described in sections 3.4. and

3.1 Time-Resolved Femtosecond Stimulated Raman Scattering technique

The Stimulated Raman Scattering phenomenon can be used for spectroscopic goals. For example two narrowband laser beams can be tuned with their frequency difference to the frequency of the molecular normal vibration. The energy of the photons of one laser beam can than be distributed to create new photons of the second beam and simultaneously to excite the medium vibrations (see Fig. 3.2). Therefore, respectively, the loss and gain of the two beams can be measured. This technique can be used for highly accurate determination of vibrational frequencies.

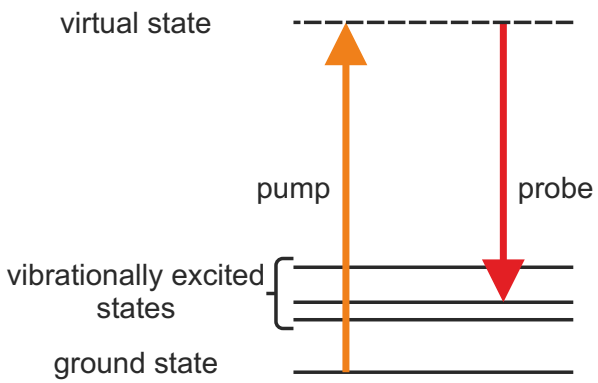

Figure 3.2: The energy diagram for stimulated Raman scattering experiment with two narrowband laser beams. The energy of photons of higher frequency pump beam (orange) is converted into the energy of created photon of the probe (red) and into the vibrational excitation of the sample. The specific vibration can be selected by tuning of the beams frequency.

The efficiency of Stimulated Raman Scattering benefits from the high intensity of laser light source. This efficiency can further be increased by use of laser pulses where the peak intensity can be significantly increased with respect to the intensity of continuous wave lasers. The highest efficiency comes when shortest, femtosecond like, pulses are used. However, in a case, when both pulses are short, the vibrational frequency can no longer be measured accurately. Moreover, the beam with broad spectrum can excite multiple vibrational levels at the same time (see Fig. 3.3). A compromise acceptable for many physical systems can be obtained by use of a few picosecond pulses. Then the resolution can be as good as 5–30 cm^{-1} and at the same time the signal is strong so measurement of Raman gain do not require photon counting techniques, instead photodiodes or CCD detectors can be used.

Further advantages of usage of the ultrashort pulses can be recognized when only pump beam is kept narrowband and a spectrally resolved detection

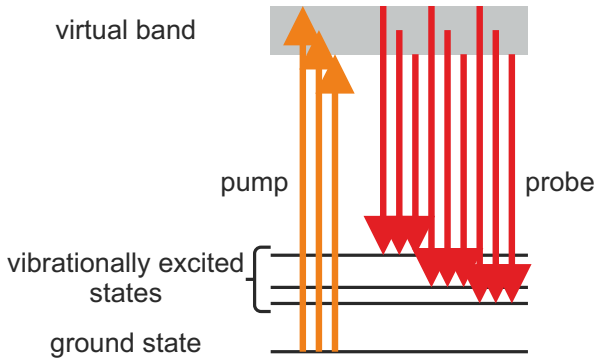

Figure 3.3: The energy diagram for stimulated Raman scattering experiment with two broadband laser beams. Multiple vibrational levels are excited.

is employed. In such a case multiple vibrational levels are excited, but the trace of this excitation forms a set of Raman lines in the probe spectrum (see Fig. 3.4 and 3.5). The width of those lines depends on the spectral width of the pump [125, 148] The main advantage of this technique is that the wide part of the Raman spectrum of the sample can be collected without the need of tuning the laser frequencies. A broad and intense Raman spectrum can, in fact, be acquired in one laser shot.

The FSRS is turned into a time resolved technique by adding the second pump pulse (actinic pump). The role of actinic pump is to excite the sample electronically. The overlapping FSRS spectra of ground and excited state are then gathered as a function of delay with respect to the excitation. The time resolution of this technique is approximately given by cross-correlation of short probe and actinic pump pulses [125,148]. Thus TR-FSRS can give both: good spectral and temporal resolution. Therefore, it was successfully implemented for studying subjects like photosynthesis [130, 149, 150], mechanisms of vision [151], photoinduced spin crossover [152] and recently, excited-state

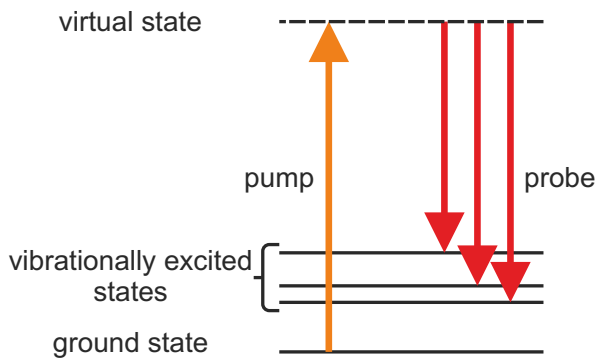

Figure 3.4: The energy diagram for stimulated Raman scattering experiment with a narrowband pump and broadband probe. Multiple vibrations of the sample are excited, but if the probe beam is spectrally resolved during measurement a set of Raman lines corresponding to the specific vibrations is obtained. The width of the lines depends on the spectral width of the pump.

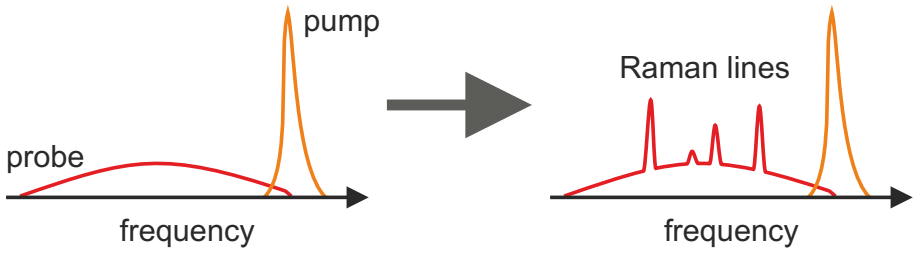

Figure 3.5: Spectra of a narrowband pump and broadband probe in the stimulated Raman scattering experiment before and after passing through the sample. Multiple vibrations of the sample are excited and multiple Raman line can be observed in the probe spectrum.

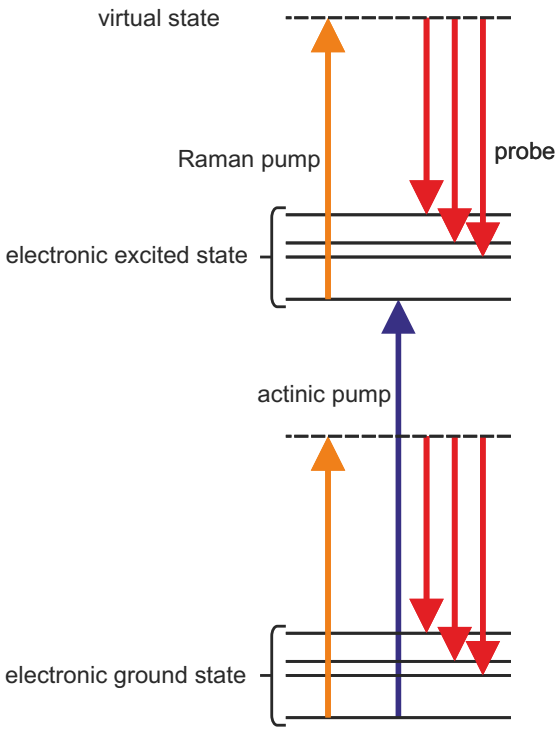

Figure 3.6: The energy diagram for Time-Resolved Femtosecond Stimulated Raman Scattering technique. First, the sample is excited to electronically excited state, then a Stimulated Raman Scattering spectra are acquired as a function of delay. The sample is never excited in 100 %, moreover the electronic state can decay in time, therefore Stimulated Raman Scattering spectra contain Raman lines of both excited and ground electronic states.

proton transfer [153]. Various samples were put under those studies, including β-carotene [125–127, 129, 130, 144], bacteriorhodopsin [150], diphenyloctatetraene [149], rhodopsin [151], iron complexes [152], pyranine [153, 154], rodamine 6G [155], poly(methyl methacrylate) [156], carotenoid phthalocyanine dyad [157], $CDCl_3$ [158, 159] and o-nitrobenzaldehyde [160].

The technique becomes popular and the two dimensional version of TR-FSRS, where information on vibrational mode coupling is retrieved, has recently been developed [158, 159, 161–163]. Special innovations were introduced for narrowband Raman pump generation [164, 165] and background free techniques, with use of interferometry [156] and Femtosecond Raman Induced Kerr Effect Spectroscopy [166], were invented. Recently also sample activation with tilted pulses, going in the perpendicular direction to the Raman pump and probe, was proposed [157]. However, no subpicosecond time resolution could be achieved in this case.

3.2 Setup

The Time Resolved Femtosecond Stimulated Raman Setup was constructed by the author in European Laboratory for Nonlinear Spectroscopy (LENS) in Florence. It has been based on femtosecond regenerative chirped pulse amplifier Legende Elite form Coherent Inc. The amplifier was seeded with femtosecond oscillator Micra from the same company.

The output pulse from the amplifier was about 45 fs long and its spectrum spanned about 30 nm around the central wavelength of 800 nm, with the

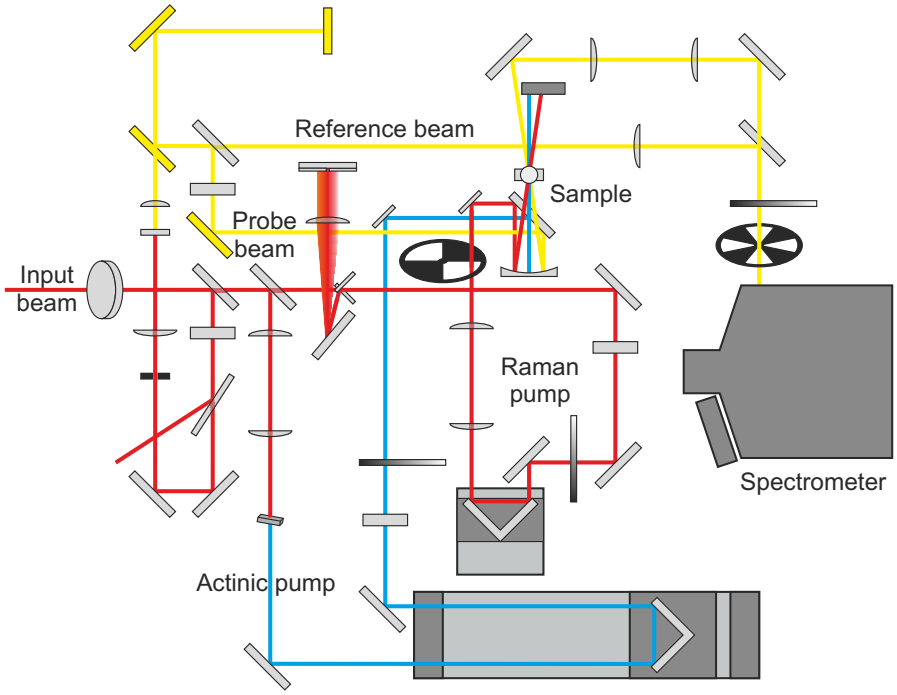

Figure 3.7: The scheme of TR-FSRS setup. The probe, reference, actinic and Raman pump beams are shown. See next figures for details on optical elements of the setup.

repetition rate of 1 kHz. The beam was split between several setups and 235 μJ was directed into TR-FSRS setup.

The scheme of the whole setup is presented on Fig. 3.7. The path of three beams required for experiment is explained in the following sections and presented in Fig. 3.8., 3.10. and 3.11. Two long exposure photographs of the setup are presented in Fig. 3.13. and 3.14.

3.2.1 Probe and reference beams

To create a broadband probe the supercontinuum generation process was used. The paths of the probe and reference beams are presented in figure

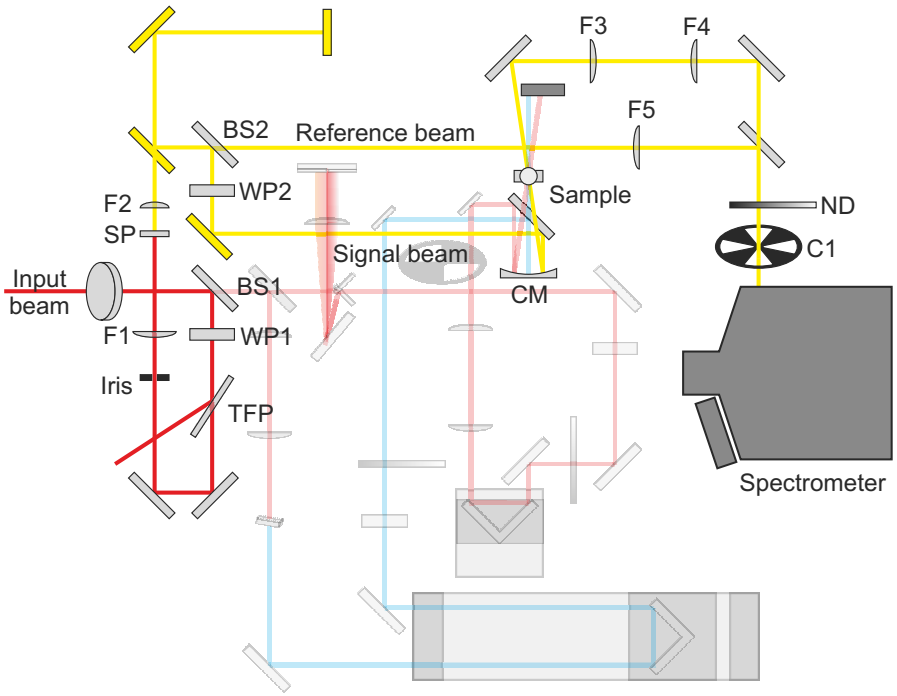

Figure 3.8: The path of probe and reference beams in TR-FSRS setup. The input beam from amplifier goes through periscope into the setup. Part of a beam is picked up with 7% beamsplitter (BS1) to form the probe and reference beam. The beam passes through half-wave plate (WP1), thin film polarizer (TFP), and the iris (Iris). It is then focused with f = +125 mm lens (F1) on a 1 mm sapphire plate (SP) where supercontinuum is generated. The supercontinuum beam is collimated with f = +20 mm lens (F2). It is reflected by a set of gold mirrors (yellow) and splited into reference and probe with a brodband beamsplitter (BS2). The reference is then focused with f = +200 mm lens (F5) on the entrance of the spectrometer. The probe polarization is controlled with half-wave plate for 800 nm (WP2) and is focused on the sample with a f = –150 mm concave mirror (CM). The probe is then collimated with f = +150 mm lens (F3) and focused on the spectrometer entrance slit with f = +200 mm lens (F4). Both, probe and reference, are attenuated by neutral density filter (ND) and chopped with a chopper (C1) before entering the spectrometer.

3.8. In the present setup to generate a probe and reference beam a part of the input beam was separated with a 7% reflecting beamsplitter. The energy of the beam in this arm was controlled with half-wave plate and a thin film polarizer. In this doublet one can control the energy of the passing beam by rotation of the half-wave plate. The beam later passed the adjustable iris and was focused with a lens (f = +125 mm) on the 1 mm sapphire plate where supercontinuum generation occured. The position of the sapphire crystal was adjustable and its initial position was optimized as follows. The iris was open and the energy of the input beam was reduced until the supercontinuum colour pattern disappeared. Then the crystal was moved to a place where colour pattern appeared again. This procedure was iterated until the crystal position corresponding to the minimum of energy, still generating supercontinuum, was found. Later the iris was adjusted and input energy was changed so that the spectrum of the supercontinuum was reaching into infrared region of interest. The generated supercontinuum beam was collimated with f = +20 mm lens. The beam was split by a broadband (620-1050 nm) 50% beamsplitter into the probe and reference beams. The reference was focused on the detector entrance with a f = +200 mm lens. The probe polarization was controlled with a 800 nm wave-plate and the beam was focused by a f = -150 mm aluminum concave mirror on the sample. After passing the sample it was collimated and later focused on the entrance of the monochromator with f = +200 mm lenses. Reference and probe were attenuated with reflective neutral density variable filter before entering the detector. Both beams were chopped to prevent illumination of detector during data digitalization.

The size of the probe beam in the sample was controlled by translation of the collimating lens and was set to 70 μm.

Initially the time compression of the supercontinuum was attempted. The compression was done with two SF10 prisms. Retrieval of supercontinuum time-frequency profile (see figure 3.9 was done by measurements of the sum frequency generation of supercontinuum beam and the fundamental beam in a thin BBO crystal. The spectrum of sum frequency was acquired with Ocean Optics spectrometer for various delays between the summed beams. The measurement was done for sum frequency wavelengths in range 400 - 444 nm which corresponds to 800 - 1000 nm of the probe ferquency. The 60 fs cross-correlation width in range from 0 to 2500 cm^{-1} was achieved. The chirp of supercontinuum was 2244 fs^2.

It was, however, concluded that the prism line compression of the supercontinuum is not required and the delay correction can be performed numerically. Moreover, the day to day amplifier's beam pointing was unstable and frequent corrections had to be performed manually. In such a case also the prism compressor would have to be reset every day. Thus, finally the compressor was removed, the correction on the probe pulse beam was done based on the cross-phase modulation and other cross effects of the probe with the actinic pulse. The length of the probe pulse was estimated be no longer than 70 fs.

3.2.2 Actinic pump

The path of the actinic pump is presented in figure 3.10. The actinic pump was created by frequency doubling of part of the fundamental beam.

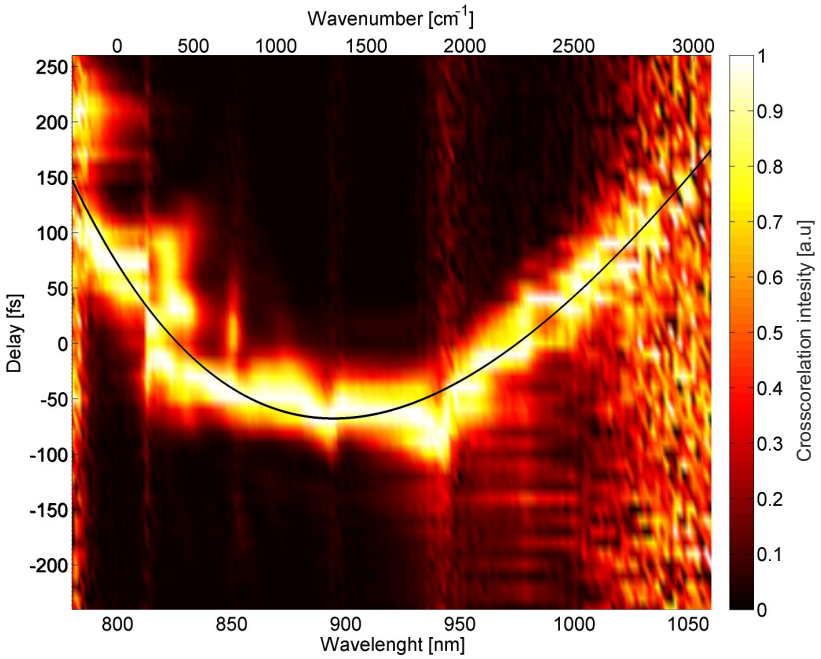

Figure 3.9: Cross-correlation of the supercontinuum and the fundamental beam together with a second order pronominal fit corresponding to the 2244 fs^2 chirp.

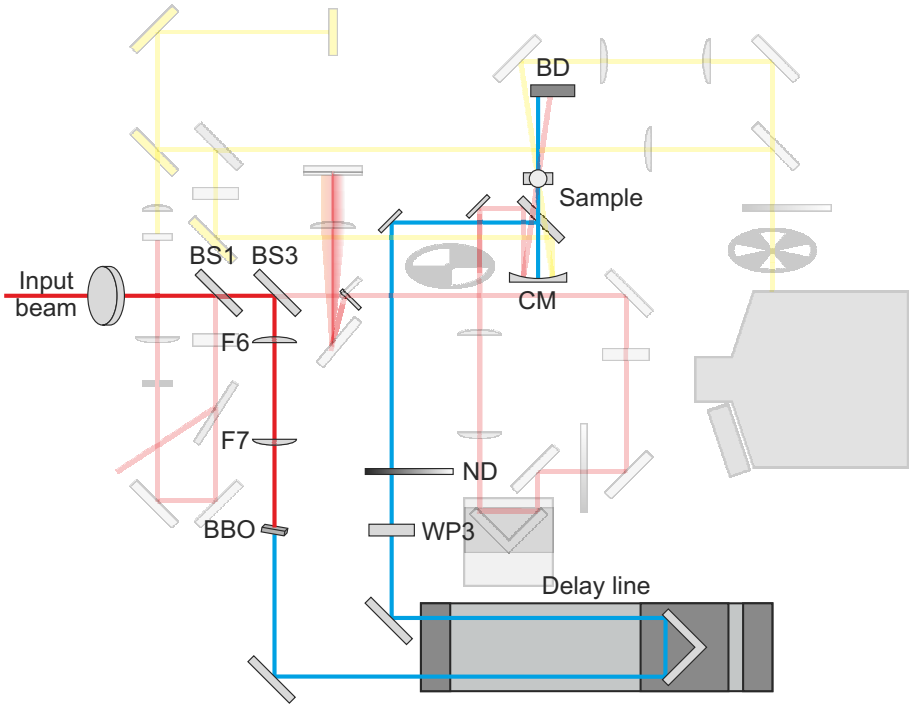

Figure 3.10: The path of the actinic pump beams in TR-FSRS setup. Part of the beam after beamsplitter (BS1) is reflected with second similar 7% beamsplitter (BS2). This beam passes a telescope of two lenses: f = + 150 mm (F6) and f = – 50 mm (F7) and is frequency doubled by BBO crystal (BBO). Net it is reflected by a dichroic mirror which reflects 400 and transmits 800 nm goes into the delay line.Then the beam goes through half-wave plate (WP3) and a neutral density filter (ND). Finally it is focused on the sample with concave mirror (CM).

About 15 μJ of the input was separated from the main 800 nm beam with a 7% reflecting beamsplitter. The separated beam passed through two lenses: f = + 150 mm and f = – 50 mm which together form a shrinking telescope with magnification of 1/3. After this the second harmonic generation in the 1 mm BBO crystal was performed. The fundamental 800 nm was filtered out from the generated second harmonic by two dichroic mirrors with high reflection at 400 nm and low reflection at 800 nm. One of the mirrors was placed after the crystal and it was reflecting the beam into the delay line. The delay line was based on a M-413.2PD 20 cm translation stage from PI (Physik Instrumente) Ltd. and the beam was back reflected by a set of two aluminum mirrors supported with parts of their front faces on the right angle optical prism. After that the delay line beam was reflected with a second dichroic mirror. Its polarization was controlled by a half wave-plate and it's energy could be attenuated with neutral variable density filter. Finally the beam was focused on the sample with the f = –150 mm concave mirror. The actinic pump beam waist in the sample was controlled with the position of the f = –50 mm lens of the telescope and was set to 70 μm. The highest beam energy, for minimal filtering, was 200 nJ. The duration of the actinic pump pulse was 70 fs. This was estimated from cross-correlation measurement with fundamental beam, both the sum and difference frequency generation in thin BBO crystal were used for this purpose.

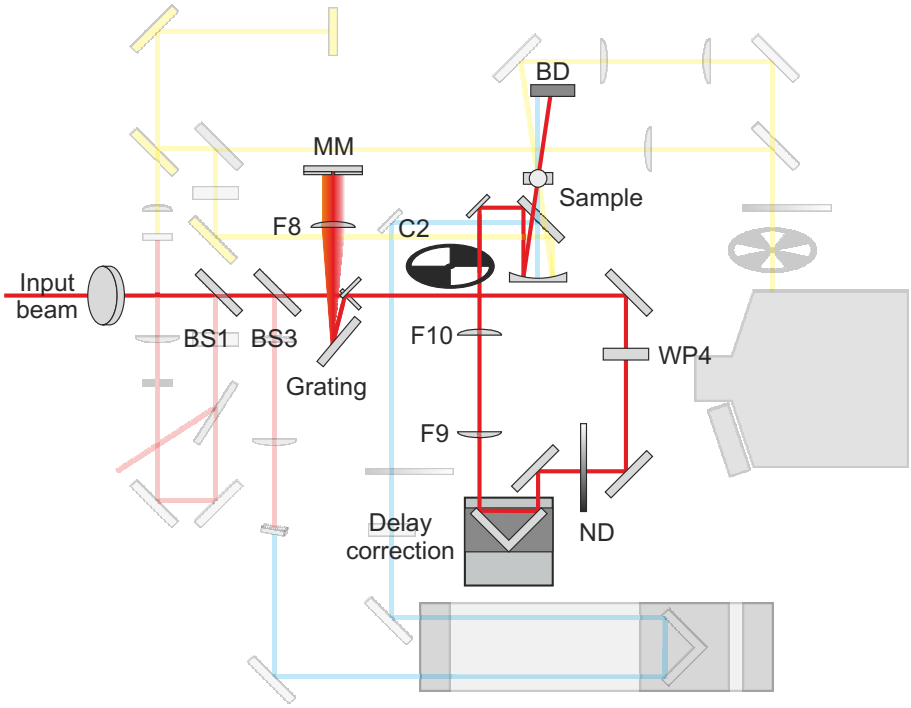

Figure 3.11: The path of the Raman pump beams in TR-FSRS setup. The input beam passing through beamsplitters BS1 and BS2 is dispersed with a grating, the dispersed colors are imaged with a cylindrical lens f = + 100 mm (F8) on the masked mirror (MM). The mask selects a narrow-band part of the beam spectrum and this part is reflected back through cylindrical lens and grating and it is sent further into the setup. The beam passes the half-wave plate (WP4) and a variable neutral density filter (ND). Next the correction of the delay between Raman pump and probe is performed (Delay correction). The beam then passes a telescope with f = +200 mm lens (F9) and f = –50 mm lens (F10). The beam is chopped with chopper (C2) and focused in the sample with concave mirror (CM).

3.2.3 Raman pump

The path of the Raman pump beam is presented in figure 3.11. Part of the input beam was passing through two 7% beamsplitters. The remaining energy (203 μJ) of the amplifier beam was used as a Raman pump.

The narrowing of the Raman pump spectrum was first done by using a narrow band filter. The filter was produced by Layertec and according to the specification it should have transmission of 1.5 nm (full width at half maximum) around 808 nm which corresponds to 25 cm^{-1} resolution. It was found, however, that their transmission was twice as broad giving 50 cm^{-1} of resolution. This resolution could not be accepted and "2f grating compressor" was build instead [167]. Thus, the beam spectral components were dispersed with a grating (1250 grooves/cm, blazing angle at 750 nm from Horiba) and imaged on the mirror with a cylindrical lens. The f = +100 mm cylindrical lens was places at focal distance from the grating and the mirror, so that the beam was forming a plane wave front on the mirror. The mirror was masked with a slit. The spectral bandwidth of the light reflected from the mirror was controlled by regulation of the slit width and the central wavelength by its translation parallel to mirror surface. The mirror in the compressor was tilted so the reflected beam was going out through the lens and on the grating below the entering beam.

The distance of lens and mirror in the compressor was initially adjusted to give a round beam pattern at the output of the compressor. Then, when the stimulated Raman spectra could have been acquired, it was slightly corrected to minimize the Raman lines width. The obtained spectral resolution was 25 cm^{-1}. Most of measurements where performed for the 798 nm Raman pump,

around the maximum of the spectrum of the amplifier. The wavelength could have been shifted by around 5 nm in both wavelength direction with an acceptable pulse intensity loss.

The polarization and the energy of the Raman pump were controlled with a half-wave plate and a reflective variable neutral density filter, respectively. Up to 3 μJ of Raman pump energy could have been used. A translation stage with a retroreflector was used for control of Raman pump – probe delay. The stage position was set once with micrometer screw to a position where maximum stimulated Raman scattering signal was observed. The beam spot size was reduced in a telescope (magnification 1/4) with f = +200 mm and f = – 50 mm lenses. The beam was chopped and focused on the sample with f = –150 mm concave mirror. The pulse duration was measured to be 760 fs. This was done by the sum frequency generation with 800 nm beam directly from the amplifier. The spot size of the beam in the sample was controlled with position of the f = –50 mm lens and was set to 70 μm.

Initially the power directed to TR-FSRS setup was 94 mW. This power was already high enough to induce cross-phase modulation between Raman pump and probe in the sample, when 50 cm^{-1} filter was used for narrowing the Raman pump spectrum. Later when filter was exchanged with 4f compressor and, thus, the Raman pump spectrum was narrowed, the incoming power was increased by a factor of 2.5 times to 235 mW.

3.2.4 Detection and data acquisition

Jobin Yvon Spex (Model HR250) 0.25 meter spectrometer with a 1250 groves/cm and a blaze angle 750 nm grating was used to resolve the spectral

components of the probe and reference beams. The spectra were acquired with two 512 pixel CCD arrays (Hamamatsu S8380-512Q). The electronic device for control of acquisition and temporary stoage of the data was prepared by Prof. Marco Prevederli in Bolognia University. After every acquisition of the spectrum the charge was transferred from CCD to analog-digital converter. The conversion and storing of the data in the device internal memory was taking 8.2 ms, in this time the monochromator entrance had to be closed. With monochromator set to 798 nm (at Raman central wavelength) one laser shot was enough to saturate the detector. It was found however that in the most interesting region at 950 nm ($\sim$ 1500 cm^{-1} away from Raman pump central wavelength) the charge accumulated from 100 laser shots was not enough to saturate the CCD. Both the decrease of probe intensity and detector sensitivity towards infrared were the cause of this. Thus to create most flexible measurement conditions a special set of choppers was developed in the LENS machine and electronic shops. The required choppers angular velocity was both too high for shutters and too small for available standard choppers thus steeping motors were used in this construction. First chopper (C1 on Fig. 3.8.) was placed in front of the monochromator. It was constructed in such a way that after every 40 laser shots (40 ms) illuminating the detector the entrance to monochromator was closed for 10 ms (10 laser shots) – in this time the conversion and data storing was performed. The second chopper (C2 on Fig. 3.11.) was closing the Raman pump for every second spectrum acquisition (for 50 ms every 100 ms).

When the low frequency region of the spectrum was observed, variable neutral density filters were used to prevent detector saturation. If the high

frequency region was observed the filters were removed and optionally the choppers driving frequency was divided by two or four to extend the time of detector illumination and increase the signal.

The scheme of electronic device connections is presented in Fig. 3.12. The 1 kHz laser pulse signal triggers the choppers controller. Next, the controller was triggering the choppers with 1 kHz, 500 or 250 Hz signals (if chosen) synchronized to the laser output, this corresponds to accumulation of 40, 80 and 160 pulses, respectively. Choppers were equipped with optical switch so the information on the beam state (open or closed) could be retrieved. The optical switch signal from each chopper was send back to the controller and a TTL open/closed signal was further send on the computer's parallel port (LPT). The optical switch signal from probe chopper was used for triggering the detector data digitization. The computer was controlling the detector state via USB interface. In particular, the index of currently acquired spectrum was saved together with information on state of Raman pump chopper (open/closed). At most, 64 spectra pairs (signal and reference, 32 with and 32 without Raman pump on) were stored in the device, after this the transfer of data to the computer was required. The transfer took about 200 ms for all 64 spectra pairs. Multiple delay scans were performed for a single sample. The number of spectra acquired for every delay in a single scan was specified by the user.

The control software was written by the author in National Instruments LABView, the lower level interfaces for detector and choppers state monitor were written in C++. An interface for delay line control was developed in LABView.

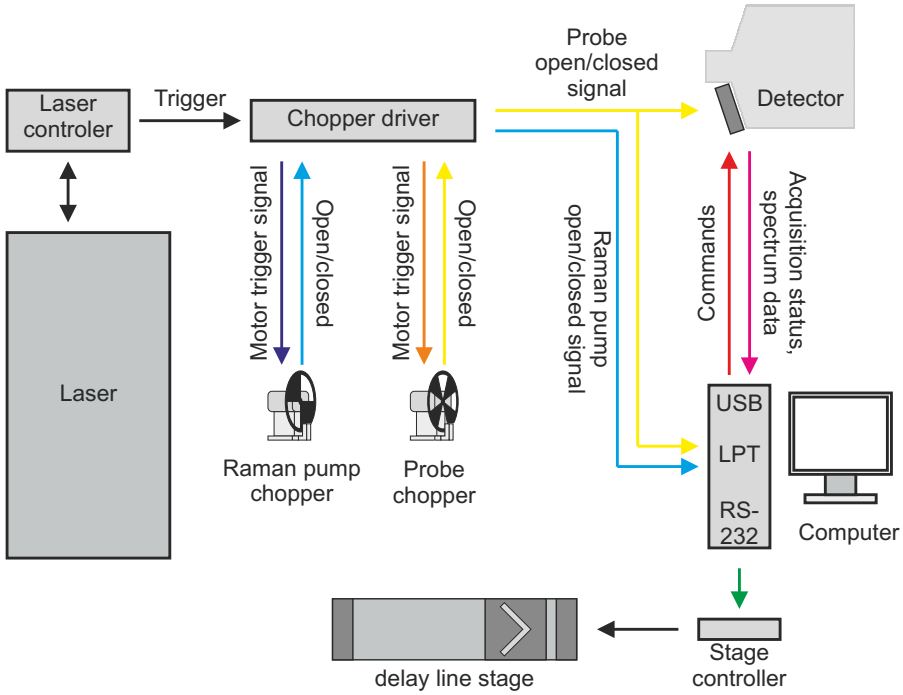

Figure 3.12: Scheme of electronic devices connections. The laser pulse signal from the amplifier triggers the chopper controller. The synchronized signal from the controller moves the choppers steeping motors. The TTL open/closed signal goes back to the controller and is sent to the computer via LPT interface. The open/close signal of the probe beam chopper triggers the detector. The status of the acquisition and the number of acquired spectra is sent on command to the computer via USB interface. After acquisition of up to 64 probe and reference spectra computer commands data transfer from the detector. The two way communication with the delay stage controller is done via RS-232 interface.

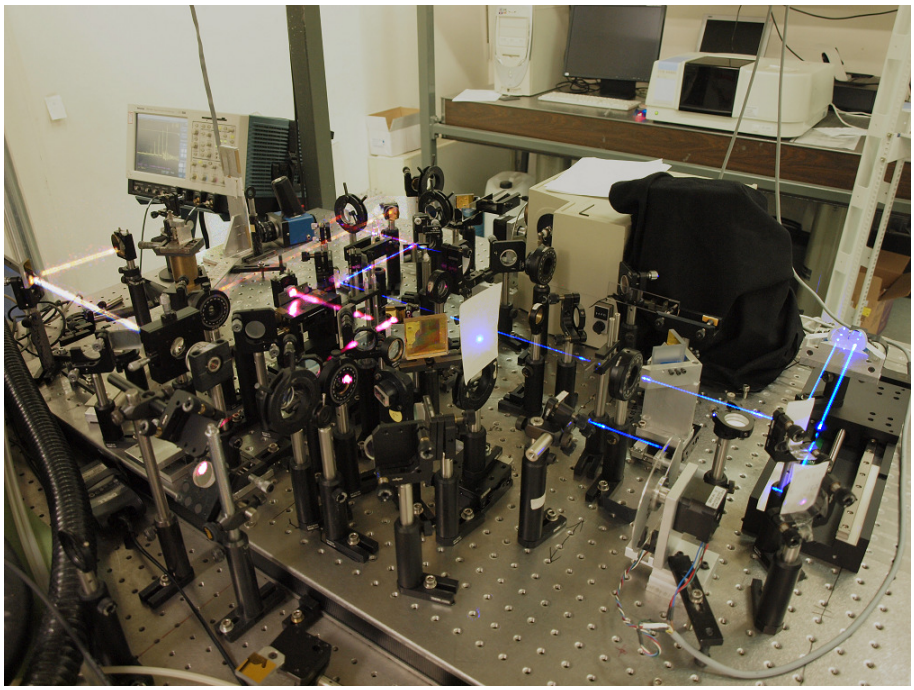

Figure 3.13: Long exposure photo of the TR-FSRS setup in LENS. All the beams are visible: actinic pump – blue, Raman pump – violet, probe – yellow.

3.3 Data analysis

In the absence of transient absorption and emission following consideration on the SRS signal can be performed. If the supercontinuum beam is divided into a probe and reference beam by a beamsplitter with wavelength dependent transmission $T(\lambda)$, the intensity of the i'th probe pulse passing the sample (according to Lambert-Bear's law) in absence of Raman pump is:

$$I_{Sig,i}^{pump\ off}(\lambda) = T(\lambda)I_i(\lambda)e^{-\alpha(\lambda)\Delta z},$$

where $I_i(\lambda)$ is the wavelength dependent intensity of supercontinuum for the i'th laser shot, Δz is the sample length and $\alpha(\lambda)$ represents combined losses

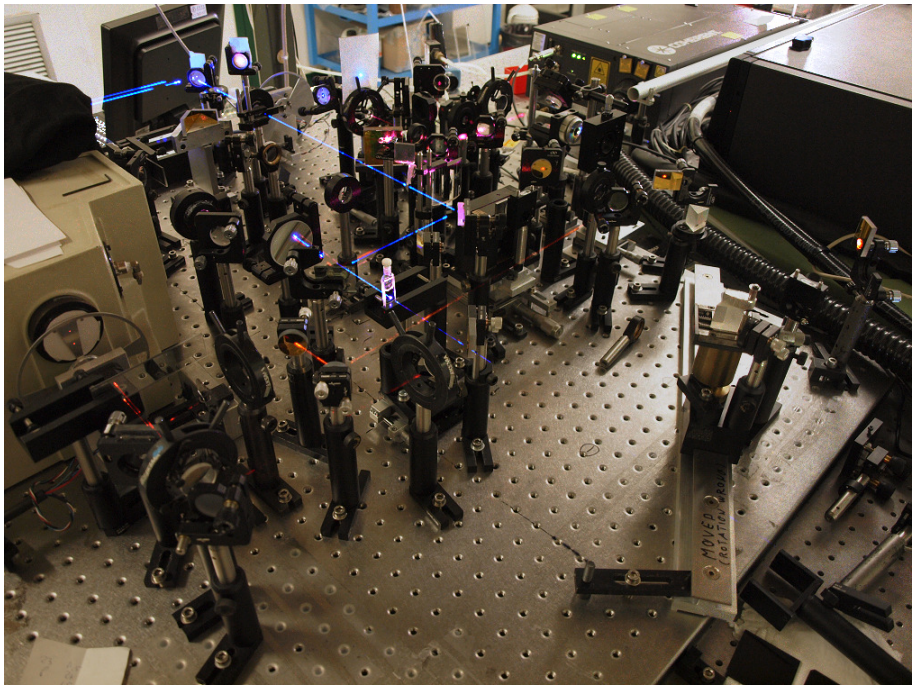

Figure 3.14: Long exposure photo of the TR-FSRS setup in LENS. The cuvete with the sample and the entrance to the monochromator are visible.

due to absorption and scattering. When Raman pump is present the intensity becomes:

$$I_{Sig,i}^{pump\ on}(\lambda) = T(\lambda)I_i(\lambda)e^{(g(\lambda)-\alpha(\lambda))\Delta z},$$

where $g(\lambda)$ is the Stimulated Raman gain. The reference beam is Raman pump independent, therefore:

$$I_{Ref,i}^{pump\ off}(\lambda) = I_{Ref,i}^{pump\ on}(\lambda) = (1 - T(\lambda))I_i(\lambda),$$

where $I_{Ref,i}^{pump\ off}(\lambda)$ and $I_{Ref,i}^{pump\ on}(\lambda)$ are intensities of reference beam in absence and presence of Raman pump, respectively. In the present experiment all the above spectra are acquired. Pairs $I_{Sig,i}^{pump\ off}(\lambda)$ and $I_{Ref,i}^{pump\ off}(\lambda)$ are gathered

by two CCD lines for the same laser shot, when chopper blocks the Raman pump beam and $I_{Sig,j}^{pump\ on}(\lambda)$ and $I_{Ref,j}^{pump\ on}(\lambda)$ are gathered for another laser shot, when the way for Raman pump beam is open. Thus, the dependance of the signal on the fluctuating supercontinuum intensity can be easily removed by taking ratios:

$$\frac{I_{Sig,i}^{pump\ off}(\lambda)}{I_{Ref,i}^{pump\ off}(\lambda)} = \frac{T(\lambda)}{1-T(\lambda)} e^{-\alpha(\lambda)\Delta z}$$

and

$$\frac{I_{Sig,j}^{pump\ on}(\lambda)}{I_{Ref,j}^{pump\ on}(\lambda)} = \frac{T(\lambda)}{1-T(\lambda)} e^{(g(\lambda)-\alpha(\lambda))\Delta z}.$$

Finally the stimulated Raman gain can be calculated [127, 129, 130, 144, 149, 154, 161]:

$$g(\lambda) = \frac{1}{\Delta z} \log \left(\frac{I_{Sig,j}^{pump\ on}(\lambda)}{I_{Ref,j}^{pump\ on}(\lambda)} \Bigg/ \frac{I_{Sig,i}^{pump\ off}(\lambda)}{I_{Ref,i}^{pump\ off}(\lambda)} \right),$$

In case of the time-resolved measurements the change of Raman gain as a function of delay is interesting. Therefore first a stimulated Raman gain spectrum in absence of actinic pump was acquired ($g^{actinic\ off}$). Later the time resolved signal was obtained by subtraction of this spectrum from the delay dependent spectra $g(\lambda, \tau)$:

$$S(\lambda, \tau) = g(\lambda, \tau) - g^{actinic\ off}(\lambda), \tag{3.1}$$

giving a delay dependent change of Raman gain.

In the case, when the transient fluorescence [127, 129, 149] or absorption [129, 130, 144] is present aparto of the Raman lines, the spectrum obtained with equation 3.1 is superimposed on the broad background. This background is usually removed by subtraction of a spline fit [127,129,130,144,149].

In the present work both excited state absorption and emission background were removed by subtraction of a polynomial fit to the experimental points around the Raman bands. Recently, successful alternative ways of the background subtraction with use of optical interference effects were proposed [156].

In the past works on TR-FSRS [127, 129, 130, 144, 149, 151], after background subtraction a complicated procedure of normalization of data was in common use. The idea was to concentrate on the excited state Raman spectrum by subtraction of a normalized ground state spectrum. A recently more popular alternative is to present the data without this normalization [128, 154, 156, 157], in such a case bleaching of the ground state is explicitly visible in the delay dependent spectra. In author's opinion the latter straightforward approach gives results which are easier to interpret, thus this approach is used in the present dissertation.

3.3.1 Setup calibration

The calibration of the setup is done after acquisition of the spectrum of a known solvent. For example in Figure 3.15. a Femtosecond Stimulated Raman Scattering spectrum of benzene as a function of the CCD pixle index is presented. Three Raman lines are required for calibration. Figure 3.16. presents a measured spectrum of toluene, here the setup is already calibrated and the spectrum is plotted as a function of the frequency. Below the frequency of 750 cm^{-1} artifacts due to fast fluctuation of the supercontinuum spectrum in this spectral region are present. In Figure 3.17. a single line of

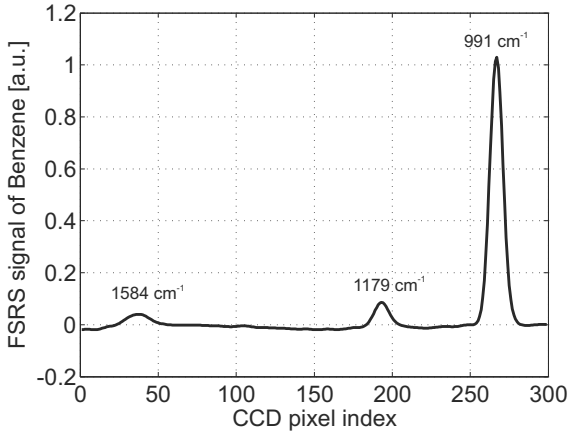

Figure 3.15: A FSRS spectrum of benzene used for setup calibration. Characteristic Raman lines of benzene are assigned to frequencies of 1584, 1179 and 991 cm^{-1}.

trans-β-apo-8′-carotenal at 1528 cm^{-1} and several lines of the cyclohexane are visible in the spectral range of interest.

3.4 Trans-β-apo-8′-carotenal molecule

The sketch of the trans-β-apo-8′-carotenal molecule together with β-carotene is presented in Figure 3.18. The symmetry characteristic to β-carotene is broken in trans-β-apo-8′-carotenal and therefore a higher infrared absorption signal is expected from the latter one while strong Raman signal is expected from the first one. Still the two molecules are close analogs and share many features, therefore, the results obtained from measurements in them can be compared [96–98].

Carotenoid molecules due to their similarity in the backbone carbonic chain with polyenes [168] are assumed to posses pseudo-C_{2h} symmetry.

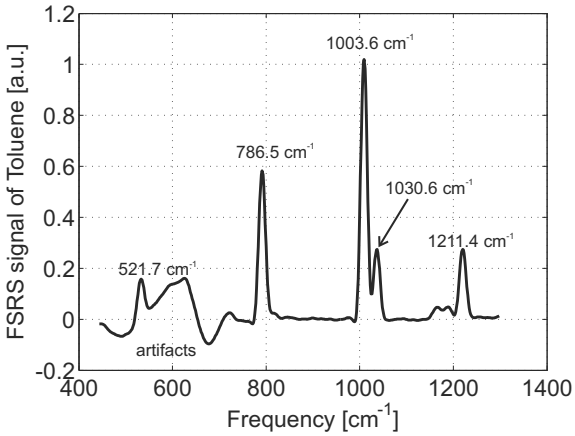

Figure 3.16: A FSRS spectrum of toluene used for calibration checking. A part of characteristic Raman lines of toluene a spectral range where artifacts appear is presented.

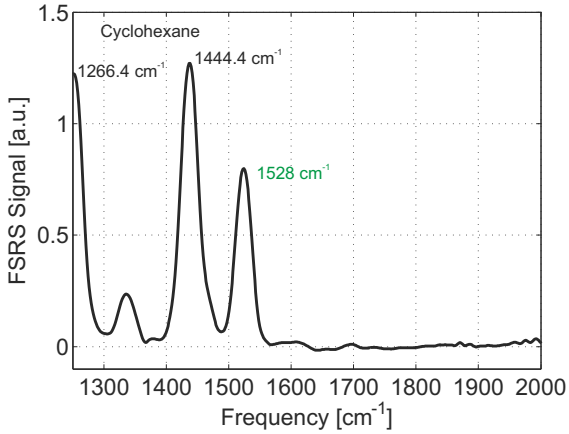

Figure 3.17: A FSRS spectrum of trans-β-apo-8′-carotenal in cyclohexane. The spectral range presented corresponds to the range where the time-resolved spectral features are expected to appear.

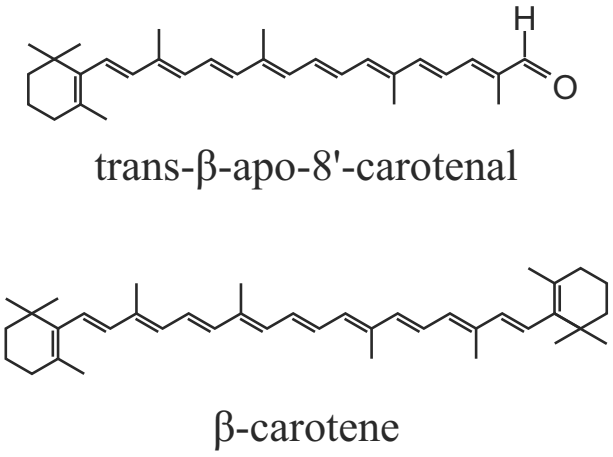

Figure 3.18: Structure of trans-β-apo-8$'$-carotenal and β-carotene.

Therefore, two low-lying excited states are expected. These are an electronic state S_1, with the same symmetry A_g^- as the ground state S_0, and a second electronic state S_2 with B_u^+ symmetry. The scheme of the electronic levels together with permitted transitions is presented in figure 3.19. The direct $S_0 \longrightarrow S_1$ transition is strongly forbidden due to symmetry, whereas a two 1275 nm photon transition is possible, this transition is, however, not a transition to the bottom of the S_1 level [96–98, 169]. On the other hand, highly energetic $S_0 \longrightarrow S_2$ transition is allowed and is responsible for the characteristic absorption band of carotenoids molecules (480–520 nm).

After excitation the S_2 state decays fast (within 0.1 – 0.3 ps) to S_1 [123, 129, 130]. This fast decay is attributed to internal conversion – transition between two different states (from S_2 to S_1 in this case) of the same spin multiplicity [170]. This transition is "horizontal": occurs from low lying vibrational levels of the higher state into high vibrationally excited levels of

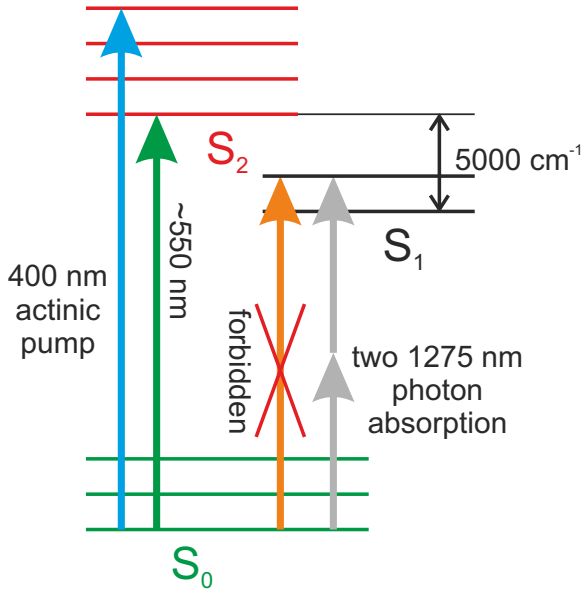

Figure 3.19: The scheme of the electronic levels together with permitted transitions. While a direct transition to S_1 from the S_0 is forbidden a two photon transition is possible. The state S_2 can be populated with green and blue light.

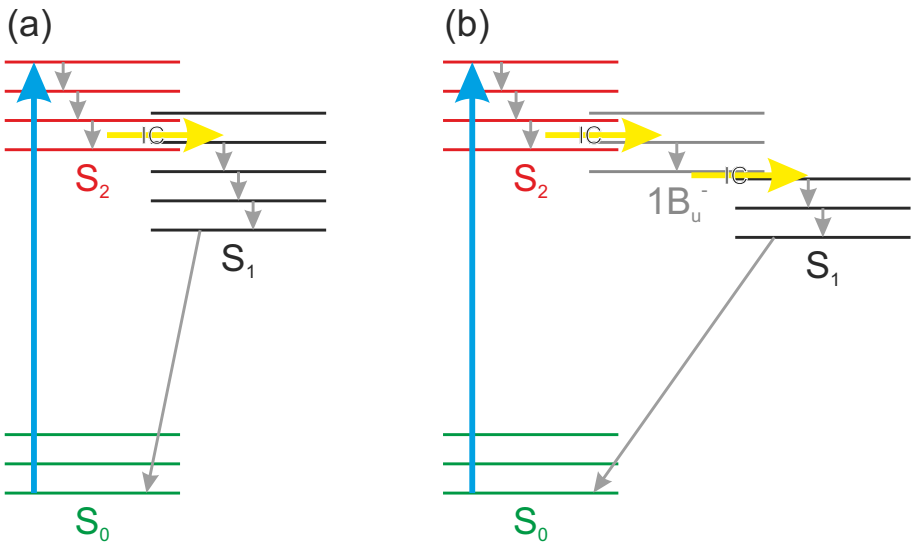

Figure 3.20: Two possible electronic schemes of the trans-β-apo-8′-carotenal with (right) and (without) a dark S* level. After excitation (Blue arrow) the molecule undergoes intramolecular vibronic relaxation (gray arrows) and internal conversion (yellow arrows).

the lower electronic state, so that the energy is conserved. As an alternative a conical intersection between S_2 and S_1 was also proposed [97, 123].

An alternative scheme of electronic levels can be considered (see Figure 3.20.). Additional dark state with a B_u^- symmetry exists in carotenoids [131], it's energy depends on the length of the carbon chains – for long chain molecules like trans-β-apo-8′-carotenal it becomes lower than that of S_2 state [123]. For the case, when additional level is considered, the transition $S_2 \longrightarrow S_1$ is expected to occur by first internal conversion from S_2 to the dark state and then another internal conversion to the S_1 state.

The strongest vibrational modes in trans-β-apo-8′-carotenal come from vibrations in the carbon chain. These are the vibrations of single (C-C) and double (C=C) bonds between carbons. In the present study the relax-

ation of the electronic and vibrational levels is investigated by observation of the evolution of Raman line attributed to the symmetric C=C stretching. Thanks to strong vibronic coupling the frequency of this vibration differs significantly in S_0, S_1 and S_2 states. This is an advantage as the three lines can be easily distinguished. The presence of S_2 and S_1 levels displacement favors fast internal conversion, due to the increased overlap of the vibrational wave-functions of two levels [170] Additionally the symmetric C=C stretching was proposed as "promoting mode" [170] of the $S_2 \longrightarrow S_1$ transition β-carotene [127], therefore a strong signal is expected.

The life time of S_1 state in carbonyl carotenoids, like the trans-β-apo-8′-carotenal, depends on the polarity of the solvent. In polar solvent this time is short. This is attributed to intramolecular charge-transfer within the S_1 state [90, 99, 102, 103, 107–109, 111, 114, 171, 172]. In the present study, however, this aspect will not be further discussed as carotenal behavior in a nonpolar solvent (cyclohexane) is studied.

Recently another dark state, currently designated as S^* was discovered [123]. This new state most likely is in fact the S_1 state in a different carotenoid conformation - a twisted backbone chain [105, 106, 123, 124]. Finally, possibility of transition to yet another triplet state of the carotenoid molecule from S_2 was recently pointed [106]. Those additional states were also not investigated in the present dissertation.

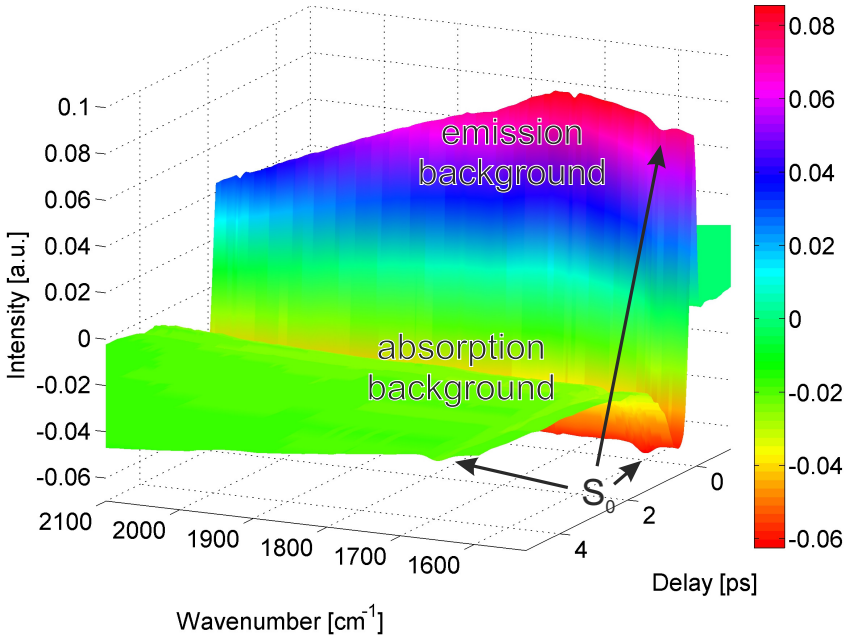

Figure 3.21: The time-resolved stimulated Raman scattering spectra before background subtraction. Transient emission and absorption regions are presented. Bleaching of the ground state Raman line is visible and designated by S_0.

3.4.1 Experimental results

The time-resolved stimulated Raman scattering spectra before background subtraction are presented in figure 3.21. Both emission, for short delays, and absorption, for longer delays, are visible. This result is similar to one obtained in β-carotene [127, 129, 130, 144, 149]. The background is removed by a 3rd and 4th order polynomial subtraction. Example spectra with polynomial subtraction are presented in figure 3.22. and 3.23, and a set of polynomials for a range of delays is presented in figure 3.24. The time-resolved stimulated Raman scattering spectra of trans-β-apo-8′-carotenal within first 5 ps after subtraction of the background are presented

in figure 3.25. Apart from the Raman bands, some artifacts connected to the detector electronics and characteristic fringes of cross-phase modulation between the supercontinuum and the actinic pump pulses are designated.

Stimulated Raman scattering spectra of trans-β-apo-8′-carotenal at various time delays are presented in figure 3.26. There are three visible lines, at 1528, around 1660 and close to 1775 cm^{-1}. At 1528 cm^{-1} a C=C stretching line from the S_0 state is present [173]. Noguchi et al. in their previous resonance Raman experiment [174] attributed lines at 1528 cm^{-1} and 1775 cm^{-1} to C=C symmetric stretching in S_0 and S_1 electronic states, respectively. Similar assignment of line frequencies in β-carotene molecule was done by Kukura et al. [130]. Additionally the line corresponding to S_2 electronic state was assigned value close to 1650 cm^{-1} in their work. Thus, based on the similarity of the molecules it is concluded that the line at 1660 cm^{-1} in figure 3.26 corresponds to C=C symmetric stretching in S_2 electronic state.

The line at 1528 cm^{-1} is present in the ground state FSRS spectrum. Therefore, the negative change of the Raman gain at 1528 cm^{-1} in Figure 3.26. corresponds to the reduction of Raman gain at this frequency. This is bleaching of the ground state due to partial excitation of the sample [128]. It's decay follows the kinetics of recovery of the ground state.

Excitation with 400 nm actinic pump populates vibrationally excited levels of S_2 electronic level of the trans-β-apo-8′-carotenal molecule. The positive feature around 1660 cm^{-1}, corresponds to the C=C stretching in the S_2 state. This band is visible within the first 200 fs and disappears as the population of S_2 state decays. Both, homogenous broadening due to short life time of the state and inhomogeneous broadening due to interaction with

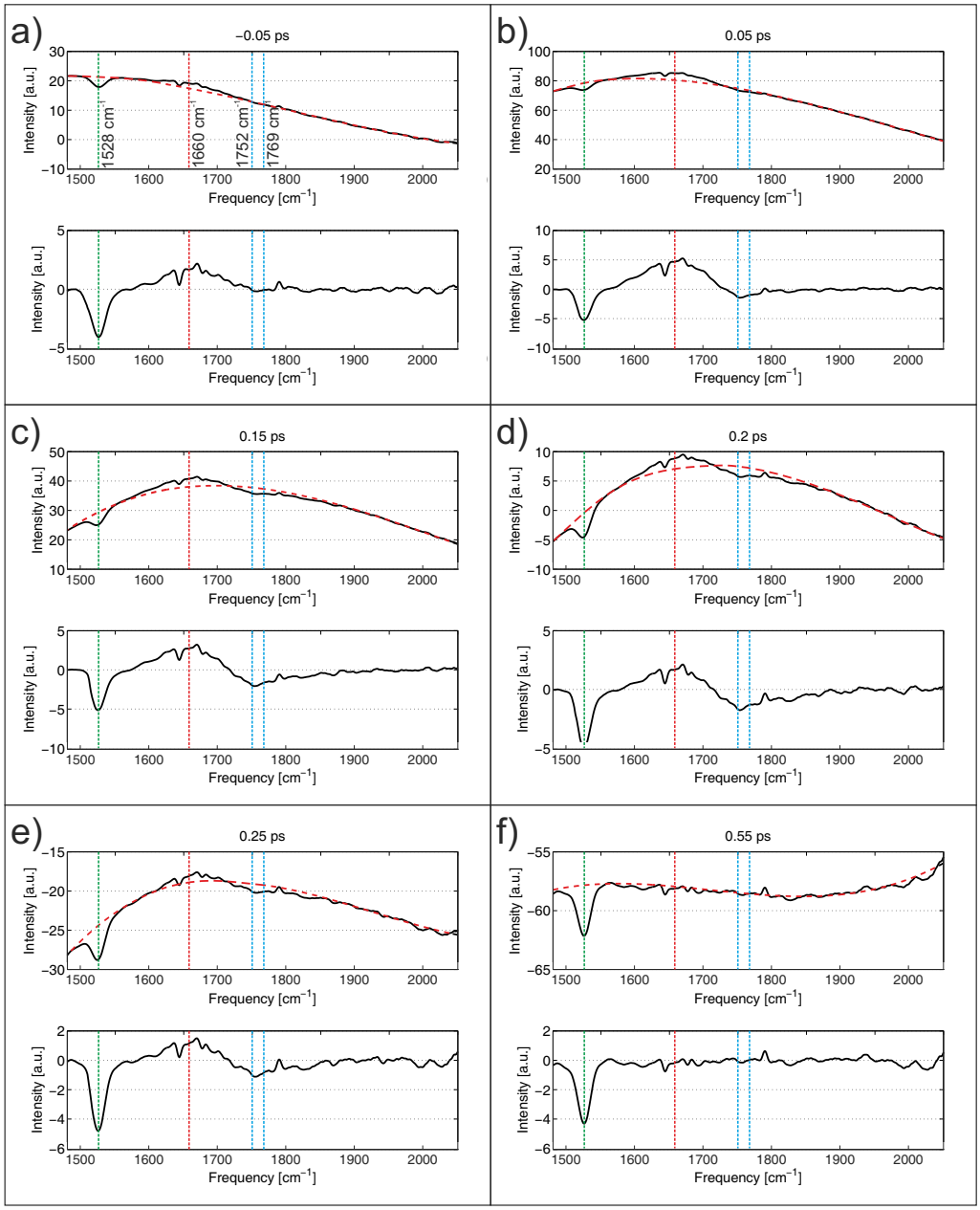

Figure 3.22: Examples of TR-FSRS raw spectra and baseline removal for selection of delays: -0.05 ps (a), 0.05 ps (b), 0.15 ps (c), 0.2 ps (d), 0.25 ps (e), 0.55 ps (f). For each delay the raw spectrum (black solid curve) and a polynomial baseline fit (red dashed curve) are presented on the top plot, and the spectrum after baseline subtraction is presented on the bottom plot. The negative signal close to 1775 cm-1 is observed in figures b-e and zero crossing can be seen in figure f.

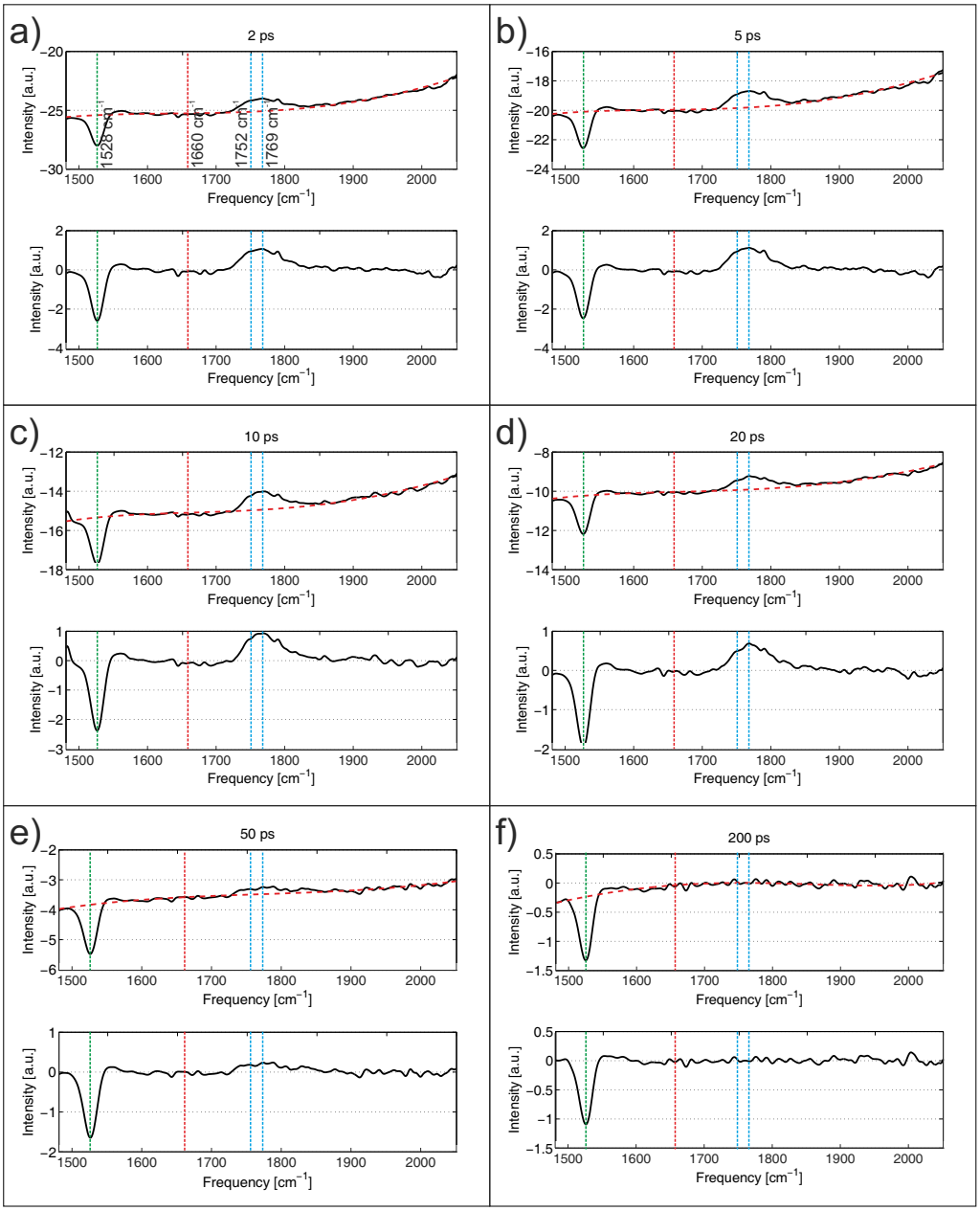

Figure 3.23: Examples of TR-FSRS raw spectra and baseline removal for selection of delays: -0.05 ps (a), 0.05 ps (b), 0.15 ps (c), 0.2 ps (d), 0.25 ps (e), 0.55 ps (f). For each delay the raw spectrum (black solid curve) and a polynomial baseline fit (red dashed curve) are presented on the top plot, and the spectrum after baseline subtraction is presented on the bottom plot. The decaying positive signal close to 1775 cm-1 is observed in figures a-e.

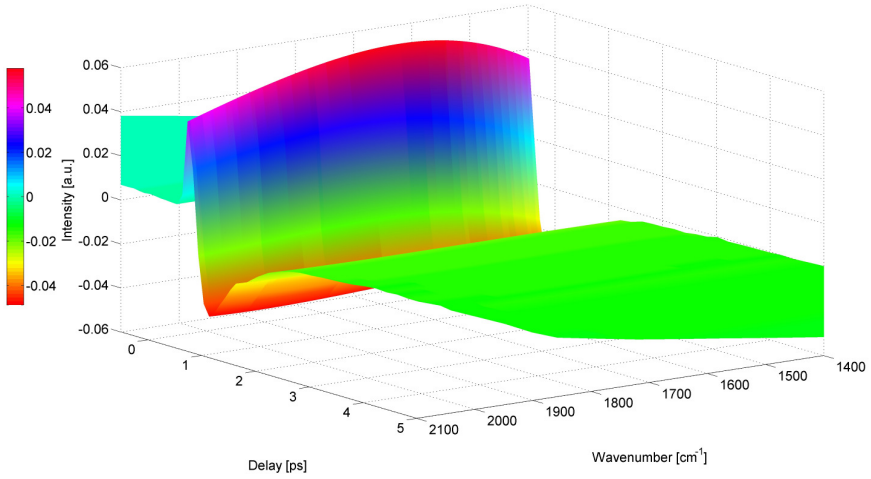

Figure 3.24: Set of background fit polynomials for a range of delays.

the solvent, causes extreme broadening of the line. It's width is close to 80 cm^{-1}. Similar broad bands corresponding to short living states were previously reported in β-carotene [130]. The spectrum of the actinic pump is not very broad, still several vibrational levels of S_2 are simultaneously excited, additionally the highly energetic 400 nm pump populates vibrationally excited levels of S_2. Therefore the questions arises as to whether the decay towards S_1 state occurs from the bottom of the S_2 electronic state after previous intramolecular vibrational relaxation in S_2, or rather internal conversion happens directly from vibrationally excited states of S_2. This second process is in principal possible, its probability should however be smaller than probability of the first one [170]. The first process, on the other hand, seems to be too slow to occur within the experimentally obtained 100-200 fs. Similar doubts on the S_2 decay process arise from the analysis of the infrared absorption measurements performed on the same molecule in LENS [175].

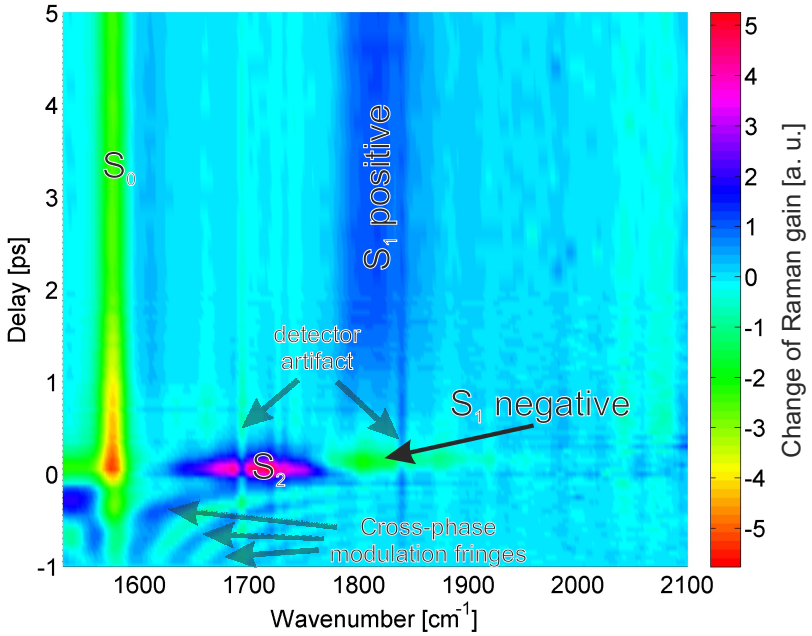

Figure 3.25: The time-resolved stimulated Raman scattering spectra of trans-β-apo-8′-carotenal. Raman bands corresponding to C=C symmetric stretching in S_0, S_2 and S_1 electronic states are designated along with artifacts connected to the detector electronics and characteristic fringes of cross-phase modulation between the supercontinuum and the actinic pump pulses.

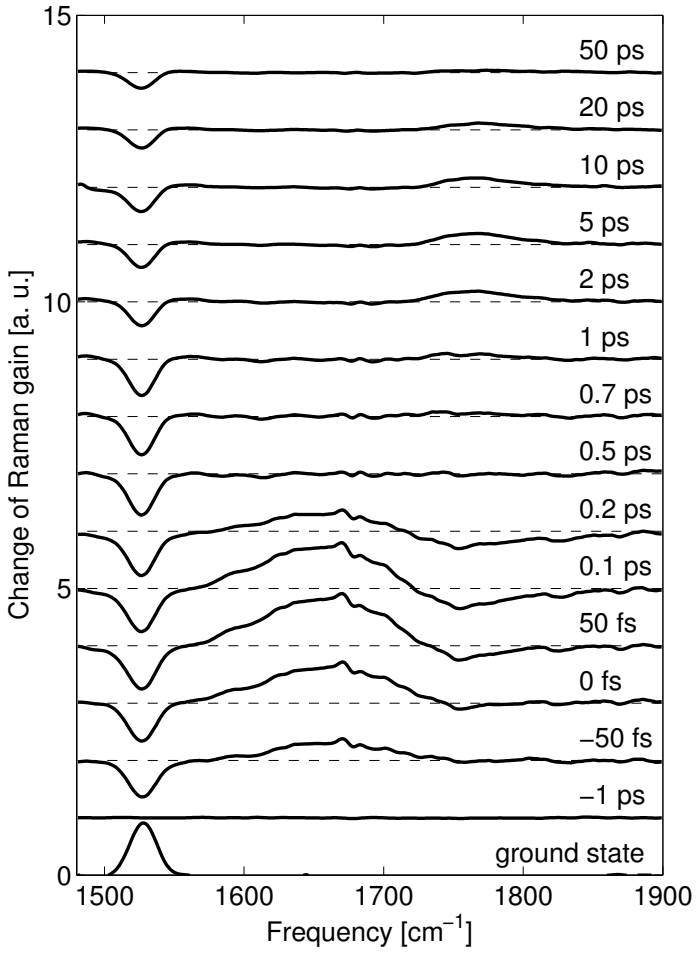

Figure 3.26: Stimulated Raman scattering spectra of trans-β-apo-8′-carotenal in cyclohexane at various delays after and before (negative delays) actinic excitation. The differential Raman gain (obtained by subtracting the SRS spectrum without the actinic excitation) is shown for all spectra, except for the bottom one, where the Raman gain of the ground state is presented. The negative signal at 1528 cm^{-1} corresponds to the bleaching of S_0 ground state. At positive delays the lines corresponding to C=C symmetric stretching in the S_2 and S_1 excited state appear at 1650 cm^{-1} and 1775 cm^{-1}, respectively. The S_1 line is negative for delays between 0 and 0.5 ps, later it becomes positive and slowly decays. It's frequency slightly upshifts as the delay time increases with respect to the actinic pulse.

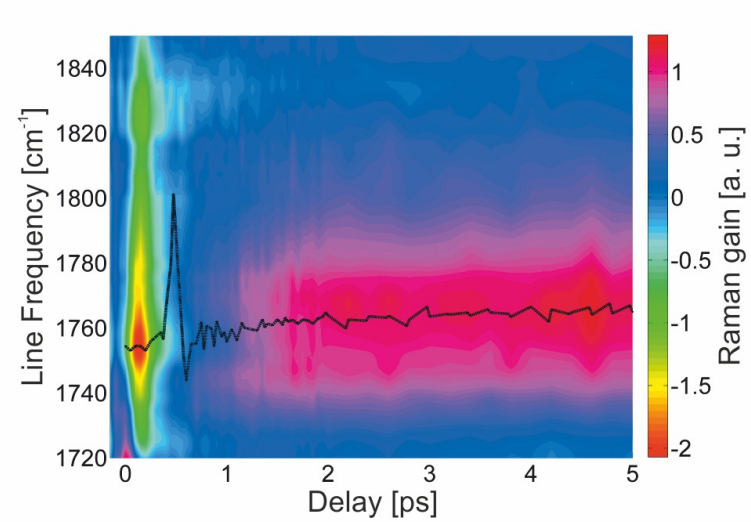

Figure 3.27: The evolution of the stimulated Raman line corresponding to the symmetrical C=C stretching in S_1 electronic state. The black curve presents the central frequency of the peak as obtained from a Gaussian fitting of the line profile. The frequency goes through singularity at 0.5 ps, where the intensity of Raman line is zero and, therefore, its frequency is undefined.

The most complicated dynamics is observed in the behavior of the line at 1775 cm^{-1}. This line corresponds to the C=C symmetric stretching in S_1 electronic state. During the first 0.5 ps a negative Raman band is observed. There is no ground state Raman band at this frequency, thus the negative signal has to be attributed to Raman losses in excited state rather than bleaching of existing ground state band. At longer time delays the signal passes through zero and becomes positive – Raman losses turn into Raman gain. Finally, it decays according to the S_1 bleaching dynamics with around 25 ps lifetime [90]. A blue-shift of the peak is observed, the evolution of the frequency, obtained by fitting Gaussian function to consecutive spectra, is presented in figure 3.27. The central frequency of the line shifts towards high frequencies with delay. This shift is interrupted by a singularity-like behavior around delay of 0.5 ps. As the Raman gain at this delay is close to zero, the frequency of the line becomes undefined. The blue-shift of the peak can be attributed to vibrational cooling in an anharmonic potential [127].

The change of the sign of observed stimulated Raman signal at a given delay with respect to the actinic pump suggests that transient vibrational inversion of population takes place in the S_1 state. The time dependent frequency blue shift may be attributed to transitions taking place between the vibrational sublevels of an anharmonic potential, for which the energy gap between subsequent levels decreases with increasing vibrational quantum number. If so, at least three vibrational levels, and thus two differences, are required for the frequency shifting to occur. The shift towards high frequencies is expected for a potential well with negative anharmonicity (like for example a Morse potential) [176]. This behavior is expected [112,127,130]

and proves that the dynamics of Raman lines provides new information with respect to informations gathered with transient absorption.

TR-FSRS measurements were performed for several wavelengths of the Raman pump within 10 nm range around 800 nm. For the case of S_1 this wavelength should be out of resonance with both higher lying states S_n (with excited state absorption of 500 – 600 nm) and the state S_2 (with 1000 – 1800 nm) [107, 117, 123]. No dependence of the signal on the Raman pump frequency was observed. In case of resonance Raman scattering, both the intensity and the line shape could change along with the Raman pump frequency [150, 177, 178]. The shape of our S_1 Raman line is well described by a Gaussian function at all delays and no dispersive shape (characteristic for Resonance Raman) is observed.

3.5 Quantum mechanical theory of coupling of light with molecular vibrations

Further interpretation of the experimental results requires formulation of a model for the molecule behavior. The goal is to confirm the thesis of the presence pf the transient vibrational inversion of population presence and to recover the life times of consecutive levels involved in the $S_2 \longrightarrow S_1$ transition, with the assumption that the state $1B_u^-$ does not take part in the transition.

The process of time-resolved stimulated Raman scattering has been previously modeled with a variety of approaches [74, 100, 125–127, 150, 177–180] but, as to the author's knowledge, none of them consider explicitly the possibility of transient vibrational population inversion. In the theories of coherent Raman scattering [147, 181], the populations of excited vibrational states are taken into account, but they are assumed to be negligible in comparison with the population of the vibrational ground state, which may not be the truth in the case of molecule excited by the actinic pulse. The theoretical treatment of the TR-FSRS was initially developed in a purely classical approach extended to treat pulsed Raman pump and probe [125]. The authors explicitly considered the case of molecules initially in the ground vibrational state and showed that the Stokes Raman signal follows the transient amount of excited molecules. In subsequent papers [100, 126] experimental evidence was given that the inversion of vibrational level population leads to negative gain on the Stokes side of the time-resolved Raman spectrum, what is in agreement with observations from the present dissertation. The solutions of the first-order kinetic model have been used by McCamant et al. [127] to analyze the vi-

brational dynamics in β-carotene probed by resonance Raman spectroscopy. The authors find the Raman gain on the anti-Stokes side, as due to highly excited vibrational levels of the electronic ground state. Successively the quantum mechanical theory of TR-FSRS, based on the density matrix approach, was developed by Lee et al. [74]. The authors derived the Stimulated Raman Scattering response from the perturbation theory at the third order of the density matrix and polarization expansion. They compared the results with the classical approach, taking into account coupling between light waves and vibrational modes of the medium. They pointed out the limitations of the classical approach for the case of resonance Raman and described the hot luminescence effect which may affect the Raman signal [155,177,179]. Those models were developed with the assumption of fast vibrational relaxation, which means that the whole electronically excited population was considered to be in the ground vibrational state. Such an assumption yielded the conclusion that negative Raman gain was possible only on the anti-Stokes side of the Raman spectrum. The above description was later extended for the case of a moving wave packet [150,177,179]. The dispersive shape of Raman lines in the case of resonance Raman scattering was explained [177] and compared with experimental results [150, 155, 177, 178, 180] but the situation of transient vibrational inversion of population was not described.

In this section a quantum mechanical description of molecule vibrations as a result of coupling with the light will be revised. For the purpose of the present thesis it is enough to threat the medium as a quantum mechanical system, while treating the light in a classical way. First, the light-matter interaction Hamiltonian will be introduced. Then the Heisenberg picture,

where the operators are time dependent and the wave-functions stay constant, will be introduced. The Heisenberg-Langevin equation for population and vibrational amplitudes of the molecule will be derived for a simple case of two vibrational levels in some electronic state. The distortion of the classical electric field due to interaction with a quantum-mechanical system will be discussed. Two and three vibrational level system will be examined as an example. Based on this, a model of the trans-β-apo-8'-carotenal molecule will be formed.

3.5.1 The unperturbed molecule Hamiltonian and perturbed Hamiltonian of the system

In absence of light and interaction with the surrounding the quantum mechanical description of a molecule has the form:

$$H_0\Psi = W\Psi, \tag{3.2}$$

where H_0 is the time-independent energy operator for the molecule, ψ is the molecule state wave-function and W is the energy corresponding to the state ψ. The time dependent Schrödinger equation can be solved, but all the expectation values of observables are found to be constant in time. The state of the molecule then becomes a weighted sum of eigenfunctions ϕ_n of Hamiltonian H_0 [170]:

$$\Psi(t) = \sum_n c_n e^{-\frac{iW_n t}{\hbar}} \phi_n, \tag{3.3}$$

where c_n are constants depending on the initial state of the molecule and W_n are energies of corresponding states ϕ_n, only phase factors change in time, but this does not influence of probabilities. In such a case, what is left is to solve an eigenvalue problem of equation 3.2.

Introduction of interaction of the molecule with light pulse and surrounding entails introduction of time dependence of the energy operator. In this thesis the time dependent part of Hamiltonian will be treated as a perturbation and a time-dependent perturbation theory [182] will be applied for solution of the problem. Therefore, a new Hamiltonian of the system interacting with light will become:

$$H = H_0 + H_{int} + H_B, \tag{3.4}$$

where H_{int} is the time dependent light matter interaction Hamiltonian and H_B is the part describing the interaction with the surrounding (bath or "vacuum").

There are a few ways to introduce the interaction with the electric field involving both classical, and quantum mechanical description of the field. The quantum mechanical description of light is required when fields are weak [170], which is not the case for stimulated Raman scattering. Therefore, a classical field will be used here:

$$\vec{E}(\vec{r},t) = \vec{E}_0(\vec{r},t)e^{i(\omega t - \vec{k}\vec{r})} + \vec{E}_0^*(\vec{r},t)e^{-i(\omega t - \vec{k}\vec{r})}, \tag{3.5}$$

where $\vec{r}$ is the position in space, $\vec{E}_0$ is the slowly varying envelope of the electric field, ω is the central angular frequency of electric field and $\vec{k}$ is the

field wavevector. Only the first nonzero term in the multipole expansion of the molecular charge distribution is used. In the case of molecule with zero total charge this leading term is a dipole interaction with dipole momentum μ, thus [170, 183]:

$$H_{int} = -\vec{\mu}\vec{E} \tag{3.6}$$

The bath-molecule interaction Hamiltonian H_B will be introduced in an implicit way by defining the result of its commutation with time-dependent operators, derived in the next sections. It is chosen to force the decay of the system state towards the ground state without taking on the task of the detailed description of the nature of the molecule coupling with its environment[1].

3.5.2 Time dependent operators in the Heisenberg picture

The concerned quantum-mechanical problem will be described in Heisenberg picture, where the operators are time-dependent while the space-dependent wavefunction basis is used. If the eigenfunctions $\phi_n(\vec{r})$ of the molecular Hamiltonian H_0 are used, any wavefunction ψ can be presented in this basis in a following way [183]:

$$|\psi\rangle = \sum_n b_n \phi_n(\vec{r}), \tag{3.7}$$

where b_n in Heisenberg picture become the time-dependent operators [183].

[1] Of course the most significant is the interaction with the solvent molecules.

Now the consecutive terms H_0, H_{int} and H_B can be expressed in the proposed basis 3.7. First the unperturbed molecular part:

$$\langle\psi|\, H_0\, |\psi\rangle = \sum_n \sum_m \int_{-\infty}^{\infty} \phi_n^*(\vec{r}) b_n^\dagger H_0 b_m \phi_m(\vec{r}) d^3r. \tag{3.8}$$

The functions ϕ_n are eigenfunctions of H_0 therefore for any m:

$$H_0 b_m \phi_m = W_m b_m \phi_m, \tag{3.9}$$

holds, where W_m are the corresponding energies of the states. Thus by use of Eq. 3.9, the Eq. 3.8 becomes:

$$\begin{aligned} \langle\psi|\, H_0\, |\psi\rangle &= \sum_n \sum_m W_m b_n^\dagger b_m \int_{-\infty}^{\infty} \phi_n^*(\vec{r}) \phi_m(\vec{r}) d^3r \\ &= \sum_n \sum_m W_m b_n^\dagger b_m \delta_{mn} = \sum_n W_n b_n^\dagger b_n, \end{aligned} \tag{3.10}$$

Similarly for the $H_{int} = -\mu E$:

$$\begin{aligned} -\langle\psi|\, \mu E\, |\psi\rangle &= -\sum_n \sum_m \int_{-\infty}^{\infty} \phi_n^*(\vec{r}) b_n^\dagger \mu(\vec{r}) E b_m \phi_m(\vec{r}) d^3r \\ &= -\sum_n \sum_m b_n^\dagger b_m E \int_{-\infty}^{\infty} \phi_n^*(\vec{r}) \mu(\vec{r}) \phi_m(\vec{r}) d^3r \\ &= -\sum_n \sum_m b_n^\dagger b_m E \mu_{nm}, \end{aligned} \tag{3.11}$$

where $\mu_{nm} = \int_{-\infty}^{\infty} \phi_n^*(\vec{r}) \mu(\vec{r}) \phi_m(\vec{r}) d^3r$. In the above expression the electric field was assumed not to change much over the molecule and therefore its spatial dependence has been neglected. This is a valid approach as the

wavelength of the light ($\sim$ 1μm) is much longer from the dimensions of the molecule ($\sim$ 1nm). As $\mu_{nn} = 0$ equation 3.11 becomes:

$$-\langle\psi|\,\mu E\,|\psi\rangle = -\sum_{n\neq m} {b_n}^{\dagger} b_m E\mu_{nm}, \tag{3.12}$$

where E is given by Eq. 3.5. Finally, no explicit form of the bath-molecule interaction Hamiltonian will be given, but H_B is chosen to force the decay of the systems state towards the ground state. Thus, for a two-level system [146, 183, 184]:

$$\frac{i}{\hbar}\left\langle [H_B, b_0^{\dagger}b_0]\right\rangle_B = \Gamma_1 b_1^{\dagger}b_1 - \Gamma_0 b_0^{\dagger}b_0, \tag{3.13}$$

$$\frac{i}{\hbar}\left\langle [H_B, b_1^{\dagger}b_1]\right\rangle_B = -\Gamma_1 b_1^{\dagger}b_1, \tag{3.14}$$

$$\frac{i}{\hbar}\left\langle [H_B, b_0^{\dagger}b_1]\right\rangle_B = -\gamma_{01} b_0^{\dagger}b_1, \tag{3.15}$$

where Γ_1, Γ_0, γ_{01} are vibrational state decay rate, electronic state decay rate and decoherence rate, respectively and $\langle . \rangle_B$ denotes averaging over bath states.

3.5.3 Heisenberg-Langevin equations of the two-level system

Heisenberg-Langevin equations of motion can now be derived using following expression:

$$\begin{aligned}\left\langle d_t b_l^{\dagger}b_k\right\rangle_B &= \frac{i}{\hbar}\left\langle [H, b_l^{\dagger}b_k]\right\rangle_B \\ &= \frac{i}{\hbar}\left(\left\langle [H_0, b_l^{\dagger}b_k]\right\rangle_B + \left\langle [H_{int}, b_l^{\dagger}b_k]\right\rangle_B + \left\langle [H_B, b_l^{\dagger}b_k]\right\rangle_B\right),\end{aligned} \tag{3.16}$$

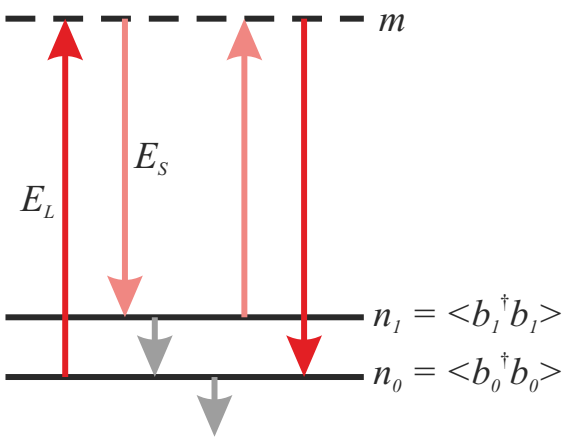

Figure 3.28: Energy scheme for two vibrational levels in some electronic state. The gray arrows represent decay due to interaction with surroundings.

The exact derivation of the set of four differential equations set for a simple case of two vibrational levels in some electronic state (see Fig. 3.28) is presented in the appendix B. The electric field with two frequencies ω_L and ω_S:

$$E(t) = E_L(t)e^{i\omega_L t} + E_L^*(t)e^{-i\omega_L t} + E_S(t)e^{i\omega_S t} + E_S^*(t)e^{-i\omega_S t} \tag{3.17}$$

where $\omega_L - \omega_S = \omega_{10}$ is the frequency difference between the vibrational levels and $E_L(t)$ and $E_S(t)$ are the slowly varying amplitudes of the field was used. The equations are as follows:

$$\begin{aligned} d_t n_0 &= \Gamma_1 n_1 - \Gamma_0 n_0 + \frac{i}{\hbar}\left(K_{01}Q_{01}E_L E_S^* - K_{10}Q_{10}E_S E_L^*\right) \\ d_t n_1 &= -\Gamma_1 n_1 + \frac{i}{\hbar}\left(K_{10}Q_{10}E_L^* E_S - K_{01}Q_{01}E_L E_S^*\right) \\ d_t Q_{01} &= -\gamma_{01}Q_{01} - \frac{i}{\hbar}E_L^* E_S\left(n_1 - n_0\right)K_{10} \end{aligned} \tag{3.18}$$

where mean and slowly varying amplitudes for the off-diagonal operators: $\left\langle b_n^\dagger b_l \right\rangle = Q_{nl} e^{i\omega_{nl}t}$, with $\omega_{nl} = \left|\frac{1}{\hbar}(W_n - W_l)\right| > 0$ are used and the diagonal operators (vibrational level populations) are $\left\langle b_l^\dagger b_l \right\rangle = n_l$, where $\langle . \rangle$ denotes average over the ensemble, the "Kramers-Heisenberg-Dirac expresions" [185, 186] are:

$$K_{kl} = \frac{1}{\hbar} \sum_m \mu_{km}\mu_{ml} \left(\frac{1}{\omega_{m0} - \omega_L} + \frac{1}{\omega_{m0} + \omega_s} \right), \tag{3.19}$$

where the sum is over all virtual levels m. Additional complex equation for Q_{10} is complex conjugate of the equation for Q_{01}. Equations 3.18. can be written in an equivalent, shorter form:

$$\begin{aligned} d_t n_0 &= \Gamma_1 n_1 - \Gamma_0 n_0 - \frac{2}{\hbar} \Im\{K_{01} Q_{01} E_L E_S^*\} \\ d_t n_1 &= -\Gamma_1 n_1 + \frac{2}{\hbar} \Im\{K_{01} Q_{01} E_L E_S^*\} \\ d_t Q_{01} &= -\gamma_{01} Q_{01} - \frac{i}{\hbar} E_L^* E_S \left(n_1 - n_0\right) K_{10} \end{aligned} \tag{3.20}$$

where $\Im\{a\}$ stands for the imaginary part of a[2]. For the system in the ground state the initial conditions in equation set 3.20. are as follows:

$$n_0 = 1, \quad n_1 = 0, \quad Q_{01} = 0. \tag{3.21}$$

With those initial conditions the impulsive excitation of the system can be introduced by adding a $-\alpha I_E$ term in the first and αI_E term in the second equation in 3.20. where α is the adsorption coefficient and $I_E(t)$ is the intensity of the exciting pulse[3].

[2] If $a = x + iy$, than $\Im\{a\} = y$

[3] This corresponds to infrared excitation rather than actinic pump used for electronic excitation in TR-FSRS experiment.

If additionally, adiabatic approximation: $d_t Q_{01} \approx 0$, valid when: $\gamma_{01} > \Gamma_1, \Gamma_2, \frac{1}{\Delta t_S}, \frac{1}{\Delta t_L}$ (where Δt_S and Δt_L are the characteristic times of the electric field envelope) is applied, the equation 3.20 can be solved approximately:

$$Q_{01} \approx -\frac{i}{\gamma_{01}\hbar} E_L^* E_S \left(n_1 - n_0\right) K_{10}. \tag{3.22}$$

In such a case the system 3.20. transforms into:

$$\begin{aligned} d_t n_0 &= \Gamma_1 n_1 - \Gamma_0 n_0 + 2D_{01}|E_L|^2|E_S|^2(n_1 - n_0) \\ d_t n_1 &= -\Gamma_1 n_1 - 2D_{01}|E_L|^2|E_S|^2(n_1 - n_0) \end{aligned} \tag{3.23}$$

with the line strength coefficient:

$$D_{01} = \frac{K_{10}K_{01}}{\hbar^2\gamma_{01}} = \frac{|K_{10}|^2}{\hbar^2\gamma_{01}}. \tag{3.24}$$

3.5.4 Influence on the electric field

The electric field is treated in the present model in a classical way, therefore it is disturbed by interaction with the molecule through the nonlinear part of the polarization [147]:

$$P = \sum_m \left(\mu_{m0} b_m^\dagger b_0 + \mu_{1m} b_1^\dagger b_m + \mu_{0m} b_0^\dagger b_m + \mu_{m1} b_m^\dagger b_1\right). \tag{3.25}$$

The contributions at two frequencies ω_S and ω_L are interesting, therefore if:

$$P(t) = P_S(t)e^{i\omega_S t} + P_S^*(t)e^{-i\omega_S t} + P_L(t)e^{i\omega_L t} + P_L^*(t)e^{-i\omega_L t} \tag{3.26}$$

then, as shown in the appendix B.3:

$$P_S(t) = K_{01} Q_{01} E_L, \tag{3.27}$$

or under adiabatic approximation ($d_t Q_{10} \approx 0$):

$$P_S(t) = -iD_{10}|E_L|^2 E_S(n_1 - n_0). \tag{3.28}$$

The wave equation can be solved approximately (see appendix B.4) to give a formula for SRS signal:

$$S = -i\frac{\omega_S}{2\epsilon_0 n^2} K_{01} \int_0^\infty Q_{01} E_L dt', \tag{3.29}$$

or:

$$S = -\frac{\omega_S}{\epsilon_0 n^2} D_{10} \int_0^\infty |E_L|^2 E_S(n_1 - n_0) dt' \tag{3.30}$$

for the approximated case, where n is the refractive index of the solution.

3.5.5 Discussion of the two-level system's model

Both equations 3.20. and 3.23. were solved numerically. Their results are indistinguishable for all values of decoherence rate γ_{10} (both slightly and significantly higher and lower from other time related constants). Population of the upper state was created with a 70 fs Gaussian pulse ($I_E(t)$ as discussed in section 3.5.3.), while the lower level is populated only by the decay of the upper state. The envelopes of Raman pump and probes were also Gaussian functions with 1 ps and 70 fs widths, respectively. The vibrational lifetime of

the upper state was set to constant 1 ps while the electronic lifetime (lifetime of lower state) was changed. The evolution of populations n_1 and n_0 of the two states for different lower state lifetimes is presented in Figures 3.29. and 3.30. The population of the upper state, as expected, do not depend on the decay time of the lower state. A long living lower state can be populated significantly by decay of the upper state before its own decay. In carotenoids such situation is expected to occur in S_1 state, where the electronic lifetime (25 – 30 ps) is longer than the vibrational lifetime. On the other hand, a short living lower level can't store a significant population. This could be the case of S_2 level, decaying within 100 – 200 fs. The time-resolved femtosecond stimulated Raman scattering signal was calculated according to equations 3.29. and 3.30, it is presented on the figure 3.31. A negative signal occurs for all lifetimes. For long life times of the lower level this negative signal becomes positive, while for the case of lower states shorter than the life time of the upper state the signal stays negative. Both signal behaviors, are reflected in the dynamics of the levels population described above. In the first case a significant population of the lower state is created, therefore a Raman process starting from the lower state and ending in the upper state is possible. In the second case the population of the lower level is always smaller then the population of the upper state and the Raman process starting from the upper state and ending at the lower state is more probable.

3.5.6 Discussion of the three-level system's model

The formulation of model for multilevel system is straightforward and can be perfrmed by analogy to the two-level model. Equations 3.18. for a

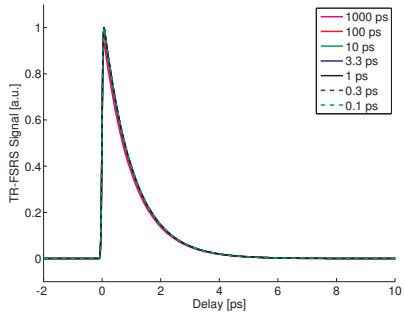

Figure 3.29: Evolution of the upper state population for the two-level system for various lower state lifetimes. As expected, the evolution is governed by the lifetime of the upper state.

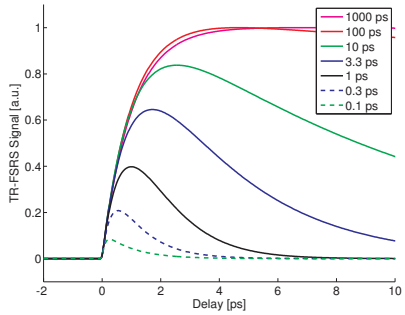

Figure 3.30: Evolution of the lower state population for the two-level system for various lower state lifetimes. The evolution growth of population is governed by the lifetime of the upper state, the decay strongly depends on the level lifetime.

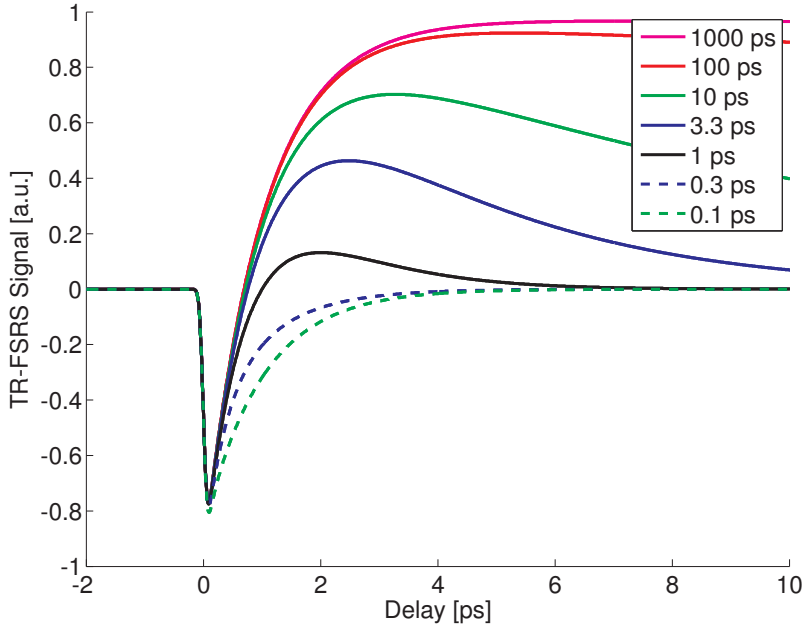

Figure 3.31: The time-resolved femtosecond stimulated Raman scattering signal for various lower state lifetimes. A negative to positive signal transition occures for long living lower states while a completely negative signal can be observed when lower level has a short life time.

three-level system transform into:

$$\begin{aligned}
d_t n_0 &= -\alpha_1 I_1 - \alpha_2 I_2 + \Gamma_1 n_1 - \Gamma_0 n_0 + \frac{i}{\hbar}\left(K_{01} Q_{01} E_L E_S^* - K_{10} Q_{10} E_S E_L^*\right) \\
d_t n_1 &= \alpha_1 I_1 + \Gamma_2 n_2 - \Gamma_1 n_1 - \frac{i}{\hbar}\left(K_{01} Q_{01} E_L E_S^* - K_{10} Q_{10} E_S E_L^*\right) \\
&\quad + \frac{i}{\hbar}\left(K_{12} Q_{12} E_L E_S^* - K_{21} Q_{21} E_S E_L^*\right) \\
d_t n_2 &= \alpha_2 I_2 - \Gamma_2 n_1 - \frac{i}{\hbar}\left(K_{12} Q_{12} E_L E_S^* - K_{21} Q_{21} E_S E_L^*\right) \\
d_t Q_{01} &= -\gamma_{01} Q_{01} - \frac{i}{\hbar} E_L^* E_S \left(n_1 - n_0\right) K_{10} \\
d_t Q_{12} &= -\gamma_{12} Q_{12} - \frac{i}{\hbar} E_L^* E_S \left(n_2 - n_1\right) K_{21}
\end{aligned} \tag{3.31}$$

where population of a higher excited level n_2 and a coherence of the first and second excited levels Q_{12} were introduced, Γ_2 is the decay ratio of the level 2, γ_{12} is the decoherence ratio and K_{12} is defined with equation 3.19. The population of n_1 or n_2 can be created through excitation $\alpha_1 I_1$ or $\alpha_2 I_2$, respectively. Then the TR-FSRS signal becomes:

$$S = -i\frac{\omega_S}{2\epsilon_0 n^2}\left(K_{01}\int_0^\infty Q_{01} E_L dt' + K_{12}\int_0^\infty Q_{12} E_L dt'\right), \tag{3.32}$$

The set of approximated equations 3.23. transforms into:

$$\begin{aligned}
d_t n_0 &= -\alpha_1 I_1 - \alpha_2 I_2 + \Gamma_1 n_1 - \Gamma_0 n_0 + 2D_{01}|E_L|^2|E_S|^2(n_1 - n_0) \\
d_t n_1 &= \alpha_1 I_1 + \Gamma_2 n_2 - \Gamma_1 n_1 - 2D_{01}|E_L|^2|E_S|^2(n_1 - n_0) \\
&\quad + 2D_{12}|E_L|^2|E_S|^2(n_2 - n_1) \\
d_t n_2 &= \alpha_2 I_2 - \Gamma_2 n_2 - 2D_{12}|E_L|^2|E_S|^2(n_2 - n_1)
\end{aligned} \tag{3.33}$$

with:

$$D_{12} = \frac{|K_{12}|^2}{\hbar^2 \gamma_{12}}. \tag{3.34}$$

and the TR-FSRS signal is:

$$S = -\frac{\omega_S}{\epsilon_0 n^2} \left(D_{10} \int_0^\infty |E_L|^2 E_S(n_1 - n_0) dt' + D_{21} \int_0^\infty |E_L|^2 E_S(n_2 - n_1) dt' \right). \tag{3.35}$$

As expected, for the three-level case the two models, based on equation 3.31. and 3.33. give similar results for fast decoherence $\gamma_{01}, \gamma_{12} > \Gamma_0, \Gamma_1, \Gamma_2$[4]. Figure 3.32. presents a simulation results for equations 3.31. and 3.33 for various decoherence ratios. Here the level 2 is populated with a 70 fs Gaussian pulse ($\alpha_1 I_1 = 0, \alpha_2 I_2 \neq 0$), Raman pump and probe are 1 ps and 70 fs, respectively. The life times of levels 2, 1 and 0 are 0.5, 1 and 5 ps, respectively. The line strength coefficients are $D_{12} = 2D_{01}$ and K_{12} and K_{01} were calculated from values of D_{12} and D_{01}[5]. The same as for the two-level model, the signal goes from negative to positive values. For fast decoherence approximated model is in agreement with the exact one.

In anharmonic potential wells the energy separation of consecutive vibrational levels is not equal. In such a case for a given frequency of the Raman pump multiple frequencies of the probe field are required to force transition between different state pairs. For example fields E_S^{01} and E_S^{12} tuned to $0 \longrightarrow 1$ and $1 \longrightarrow 2$ transitions with frequencies ω_{01} and ω_{12}, respectively, should be introduced for a three-level system. Figure 3.33. presents a three-level system of such a kind, together with possible stimulated Raman

[4]Apart of a special case, when a condition $\gamma_{01} = \gamma_{12}$ is satisfied. Then similarity is assured for any value of γ_{01} and γ_{12}.

[5]The ratio $D_{12} = 2D_{01}$ is expected for vibrational levels in harmonic potential [170].

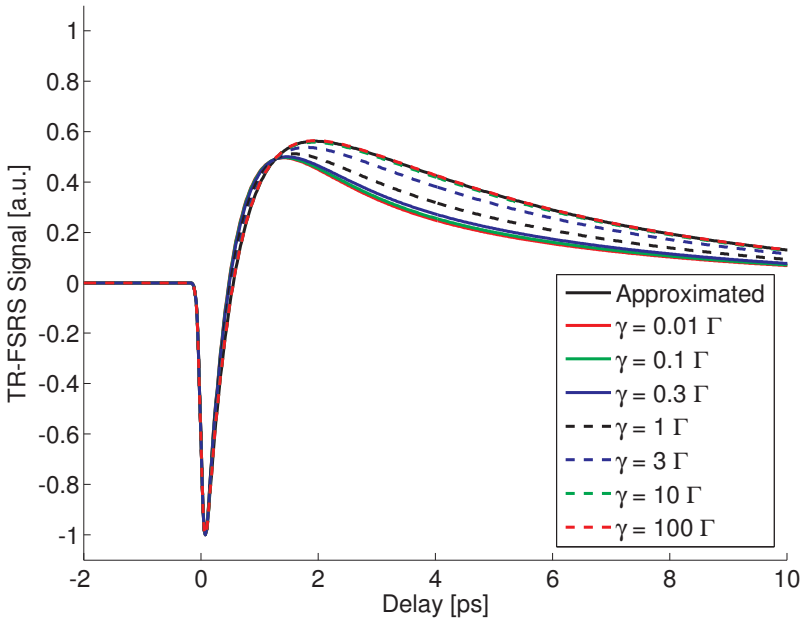

Figure 3.32: The comparison of exact and approximated model for three-level system. The result for the approximated model overlaps with exact model results for $\gamma = 10\Gamma$ and $\gamma = 100\Gamma$.

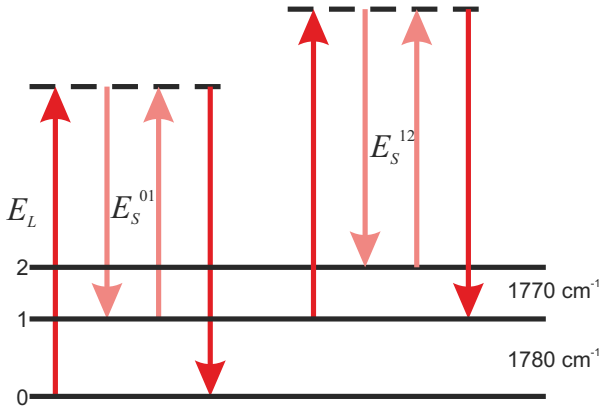

Figure 3.33: The three-level system (levels 0, 1 and 2) with unequal levels separation (1780 and 1770 cm^{-1}).

transitions. In principle, in such a case, the Raman probe E_S in equations 3.31. and 3.33. should be replaced by E_S^{01} and E_S^{12}. Still if one assumes that two frequencies have similar amplitudes: $E_S^{01} = E_S^{12} = E_S$ (this is the case in the experiment as the energy differences are small in comparison to the probe frequency intensity variation), then no change of the equations 3.31. and 3.33 is required. It is however important to distinguish the two probe frequencies during detection – equation 3.32. now splits into:

$$\begin{aligned} S(\omega_{01}) &= -i\frac{\omega_S}{2\epsilon_0 n^2}K_{01}\int_0^\infty Q_{01}E_L dt', \\ S(\omega_{12}) &= -i\frac{\omega_S}{2\epsilon_0 n^2}K_{12}\int_0^\infty Q_{12}E_L dt', \end{aligned} \tag{3.36}$$

and equation 3.35. into:

$$\begin{aligned} S(\omega_{01}) &= -\frac{\omega_S}{\epsilon_0 n^2}D_{10}\int_0^\infty |E_L|^2 E_S(n_1 - n_0)dt', \\ S(\omega_{12}) &= -\frac{\omega_S}{\epsilon_0 n^2}D_{21}\int_0^\infty |E_L|^2 E_S(n_2 - n_1)dt', \end{aligned} \tag{3.37}$$

In the experiment the change of the Raman line frequency was observed and a position of the peek central frequency was recovered by Gaussian function fitting to the broad Raman line shape (see Figure 3.27. in section 3.4.1), which as is assumed here, contains indistinguishable frequencies of vibrational transitions within its shape. This observable can be simulated here by calculation of weighted frequency average of vibrational transitions frequencies like:

$$\bar{\omega} = \frac{S(\omega_{01})\omega_{01} + S(\omega_{12})\omega_{12}}{S(\omega_{01}) + S(\omega_{12})}. \tag{3.38}$$

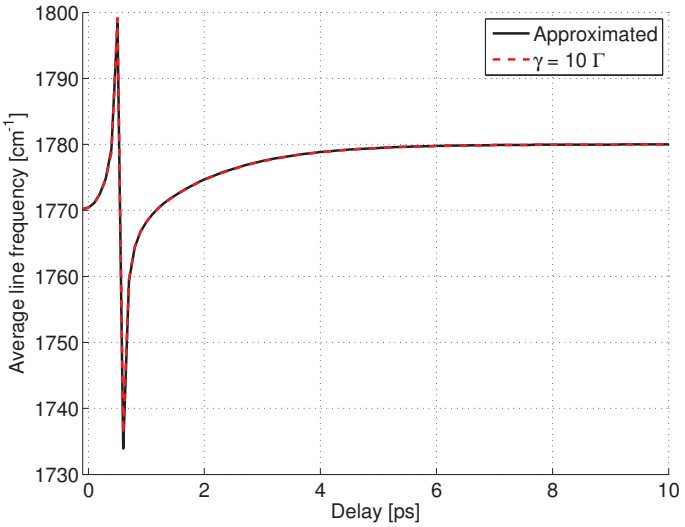

Figure 3.34: Weighted frequency average as calculated with equation 3.38. for both approximated and exact three level model.

Figure 3.34. presents weighted frequency average as calculated with equation 3.38. for parameters described before and frequency differences of the upper (1, 2) and lower (0, 1) level pairs equal to 1770 and 1780 cm^{-1}, respectively. The start frequency is equal to the frequency shift between the upper levels (1770 cm^{-1}), in fact, at that time the upper levels are most populated, so no transitions between two lower levels are possible. Later, as the lower levels become populated, the average frequency is increased. Similarly as observed in the experiment the frequency goes through singularity when the signal (see figure 3.32) passes through zero. Both numerator and denominator in equation 3.38 decay towards zero fast in vicinity of that point. Later the frequency increases further towards the frequency separation between the lower levels (1780 cm^{-1}). At that time the level 0 becomes most populated.

Another very important numerical experiment can be performed for the simple three-level system. This is the case when the level 1 is populated instead of level 2 ($\alpha_1 I_1 \neq 0, \alpha_2 I_2 = 0$). The resulting signal for such a condition is presented in figure 3.35. In such a case, if $D_{12} > D_{01}$ (which is the case for harmonic potential [170, 184]), it is impossible to observe a negative signal.

This can be easily understood, level 2 has zero population (or very small population due only to population by Raman effect) and the population of the lowest level grows due to decay of the level 1, therefore: From Eq. 3.35. one can see that the FSRS signal is positive when:

$$S > 0 \Leftrightarrow D_{21}(n_1 - n_2) > D_{10}(n_1 - n_0)$$

if $n_2 = 0, n_1 = n - \delta n$ and $n_0 = \delta n$ this transforms into:

$$\frac{D_{21}}{D_{10}} > 1 - \frac{2\delta n}{n} > 0$$

which is always true (as $D_{12} > D_{01}$) and thus the signal in equation 3.35. has to be positive. In harmonic potentials, with constant energy separation between consecutive levels, there always is the next higher vibrational level on the vibrational ladder. In such a case no negative Raman gain could be observed even if vibrational inversion of population is present. In the case of anharmonic potentials the energy of levels becomes closer and closer with their difference converging to zero with growing vibrational quantum number. Here, in the presence of population inversion a negative signal can be observed in part of the spectrum corresponding to highly energetic

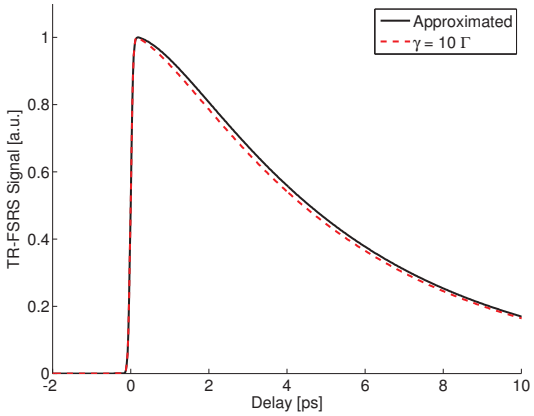

Figure 3.35: A TR-FSRS signal from a three-level system when a middle level is populated. The signal in such a case is never negative. The exact and approximated model solution is presented.

transitions (for the bottom states) while a positive signal is present in low energetic part of the spectrum (corresponding to top states). Depending on the exact shape of the potential well the separation of those spectral features can be significant.

3.6 Model for trans-β-apo-$8'$-carotenal molecule

Herewith each trans-β-apo-$8'$-carotenal molecule is described as a three electronic level system (see figure 3.37 and 3.36.). All electronic levels are split into vibrational sublevels; the energy gap between them differs in each electronic state due to the strong vibronic coupling leading to different shapes of the potential wells. The actinic pulse prepares the molecule in the excited state S_2, which decays to a highly excited vibrational sublevel of the S_1

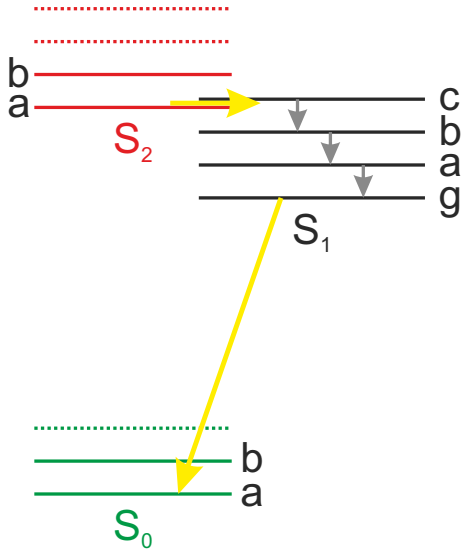

Figure 3.36: The energy scheme for trans-β-apo-8′-carotenal molecule used for formulation of the model. Four vibrational levels are assumed in the electronic state S_1 while two vibrational levels are assigned to S_0 and S_2. While, all vibrational levels in S_1 can be populated, the vibrationally excited sublevels of S_0 and S_2 are assumed to be empty. The transitions described by the model are marked with arrows.

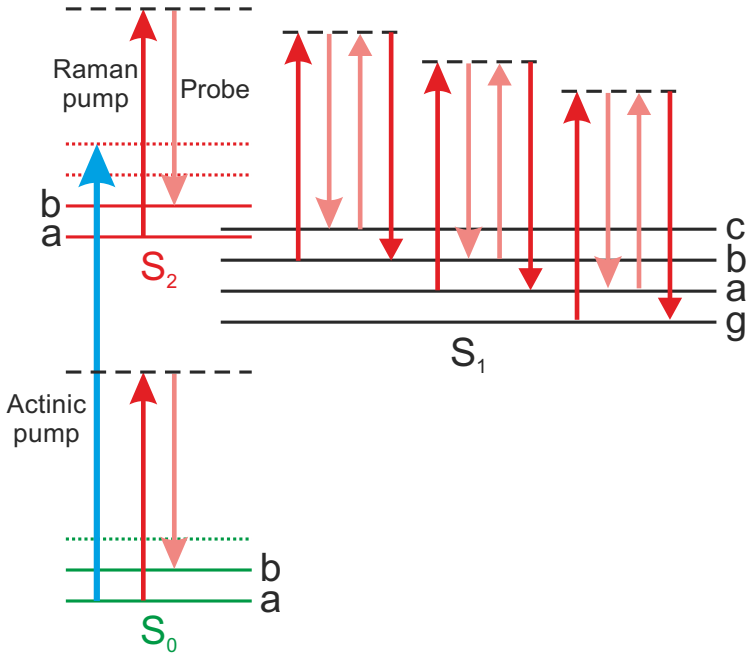

Figure 3.37: The energy scheme for trans-β-apo-8′-carotenal molecule used for formulation of the model. The possible stimulated Raman transitions are marked.

state. This vibrational state can be depopulated via intramolecular energy redistribution (IVR); the excess energy is then released to the surrounding (the bath) and the system reaches the bottom of the potential well of level S_1. Finally, internal conversion (IC) brings the system back to the ground state S_1. Apart from the activation, all the considered transitions are nonradiative and take place within hundreds of femtoseconds or picoseconds.

The level S_1 is of main interest here, therefore, only it is considered to be split into a number of vibrational sublevels. Four sublevels c, b, a and g are proposed as this number fits the energy difference of about 5000 cm^{-1} between the bottom sublevels of S_2 and S_1 states [96,111]. In case of β-carotene this difference is 5800 cm^{-1} [127], there the decay from S_2 into third excited level of S_1 was also suggested by McCammant et. al. [144]. According to the experimental observation we assume that the energy gap between the adjacent states slightly decreases with increasing vibrational number of the state: $\omega_{ga} > \omega_{ab} > \omega_{bc}$. This is characteristic for an anharmonic potential with negative anharmonicity [176]. The Raman transition occurs between the succeeding vibrational sublevels of the electronic level S_1. In order to be able to consider Raman transitions in electronic levels S_0 and S_2 an unspecified pair (a and b) of vibrational sublevels is assigned to each level. It is, however, assumed that the population of the higher vibrational level remains negligible.

Two models of the molecule, with use of the exact and approximated approach, are tested. The ordinary differential equations for populations and vibrational amplitudes for the exact "Model 1" are based on the generic set of equations 3.20. extended in a way similar to the extension performed

for three-level system. The equations for the populations of four vibrational levels of electronic level S_1 are:

$$d_t n_c = \Gamma_2 n_2 - \Gamma_c n_c + \frac{2}{\hbar}\Im\{K_{bc}Q_{bc}E_L E_S^*\}, \tag{3.39}$$

$$d_t n_b = -\Gamma_b n_b - \frac{2}{\hbar}\Im\{K_{bc}Q_{bc}E_L E_S^*\} + \frac{2}{\hbar}\Im\{K_{ab}Q_{ab}E_L E_S^*\}, \tag{3.40}$$

$$d_t n_a = -\Gamma_a n_a - \frac{2}{\hbar}\Im\{K_{ab}Q_{ab}E_L E_S^*\} + \frac{2}{\hbar}\Im\{K_{ga}Q_{ga}E_L E_S^*\}, \tag{3.41}$$

$$d_t n_g = -\Gamma_g n_g - \frac{2}{\hbar}\Im\{K_{ga}Q_{ga}E_L E_S^*\}, \tag{3.42}$$

the vibrational amplitudes:

$$d_t Q_{bc} = -\gamma_{bc}Q_{bc} - \frac{i}{\hbar}E_L^* E_S\left(n_c - n_b\right)K_{cb}, \tag{3.43}$$

$$d_t Q_{ab} = -\gamma_{ab}Q_{ab} - \frac{i}{\hbar}E_L^* E_S\left(n_b - n_a\right)K_{ba}, \tag{3.44}$$

$$d_t Q_{ga} = -\gamma_{ga}Q_{ga} - \frac{i}{\hbar}E_L^* E_S\left(n_a - n_g\right)K_{ag}, \tag{3.45}$$

populations of the ground and S_2 states:

$$d_t n_{0a} = -\alpha I_A(t) + \Gamma_g n_g - \frac{2}{\hbar}\Im\{K_{0a0b}Q_0 E_L E_S^*\}, \tag{3.46}$$

$$d_t n_{0b} = \frac{2}{\hbar}\Im\{K_{0a0b}Q_0 E_L E_S^*\}, \tag{3.47}$$

$$d_t n_{2a} = \alpha I_A(t) - \Gamma_2 n_{2a} - \frac{2}{\hbar}\Im\{K_{2a2b}Q_2 E_L E_S^*\}, \tag{3.48}$$

$$d_t n_{2b} = \frac{2}{\hbar}\Im\{K_{2a2b}Q_{2a2b}E_L E_S^*\}, \tag{3.49}$$

and corresponding vibrational amplitudes:

$$d_t Q_0 = -\gamma_0 Q_0 - \frac{i}{\hbar} E_L^* E_S \left(n_{0b} - n_{0a}\right) K_{0b0a}, \tag{3.50}$$

$$d_t Q_2 = -\gamma_2 Q_2 - \frac{i}{\hbar} E_L^* E_S \left(n_{2b} - n_{2a}\right) K_{2b2a}, \tag{3.51}$$

where the decay ratios Γ_k, with $k = 2, g, a, b, c$ are population decays, γ_{kl} with $k = 0, 2, g, a, b, c$ are the decoherence ratios and α is the actinic pump absorption coefficient, $I_A(t)$ is the intensity of the actinic pump.

The "Model 2" constructed with use of the adiabatic approximated equations 3.23 is as follows. The populations of the S_1 vibrational states are:

$$d_t n_c = \Gamma_2 n_2 - \Gamma_c n_c - 2D_{bc}|E_L|^2|E_S|^2(n_c - n_b), \tag{3.52}$$

$$d_t n_b = \Gamma_c n_c - \Gamma_b n_b + 2D_{bc}|E_L|^2|E_S|^2(n_c - n_b) - 2D_{ab}|E_L|^2|E_S|^2(n_b - n_a), \tag{3.53}$$

$$d_t n_a = \Gamma_b n_b - \Gamma_a n_a + 2D_{ab}|E_L|^2|E_S|^2(n_b - n_a) - 2D_{ga}|E_L|^2|E_S|^2(n_a - n_g), \tag{3.54}$$

$$d_t n_g = \Gamma_a n_a - \Gamma_g n_g + 2D_{ga}|E_L|^2|E_S|^2(n_a - n_g), \tag{3.55}$$

and populations of states S_0 and S_2 are:

$$d_t n_0 = -\alpha I_A(t) + \Gamma_g n_g \tag{3.56}$$

$$d_t n_2 = \alpha I_A(t) - \Gamma_2 n_2 \tag{3.57}$$

here the populations of the vibrationally excited states of S_0 and S_2 were neglected.

3.7 Numerical aspects of model fitting

Fitting of the model parameters to the experimental data is time consuming. For each delay a system of 13 (Model 1) or 6 (Model 2) ordinary differential equations has to be solved for a range of time points. The time range has to start before excitation and end after intensity of the probe pulse decreases significantly. The probe pulse maximum delay time in the experiment is around 200 ps. At the same time the excitation and probing with pulses as short as 70 fs has to be properly reflected, thus the time resolution of at least 25 fs is required, giving 8000 time points. The polarization, Raman gain and finally FSRS signal for particular delay is obtained by integration of result of differential equation with the envelope of the probe pulse (see Eqs. 3.29. and 3.30.). This procedure has to be performed for each of around 200 experimental points to obtain delay dependent FSRS signal. Only then the signal can be compared with the experimental data and a single step of the fitting optimization can be accomplished. The fitting itself requires around a thousand steps to converge. Therefore fitting procedure requires potentially hundreds of millions of evaluations of a system of differential equations for various parameter values.

In order to perform the fitting within one week rather than five years a parallel ordinary differential equation solver, working with graphical processing unit, developed previously for solution of plasma dynamics in the supercontinuum generation problem was modified and used (see appendix A).

The code was generalized to solve multidimensional problems. Additionally each clone of the set of equations can be solved for different initial

conditions. This second modification is required for performing parallel computations for large number of time points and multidimensional problems. In such cases the whole solution, for all time points, frequently cant fit the limited memory of graphical card. Then the calculation for a smaller time range has to be performed, the solution has to be moved to computer RAM and the last time point of this solution can be used for calculation of the next range. By use of the solver the single set of equations was solved for various time delay's at the same time. A parallel trapezoid integration routine was also developed for FSRS signal calculation.

For fitting procedure two MATLAB build in methods were employed: Nelder-Mead simplex method and Levenberg-Marquardt algorithm. For analyzed problem the first one was found to converge faster than the latter one.

The estimation of the parameters' fitting errors was based on the value of χ^2 and the covariance matrix of the minimized function [187]. The derivatives required for construction of the covariance matrix were calculated numerically.

3.8 Modeling results and discussion

To form the kinetics corresponding to the FRSR signal for the three states (S_0, S_1 and S_2) the data were integrated along the frequency axis. Model 2 was fitted to the experimental data. The values of the decay rates, frequencies and line strengths from Model 2 were introduced into Model 1, then fitting of Model 1 was performed. Figure 3.39. and 3.38. presents the time evolution of

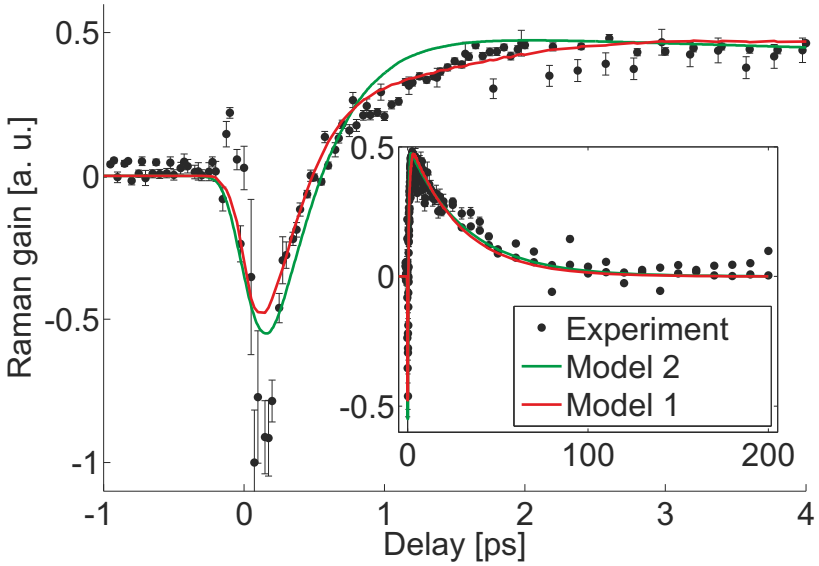

Figure 3.38: The delay dependance of Raman line corresponding to the S_1 electronic state, experimental results and fit of two models.

the Raman signals corresponding to S_2 and S_1 states. Figure 3.40. shows the time evolution of the central frequency of the Raman line in S_1. Both models seem to reflect the behavior of the measured signal. Moreover, all the values of the decoherence rate obtained from the Model 1 are an order of magnitude higher than the decay rates, therefore, the adiabatic approximation seems justified. Thus, the first conclusion is that the adiabatic approximation and thus Model 2 is valid in the present case.

It is for sure valuable to possess a valid and exact model as Model 1, it is however also valuable to possess a simple model which can be easily interpreted and can help to create intuitions about the system behavior. In the present case not only both models exist but they also are self consistent and both reflect the experimental situation well. Thus, further discussion

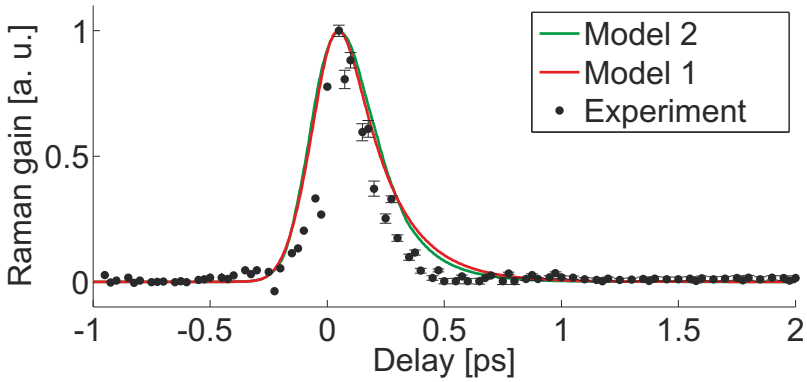

Figure 3.39: The delay dependance of Raman line corresponding to the S_2 electronic state, experimental results and fit of two models.

will be limited to the results of the Model 2 fit. The values of the obtained parameters are presented in Table 3.1. As expected, we find that the energy gap of the consecutive vibrational levels decreases with increasing vibrational quantum number. This behavior is characteristic for anharmonic potentials. The difference between the succeeding energy gaps and thus also the anharmonicity that we retrieve for the analized molecule, based on the parameters obtained from the fit, is not as large as that reported for β-carotene (30 cm^{-1}) [100, 101, 126]. However, the total difference of 17 cm^{-1} detected in our experiment corresponding to 1 % change of the frequency is, consistent with about 15 cm^{-1} between 200 fs and 30 ps [127] and recently measured 5 cm^{-1} in the range from 300 to 800 fs after excitation [118] in β-carotene.

The fast decay, of about 110 fs of the S_2 electronic state, is consistent with previous observations in β-carotene [123, 130]. For the time constants describing the decay of the vibrational levels, we obtained the following values: 313 fs for the highest one (c), 388 fs and 624 fs for the two lower levels (b) and (a), respectively. The values of the decay times fulfill the relation

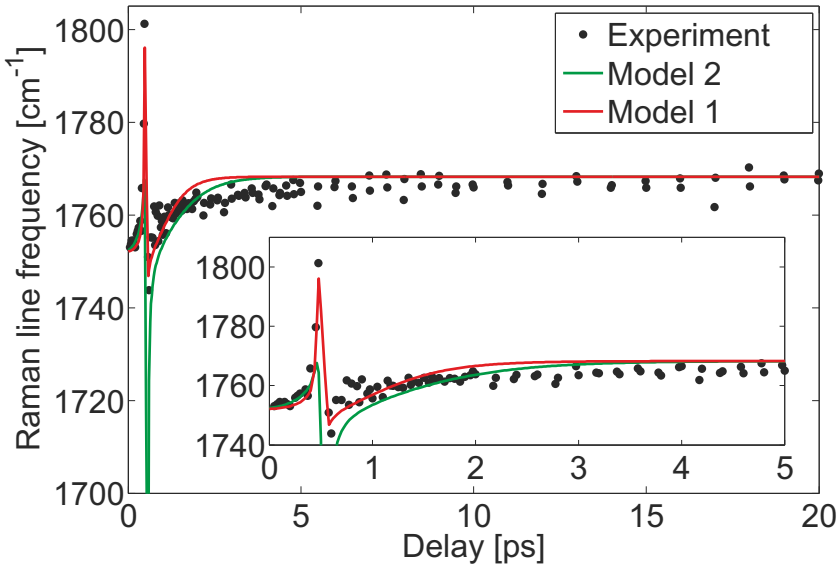

Figure 3.40: The delay dependance of Raman line frequency in the S_1 electronic state, experimental results and fit of two models.

$\Gamma_c > \Gamma_b > \Gamma_a$. The linear dependence of the decay rates on the vibrational quantum number, known from the harmonic potential [188, 189], is fulfilled within a half of the $\Gamma_c, \Gamma_b, \Gamma_a$ fit error. Discrepancies are expected for the anharmonic potential. The line strength coefficients D_{mn} also fulfill the relation characteristic for the harmonic potential. In fact, they correspond to the Raman cross sections, which for non-resonant Raman scattering are proportional to the square matrix element for one phonon transitions [170]. The results of the fit give: $D_{cb}/D_{ba}/D_{ag} = 3.06/2.03/1$. The internal conversion process from the relaxed S_1 to ground state S_0 takes about 30 ± 6 ps; the large error is the consequence of the low value (250 ps) of the longest pump-probe delay time used in the experiments. A decay time in this range has been reported for S_1 by other authors [90, 107–109].

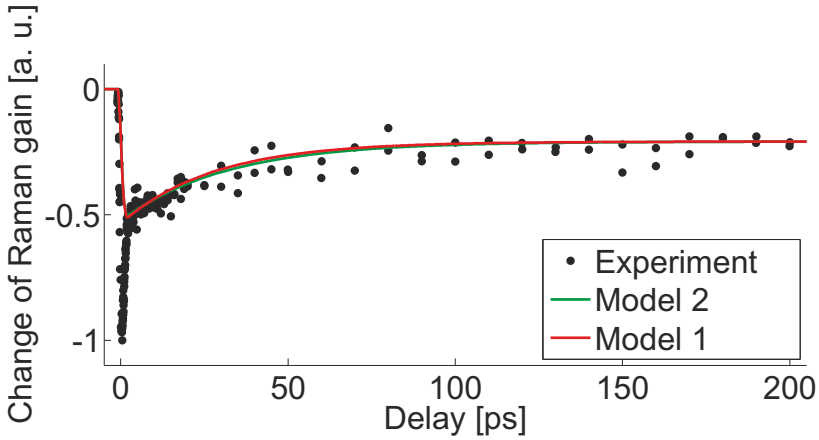

Figure 3.41: The delay dependance of Raman line corresponding to the S_0 electronic state, experimental results and fit of two models.

The agreement between the experimental data and modeling results suggest that no dark $1B_u^-$ level is involved in the $S_2 \longrightarrow S_1$ transition, and thus, the energy scheme on the Figure 3.20.(a) is correct. Moreover, the presence of the negative signal in the state S_1 suggests that the depopulation of the S_2 level occurs to highest vibrational levels on the vibrational ladder of electronic state S_1. Still, as mentioned before, it is not obvious if vibrational levels of S_1 are populated from the bottom vibrational levels of the S_2 state or rather from some vibrationally excited levels. Therefore, it cannot yet be stated whether only four vibrational levels are involved in the intramolecular vibrational relaxation of the S_1 state.

Absence of negative signal for the S_2 state can be explained by the fact that vibrational levels exist beyond the level populated by the actinic pump. Another explanation, however, can be that this negative signal is hidden due to limited time resolution of the setup.

Table 3.1: The values of parameters obtained from Model 1 fitting.

Γ_2 [fs]	110 ± 1
Γ_c [fs]	313 ± 27
Γ_b [fs]	388 ± 38
Γ_a [fs]	624 ± 141
Γ_g [fs]	$(31.4 \pm 6.3) \cdot 10^3$
γ_{cb} [cm^{-1}]	1751.7 ± 6.6
γ_{ba} [cm^{-1}]	1760.0 ± 3.9
γ_{ag} [cm^{-1}]	1768.25 ± 0.88
D_{ag}	1 (fixed)
D_{ba}/D_{ag}	2.03 ± 0.82
D_{cb}/D_{ag}	3.06 ± 0.12

No complete repopulation of the ground state occurs within experimental time. The electron transfer reaction to the solvent was proposed as the mechanism responsible for similar behavior observed in β-carotene in chloroform [190] another possibility of significant triplet state population directly from S_2 was also proposed recently [106, 191]. However, further studies on this particular subject have to be performed to reveal the nature of this phenomenon. The destruction of the sample is unlike as no dependence of this phenomenon on the actinic or Raman pump power was observed. In any case, a general behavior of the ground state repopulation due to internal conversion, has been successfully reproduced, as can be seen in Figure 3.41.

3.9 Conclusion

Herewith a construction of a Time-Resolved Femtosecond Stimulated Raman Scattering setup and measurement in trans-β-apo-8′-carotenal were described. The results of experiment were analyzed by calculating the FSRS

time resolved signal on the basis of the quantum mechanical approach, using the formalism of projection operators. By including the populations of vibrational states as dynamical variables, the phenomenon of the transient vibrational population inversion was described. It was shown that the predictions of numerical models agree well with the experimental results, demonstrating that the decaying vibrational population inversion leads to the transition from Raman losses to Raman gain on the Stokes side of TR-FSRS spectra. Furthermore, the mechanism of the observed Raman line frequency shift was explained by combination of Raman loss to Raman gain transition and difference in vibrational levels' separation energy. The agreement of the modeling and the experimental results suggests that no additional "dark" electronic state is involved in the $S_2 \longrightarrow S_1$ transition in trans-β-apo-8′-carotenal molecule.

Chapter 4

Conclusions

In the present thesis coupling of light with medium vibrations was used for studying complex processes occurring in diamond crystal and carotenal molecule. In both cases the modification of short pulse intensities due to Impulsive Stimulated Raman Scattering within the medium was observed. In the first case, the medium was subjected to highly intensive off-resonance pulse, in the second, the measurements were carried on during the relaxation after electronic excitation of the sample.

The first experiment was the generation of supercontinuum in a bulk diamond crystal. The main objective of those measurements was to confirm the presence of features characteristic for Stimulated Raman Scattering in the supercontinuum spectra, and, thus, to asses the involvement of SRS in supercontinuum generation process. The experiment was performed for wide range of input energies. Spectra of supercontinua, only slightly affected by self-phase modulation, as well as spectra of supercontinua, generated just below the multiple filamentation threshold, where presented. For energies

above 17 μJ a small peak shifted by around 1332 cm^{-1} (the frequency of diamond lattice vibration) from the pulse central frequency can be observed. This peak is attributed to SRS. In the present thesis, supercontinuum generation process was described by means of the nonlinear envelope equation. The experimental results, together with presence of the SRS peak, were well reproduced by the model.

The SRS peak can be observed in the spectrum of supercontinuum generated in diamond, it is, however, weak. Thus a conclusion is drawn that for other media, like for example fused silica, where the Raman gain is orders of magnitude smaller, the SRS has little meaning in the process of white light generation. This confirms the validity of assumption (made by many authors [40, 43–46]) that it can be neglected in simulations of supercontinuum generation in those media.

The process of white light generation in complex media involves many phenomena. A few of them can cause similar effects, for example, both 5th order nonlinearity (the self-phase-modulation or self-focusing saturation) and photoionization cause defocusing of the beam. On the other side, both, self-phase modulation and interaction with the free-carriers generated by photoionization cause spectrum broadening. Therefore, as one of many phenomena – the Stimulated Raman Scattering – can be neglected, more effort can be made on the studies to distinguish importance of the remaining processes.

Additional results from the simulation of the supercontinuum generation process is that, while photoionization is most important, the 5th order nonlinearity can also play significant role in defocusing of the beam.

The blue side of the supercontinuum generated in diamond is limited to around 600 nm. This parameter restrains the applicability of diamond as a supercontinuum source in spectroscopy as broader spectrum can be generated in materials like sapphire, fused silica, CaF_2 and LiF. However, the possibility of using diamond supercontinuum in various applications, like spectroscopy, optical coherent tomography or carrier-envelope phase stabilization, remains unexamined. Moreover, no studies of supercontinuum generation in diamond were performed in the infrared region and with other sources of pulses like femtosecond laser oscillators. Thus, further studies on the applicability of the material are possible.

The second experiment was the Time-Resolved Femtosecond Stimulated Raman Scattering (TR-FSRS) studies of trans-β-apo-8′-carotenal molecule. A TR-FSRS setup was constructed by the author for purpose of this thesis. The time resolution of the setup is better than 100 fs an the frequency resolution is about 25 cm^{-1}. The trans-β-apo-8′-carotenal molecule was excited electronically to the S_2 state and it's relaxation to the ground state was observed through measurements of FSRS spectra of the C=C symmetrical stretching vibration. Due to vibronic coupling the frequency of C=C symmetrical stretching vibration differs significantly in different electronic states. The line corresponding to S_2 state decays within 120 fs after excitation, then a long living line at frequency corresponding to the optically forbidden S_1 state appears. During the first 500 fs this line is negative, which is attributed to the transient vibrational inversion of population in S_1 electronic level. Later the line becomes positive and then decays with the lifetime of S_1 level. At the same time the frequency of the line up-shifts.

The results of experiment were analyzed by comparison with the FSRS time resolved signal calculated on the basis of the quantum mechanical approach, using the formalism of projection operators. It was shown that the predictions of numerical models agree well with the experimental results.

The relaxation pathways of carotenoids is still a topic of discussion. The involvement of the so called dark state, with symmetry $1B_u^-$ was proposed by some authors [100, 125, 126, 131, 134, 136–139] and criticized by others [105, 112, 116–118, 120–122, 127, 129, 130]. In the present work, no influence of dark state has been detected. The signal obtained experimentally was explained by a model where apart of electronic states S_2 and S_0 a set of vibratioally excited sublevels of electronic state S_1 was used. It was shown, that the decaying vibrational population inversion leads to the transition from Raman losses to Raman gain on the Stokes side of TR-FSRS spectra. Additionally, the difference in energy separation of subsequent vibrational levels combined with Raman loss to Raman gain transition explained the line frequency shift. By fitting the result of modeling to experimental data decay rates of electronic states and vibrational sublevels were resolved. The results of my research, presented in this thesis, have been published [52, 192].

Appendices

Appendix A

Parallel Implicit Ordinary Differential Equations Solver

A simplest definition of stiffness, sufficient for purposes of the present thesis is as follows [88]:

A set of ordinary differential equations is said to be stiff when certain implicit methods perform their solution "better" than explicit ones.

The common symptom of equations stiffening is the fact that, to maintain the accuracy of the solution the explicit solver's marching step has to be reduced to unreasonably small size. On the other hand, in such cases, implicit methods often can be used for solution of such problems with high accuracy and a reasonably large step size.

For the ordinary differential equation defined as:

$$\frac{d\vec{y}}{dt} = \vec{f}(\vec{y}, t) \tag{A.1}$$

c_k	a_{kj}
	b_j

Table A.1: Butcher tableau for Runge-Kutta method, c_k are the nodes, b_j are the weights and a_kj are the elements of Runge-Kutta matrix.

1	1
	1

Table A.2: Butcher tableau for implicite Euler method.

the explicit solver at each step calculates the function $\vec{f}$ with use of solution from the previous steps and uses it to compute the new solution. For example, if the explicit Euler method is used:

$$y(t_{i+1}) = y(t_i) + \Delta t f(y(t_i), t_i) \tag{A.2}$$

here $y(t_{i+1})$ is the new solution at time $t_{i+1} = t_i + \Delta t$ and $y(t_i)$ is the calculated earlier solution at t_i, Δt is the step size. On the other hand, the implicit solver uses the value of $\vec{f}$ calculated for the next step. For example, if the implicit Euler method is used:

$$y(t_{i+1}) = y(t_i) + \Delta t f(y(t_{i+1}), t_{i+1}). \tag{A.3}$$

Unlike in the first case, this second equation is a potentially nonlinear equation for $y(t_{i+1})$ which has to be solved (for example with compute-intensive Newton iterative method). Therefore, for non-stiff cases explicit methods are usually faster and thus preferable.

In the present thesis two problems described by the sets of ordinary differential equations (ODE) which were found to be stiff were encountered. The

$\frac{4-\sqrt{6}}{10}$	$\frac{88-7\sqrt{6}}{360}$	$\frac{296-169\sqrt{6}}{1800}$	$\frac{-2+3\sqrt{6}}{225}$
$\frac{4+\sqrt{6}}{10}$	$\frac{296+169\sqrt{6}}{1800}$	$\frac{88+7\sqrt{6}}{360}$	$\frac{-2-3\sqrt{6}}{225}$
1	$\frac{16-\sqrt{6}}{36}$	$\frac{16+\sqrt{6}}{1800}$	$\frac{1}{9}$
	$\frac{16-\sqrt{6}}{36}$	$\frac{16+\sqrt{6}}{1800}$	$\frac{1}{9}$

Table A.3: Butcher tableau for three stage Radau IIA implicit method of the fifth order [88].

first problem is the equation of current density in the supercontinuum generation model (Eq. 2.37. in section 2.3.5.), the second is the set of Heisenberg-Langevin equations of motion for trans-β-apo-8′-carotenal molecule (see section 3.6.). In both cases the ODE sets can be solved in parallel for different parameters set. In case of current density, the photoionization rate on the right hand side of equation depends on the amplitude of electric field which is different for every radial coordinate. And the Heisenberg-Langevin equations have to be solved for different pump-probe delays to obtain a single TR-FSRS signal.

Modern graphical cards are specialized in parallel computation. By use of these graphical processing units (GPU) action can be perform simultaneously on the set of data as long as this action is the same for each data entry [193]. This is not a limitation in the present case – the procedure of ODE solving is identical for each value of the parameter. Thus, the parallel ODE solver was implemented for GPU[1].

The scheme proposed by E. Hairer and G. Wanner [88] for implicit Runge-Kutta method implementation was applied. The new solution $\vec{y}_{i+1}$ is calcu-

[1]It is possible to use explicit ODE solving methods in parallel on GPU with use of odeint [194] library and one of a few GPU interface library [195, 196].

lated from previous $\vec{y}_i$ by:

$$\vec{y}_{i+1} = \vec{y}_i + \sum_{j=1}^{s} d_j \vec{z}_j, \tag{A.4}$$

where d_j are constants, s is the number of method stages and $\vec{z}_j$ are calculated as solution of algebraic equation set:

$$\vec{z}_j = \Delta t \sum_{k=1}^{s} a_{jk} f(x_j + c_k \Delta t, \vec{y}_i + \vec{z}_k), \tag{A.5}$$

where a_{jk} are the elements of Runge-Kutta matrix, c_k are Runge-Kutta method nodes. The three stage Radau IIA fifth order implicit Runge-Kutta method and implicit Euler method of second order were implemented. The values of elements of Runge-Kutta matrix, nodes and weights for these methods are presented in Butcher [197] tables A.3. and A.2, the construction of Butcher table is presented in table A.1. The Eq. A.5. is solved with a simplified Newton iteration, which uses the Jacobian matrix of the system [88]. A constant of 10 Newtnonian iteration are performed per step. There is no step-size control implemented and the positions (x_i) at which the solution is given are proposed by the user.

The user has to supply the system function `SystemFunction` and Jacobian `SystemJacobian` of the system in the C++ language:

```
#include "arch_settings.h"

template<typename T> DEVICE void SystemFunction(
 T *pDerivatives,
 T *pPreviousSolution,
 T fCoordinate,
 const T *pParams,
 const T *pConstParams)
```

```
{
        ...
}

template<typename T> DEVICE void SystemJacobian(
 T *pJacobian,
 T *pPreviousSolution,
 T fCoordinate,
 const T *pParams,
 const T *pConstParams)
{
        ...
}
```

here `T` is the floating point number type (`float` or `double`), `pDerivatives` and `pJacobian` points to memory area where calculated derivatives and elements of Jacobian should be placed, `pPreviousSolution` points to the solution from previous iteration, `fCoordinate` is the current value of time coordinate, `pParams` points at the memory containing parameter values specific for current instance, `pConstParams` points at the memory containing parameter values common for all instance, the `"arch_settings.h"` file contains required definitions and CUDA inclusions (`DEVICE` key word). The file containing `SystemFunction` and `SystemJacobian` definitions has to be included in CUDA C file of the following form:

```
#define FLOAT double

#include "harmonic_oscillator.hpp"
#include "RadauIIA.hpp"
#include "parallel_solver.hpp"
```

here, example `"harmonic_oscillator.hpp"` file is used, it contains definitions of `SystemFunction` and `SystemJacobian` for simple harmonic oscillator, by setting the `FLOAT` to `float` or `double` the precision of calculations can be chosen, the method of solution can be chosen by inclusion of `"RadauIIA.hpp"` for Radau IIA method or `"implicite_euler.hpp"` for implicit Euler method.

The CUDA C file can be either linked together wit other code, or can be compiled into a CUDA kernel [193] (Parallel Thread Execution "ptx" file) and used from other software, like MATLAB. In both cases the point of entry of the external code is through the following function:

```
GLOBAL void solveAllOde(
 FLOAT *pSolution,
 const FLOAT *pTimes,
 int iTSize,
 const FLOAT *pInitialCondition,
 int iProblemDimension,
 const FLOAT *pParams,
 int iParamsNumber,
 int iParamsVariantsNumber,
 const FLOAT *pConstParams,
 FLOAT *pBuffer,
 int iBufferUnitSize)
```

where `iProblemDimension` is the number of differential equations in the ODE set, `iParamsVariantsNumber` is the number of variants of parameter or initial condition values, `iParamsNumber` is the number of variable parameters per variant, `iTSize` is the number of time points at which the solution should be computed, `pSolution` points to the memory area where the solution of all the ODE sets for all parameter values and initial conditions will be placed (it should have a size of `iProblemDimension` × `iParamsVariantsNumber` × `iTSize`), `pTimes` points to values of time at which the solution will be computed, `pInitialCondition` points at values of initial conditions (size is `iProblemDimension` × `iTSize`), `pParams` points at values of parameters for all variants (size is `iParamsNumber` × `iParamsVariantsNumber`), `pConstParams` points to the memory containing parameters common for all variants, `pBuffor` is the method specific calculation buffer of size `iBufferUnitSize` . The size of the buffer depend on `iProblemDimension` and can be obtaine by use of macrodefinitions `RADAUIIA_BUFFOR_SIZE(iProblemDimension)` and

`IMPLICITE_EULER_BUFFOR_SIZE(iProblemDimension)` for Radau and Euler methods respectively. The `solveAllOde` function distributes the parameter values, initial conditions and memory buffers to particular instances of ODE solvers. The code of the library has been published on the internet [198].

Appendix B

Derivation of equations for a two vibrational level system

Herewith details on derivation of equations describing the dynamics of a system with two real vibrational levels 0 and 1 in some electronic state and a set of virtual levels m is considered.

B.1 Creation and annihilation operators for fermions

Time dependent operators ${b_n}^\dagger$ and b_n can be interpreted as creation and annihilation operators of an electronic state of the molecule [183] Those operators obey following commutation relations:

$$b_k^\dagger b_l + b_l b_k^\dagger = \delta_{kl} \tag{B.1}$$

$$b_k b_m + b_m b_k = 0 \tag{B.2}$$

$$b_k^\dagger b_m^\dagger + b_m^\dagger b_k^\dagger = 0 \tag{B.3}$$

B.2 Heisenberg-Langevin equations

The Heisenberg-Langevin equations for the system described by Hamiltonian Eq. 3.4 will now be derived. Starting with equation for evolution of $b_0^\dagger b_0$:

$$d_t b_0^\dagger b_0 = \frac{i}{\hbar}[H, b_0^\dagger b_0] = \frac{i}{\hbar}\left([H_0, b_0^\dagger b_0] + [H_{int}, b_0^\dagger b_0] + [H_B, b_0^\dagger b_0]\right), \tag{B.4}$$

the consecutive contributions will be considered separately.

First:

$$\begin{aligned}
[H_0, b_0^\dagger b_0] &= \sum_n W_n \left(b_n^\dagger b_n b_0^\dagger b_0 - b_0^\dagger b_0 b_n^\dagger b_n\right) \\
&= \sum_n W_n \left(b_n^\dagger \delta_{0n} b_0 - b_n^\dagger b_0^\dagger b_n b_0 - b_0^\dagger \delta_{0n} b_n + b_0^\dagger b_n^\dagger b_0 b_n\right) \\
&= 0,
\end{aligned} \tag{B.5}$$

where the commutation relations B.1. was used in the first line and then the relation: $b_0^\dagger b_n^\dagger b_0 b_n = b_n^\dagger b_0^\dagger b_n b_0$ (derived from B.2. and B.3) was used in the second line.

Second[1]:

$$
\begin{aligned}
-[\mu E, b_0^\dagger b_0] &= -E \sum_{n \neq m} \mu_{nm} \left(b_n^\dagger b_m b_0^\dagger b_0 - b_0^\dagger b_0 b_n^\dagger b_m \right) \\
&= -E \sum_{n \neq m} \mu_{nm} \left(b_n^\dagger \delta_{0m} b_0 - b_n^\dagger b_0^\dagger b_m b_0 - b_0^\dagger \delta_{0n} b_m + b_0^\dagger b_n^\dagger b_0 b_m \right),
\end{aligned}
\tag{B.6}
$$

again $b_n^\dagger b_0^\dagger b_m b_0 = b_0^\dagger b_n^\dagger b_0 b_m$, and thus:

$$
\begin{aligned}
-[\mu E, b_0^\dagger b_0] &= -E \sum_{n \neq m} \mu_{nm} \left(b_n^\dagger \delta_{0m} b_0 - b_0^\dagger \delta_{0n} b_m \right) \\
&= -E \left(\sum_{n \neq 0} \mu_{n0} b_n^\dagger b_0 - \sum_{m \neq 0} \mu_{0m} b_0^\dagger b_m \right) \\
&= -E \sum_{n \neq 0} \left(\mu_{n0} b_n^\dagger b_0 - \mu_{0n} b_0^\dagger b_n \right).
\end{aligned}
\tag{B.7}
$$

Finally after inserting Eq. B.5, B.7. and 3.13. into B.4:

$$
d_t b_0^\dagger b_0 = \Gamma_1 b_1^\dagger b_1 - \Gamma_0 b_0^\dagger b_0 - \frac{i}{\hbar} E \sum_{n \neq 0} \left(\mu_{n0} b_n^\dagger b_0 - \mu_{0n} b_0^\dagger b_n \right) \tag{B.8}
$$

In the same way:

$$
d_t b_1^\dagger b_1 = -\Gamma_1 b_1^\dagger b_1 - \frac{i}{\hbar} E \sum_{n \neq 1} \left(\mu_{n1} b_n^\dagger b_1 - \mu_{1n} b_1^\dagger b_n \right) \tag{B.9}
$$

[1]Note that $E = E_0 e^{i\omega t} + E_0^* e^{-i\omega t}$

and:

$$d_t b_m^\dagger b_m = -\Gamma_m b_m^\dagger b_m - \frac{i}{\hbar} E \sum_{n \neq m} \left(\mu_{nm} b_n^\dagger b_m - \mu_{mn} b_m^\dagger b_n \right), \tag{B.10}$$

where the virtual state m decays instantaneously with $\tau_m \to 0$ ($\Gamma_m = \frac{1}{\tau_m} \to \infty$), therefore the last equation becomes:

$$d_t b_m^\dagger b_m \to -\infty - \ldots, \tag{B.11}$$

$b_m^\dagger b_m$ has to be greater or equal to zero, thus as its the derivative becomes infinite $b_m^\dagger b_m(t) = 0$ at all times.

The evolution of the mixed operators $b_n^\dagger b_l$, where $n \neq l$, can be derived in a similar way, starting from:

$$d_t b_n^\dagger b_l = \frac{i}{\hbar} \left([H_0, b_n^\dagger b_l] + [H_{int}, b_n^\dagger b_l] + [H_B, b_n^\dagger b_l] \right). \tag{B.12}$$

Here, first:

$$\begin{aligned} [H_0, b_n^\dagger b_l] &= \sum_k W_k \left(b_k^\dagger b_k b_n^\dagger b_l - b_n^\dagger b_l b_k^\dagger b_k \right) \\ &= \sum_k W_k \left(b_k^\dagger \delta_{kn} b_l - b_k^\dagger b_n^\dagger b_k b_l - b_n^\dagger \delta_{lk} b_k + b_n^\dagger b_k^\dagger b_l b_k \right) \\ &= (W_n - W_l) b_n^\dagger b_l, \end{aligned} \tag{B.13}$$

therefore, for $n, l = 0, 1$ and m:

$$\begin{aligned}
&[H_0, b_0^\dagger b_1] = (W_0 - W_1) b_0^\dagger b_1, \quad [H_0, b_1^\dagger b_0] = (W_1 - W_0) b_1^\dagger b_0, \\
&[H_0, b_0^\dagger b_m] = (W_0 - W_m) b_0^\dagger b_m, \quad [H_0, b_m^\dagger b_0] = (W_m - W_0) b_m^\dagger b_0, \\
&[H_0, b_m^\dagger b_1] = (W_m - W_1) b_m^\dagger b_1, \quad [H_0, b_1^\dagger b_m] = (W_1 - W_m) b_1^\dagger b_m.
\end{aligned} \tag{B.14}$$

Second:

$$\begin{aligned}
-[\mu E, b_n^\dagger b_l] &= -E \sum_{k \neq j} \mu_{kj} \left(b_k^\dagger b_j b_n^\dagger b_l - b_n^\dagger b_l b_k^\dagger b_j \right) \\
&= -E \sum_{k \neq j} \mu_{kj} \left(b_k^\dagger \delta_{jn} b_l - b_k^\dagger b_n^\dagger b_j b_l - b_n^\dagger \delta_{lk} b_j + b_n^\dagger b_k^\dagger b_l b_j \right) \\
&= -E \left(\sum_{k \neq n} \mu_{kn} b_k^\dagger b_l - \sum_{j \neq l} \mu_{lj} b_n^\dagger b_j \right),
\end{aligned} \tag{B.15}$$

and again for $n, l = 0, 1$ and m:

$$\begin{aligned}
-[\mu E, b_0^\dagger b_1] &= -E \left(\sum_{k \neq 0} \mu_{k0} b_k^\dagger b_1 - \sum_{j \neq 1} \mu_{1j} b_0^\dagger b_j \right) \\
&= -E\mu_{10} \left(b_1^\dagger b_1 - b_0^\dagger b_0 \right) - E \sum_m \left(\mu_{m0} b_m^\dagger b_1 - \mu_{1m} b_0^\dagger b_m \right), \\
-[\mu E, b_1^\dagger b_0] &= -E\mu_{01} \left(b_0^\dagger b_0 - b_1^\dagger b_1 \right) + E \sum_m \left(\mu_{m1} b_m^\dagger b_0 - \mu_{0m} b_1^\dagger b_m \right), \\
-[\mu E, b_0^\dagger b_m] &= -E \left[\mu_{m0} \left(b_m^\dagger b_m - b_0^\dagger b_0 \right) + \mu_{10} b_1^\dagger b_m - \mu_{m1} b_0^\dagger b_1 \right], \\
-[\mu E, b_m^\dagger b_0] &= -E \left[\mu_{0m} \left(b_0^\dagger b_0 - b_m^\dagger b_m \right) + \mu_{1m} b_1^\dagger b_0 - \mu_{01} b_m^\dagger b_1 \right], \\
-[\mu E, b_1^\dagger b_m] &= -E \left[\mu_{m1} \left(b_m^\dagger b_m - b_1^\dagger b_1 \right) + \mu_{01} b_0^\dagger b_m - \mu_{m0} b_1^\dagger b_0 \right], \\
-[\mu E, b_m^\dagger b_1] &= -E \left[\mu_{1m} \left(b_1^\dagger b_1 - b_m^\dagger b_m \right) + \mu_{0m} b_0^\dagger b_1 - \mu_{10} b_m^\dagger b_0 \right],
\end{aligned} \tag{B.16}$$

where the first term corresponds to single photon absorption and the sum corresponds to stimulated processes occurring with involvement of the virtual state,

By merging equations B.14., B.16 and 3.15 a set of equations is obtained:

$$\begin{aligned}
d_t b_0^\dagger b_1 =& -\gamma_{01} b_0^\dagger b_1 - i\omega_{10} b_0^\dagger b_1 \\
& - \frac{i}{\hbar}\left(E\mu_{10}\left(b_1^\dagger b_1 - b_0^\dagger b_0 \right) + E\sum_m \left(\mu_{m0} b_m^\dagger b_1 - \mu_{1m} b_0^\dagger b_m \right) \right), \\
d_t b_1^\dagger b_0 =& -\gamma_{01} b_1^\dagger b_0 + i\omega_{10} b_1^\dagger b_0 \\
& - \frac{i}{\hbar}\left(E\mu_{01}\left(b_0^\dagger b_0 - b_1^\dagger b_1 \right) + E\sum_m \left(\mu_{m1} b_m^\dagger b_0 - \mu_{0m} b_1^\dagger b_m \right) \right), \\
d_t b_0^\dagger b_m =& -i\omega_{m0} b_0^\dagger b_m - \frac{i}{\hbar} E\left[\mu_{m0}\left(b_m^\dagger b_m - b_0^\dagger b_0 \right) + \mu_{10} b_1^\dagger b_m - \mu_{m1} b_0^\dagger b_1 \right], \\
d_t b_m^\dagger b_0 =& i\omega_{m0} b_m^\dagger b_0 - \frac{i}{\hbar} E\left[\mu_{0m}\left(b_0^\dagger b_0 - b_m^\dagger b_m \right) + \mu_{1m} b_1^\dagger b_0 - \mu_{01} b_m^\dagger b_1 \right], \\
d_t b_1^\dagger b_m =& -i\omega_{m1} b_1^\dagger b_m - \frac{i}{\hbar} E\left[\mu_{m1}\left(b_m^\dagger b_m - b_1^\dagger b_1 \right) + \mu_{01} b_0^\dagger b_m - \mu_{m0} b_1^\dagger b_0 \right], \\
d_t b_m^\dagger b_1 =& i\omega_{m1} b_m^\dagger b_1 - \frac{i}{\hbar} E\left[\mu_{1m}\left(b_1^\dagger b_1 - b_m^\dagger b_m \right) + \mu_{0m} b_0^\dagger b_1 - \mu_{10} b_m^\dagger b_0 \right],
\end{aligned} \tag{B.17}$$

or if a slowly varying amplitudes for the mix operators $\left\langle b_n^\dagger b_l \right\rangle = Q_{nl} e^{i\omega_{nl} t}$ and populations $\left\langle b_l^\dagger b_l \right\rangle = n_l$, where $\langle . \rangle$ denotes average over ensemble, are used:

$$d_t n_0 = \Gamma_1 n_1 - \Gamma_0 n_0 - \frac{i}{\hbar} E \sum_{n\neq 0} \left(\mu_{n0} Q_{n0} e^{i\omega_{n0} t} - \mu_{0n} Q_{0n} e^{-i\omega_{n0} t} \right), \tag{B.18}$$

$$d_t n_1 = -\Gamma_1 n_1 - \frac{i}{\hbar} E \sum_{n\neq 1} \left(\mu_{n1} Q_{n1} e^{i\omega_{n1} t} - \mu_{1n} Q_{1n} e^{-i\omega_{n1} t} \right), \tag{B.19}$$

$$d_t Q_{01} = -\gamma_{01} Q_{01} - \frac{i}{\hbar} E e^{i\omega_{10}t} \left[\mu_{10}\left(n_1 - n_0\right) + \sum_m \left(\mu_{m0} Q_{m1} e^{i\omega_{m1}t} - \mu_{1m} Q_{0m} e^{-i\omega_{m0}t}\right)\right], \tag{B.20}$$

$$d_t Q_{10} = -\gamma_{01} Q_{10} + \frac{i}{\hbar} E e^{-i\omega_{10}t} \left[\mu_{01}\left(n_1 - n_0\right) + \sum_m \left(\mu_{0m} Q_{1m} e^{-i\omega_{m1}t} - \mu_{m1} Q_{m0} e^{i\omega_{m0}t}\right)\right], \tag{B.21}$$

$$d_t Q_{0m} = -\frac{i}{\hbar} E e^{i\omega_{m0}t} \left[\mu_{m0}\left(n_m - n_0\right) + \mu_{10} Q_{1m} e^{-i\omega_{m1}t} - \mu_{m1} Q_{01} e^{-i\omega_{10}t}\right], \tag{B.22}$$

$$d_t Q_{m0} = \frac{i}{\hbar} E e^{-i\omega_{m0}t} \left[\mu_{0m}\left(n_m - n_0\right) + \mu_{01} Q_{m1} e^{i\omega_{m1}t} - \mu_{1m} Q_{10} e^{i\omega_{10}t}\right], \tag{B.23}$$

$$d_t Q_{1m} = -\frac{i}{\hbar} E e^{i\omega_{m1}t} \left[\mu_{m1}\left(n_m - n_1\right) + \mu_{01} Q_{0m} e^{-i\omega_{m0}t} - \mu_{m0} Q_{10} e^{i\omega_{10}t}\right], \tag{B.24}$$

$$d_t Q_{m1} = \frac{i}{\hbar} E e^{-i\omega_{m1}t} \left[\mu_{1m}\left(n_m - n_1\right) + \mu_{10} Q_{m0} e^{i\omega_{m0}t} - \mu_{0m} Q_{01} e^{-i\omega_{10}t}\right], \tag{B.25}$$

here $n = 0, 1, m$. As $Q_{kl} = Q_{lk}^{\dagger}$, the relation: $d_t Q_{kl} = (d_t Q_{lk})^{\dagger}$ is also valid, which is visible in above equations, it is therefore enough to consider half of the equations for vibrational amplitudes. If the electric field is represented as a plane wave:

$$E = E_L e^{i\omega_L t} + E_L^* e^{-i\omega_L t} + E_S e^{i\omega_S t} + E_S^* e^{-i\omega_S t}, \tag{B.26}$$

where E_L and E_S are constant or slowly varying amplitudes of Raman pump and probe, respectively, equations B.22, B.23, B.24. and B.25. can be integrated.

Integration of equation B.22 after setting $n_m = 0$, gives:

$$
\begin{aligned}
Q_{0m}(t) = Q_{0m}(0) &+ \frac{1}{\hbar}\mu_{m0}n_0\Big(\\
&\frac{E_L e^{i(\omega_{m0}+\omega_L)t}}{\omega_{m0}+\omega_L} - \frac{E_L}{\omega_{m0}+\omega_L} \\
&+ \frac{E_L^* e^{i(\omega_{m0}-\omega_L)t}}{\omega_{m0}-\omega_L} - \frac{E_L^*}{\omega_{m0}-\omega_L} \\
&+ \frac{E_S e^{i(\omega_{m0}+\omega_S)t}}{\omega_{m0}+\omega_S} - \frac{E_L}{\omega_{m0}+\omega_S} \\
&+ \frac{E_S^* e^{i(\omega_{m0}-\omega_S)t}}{\omega_{m0}-\omega_S} - \frac{E_L^*}{\omega_{m0}-\omega_S}\Big) \\
&- \frac{1}{\hbar}\mu_{10}Q_{1m}\Big(\\
&\frac{E_L e^{i(\omega_{m0}-\omega_{m1}+\omega_L)t}}{\omega_{m0}-\omega_{m1}+\omega_L} - \frac{E_L}{\omega_{m0}-\omega_{m1}+\omega_L} \\
&+ \frac{E_L^* e^{i(\omega_{m0}-\omega_{m1}-\omega_L)t}}{\omega_{m0}-\omega_{m1}-\omega_L} - \frac{E_L^*}{\omega_{m0}-\omega_{m1}-\omega_L} \\
&+ \frac{E_S e^{i(\omega_{m0}-\omega_{m1}+\omega_S)t}}{\omega_{m0}-\omega_{m1}+\omega_S} - \frac{E_S}{\omega_{m0}-\omega_{m1}+\omega_S} \\
&+ \frac{E_S^* e^{i(\omega_{m0}-\omega_{m1}-\omega_S)t}}{\omega_{m0}-\omega_{m1}-\omega_S} - \frac{E_S^*}{\omega_{m0}-\omega_{m1}-\omega_S}\Big) \\
&+ \frac{1}{\hbar}\mu_{m1}Q_{01}\Big(\\
&\frac{E_L e^{i(\omega_{m0}-\omega_{10}+\omega_L)t}}{\omega_{m0}-\omega_{10}+\omega_L} - \frac{E_L}{\omega_{m0}-\omega_{10}+\omega_L} \\
&+ \frac{E_L^* e^{i(\omega_{m0}-\omega_{10}-\omega_L)t}}{\omega_{m0}-\omega_{10}-\omega_L} - \frac{E_L^*}{\omega_{m0}-\omega_{10}-\omega_L} \\
&+ \frac{E_S e^{i(\omega_{m0}-\omega_{10}+\omega_S)t}}{\omega_{m0}-\omega_{10}+\omega_S} - \frac{E_S}{\omega_{m0}-\omega_{10}+\omega_S} \\
&+ \frac{E_S^* e^{i(\omega_{m0}-\omega_{10}-\omega_S)t}}{\omega_{m0}-\omega_{10}-\omega_S} - \frac{E_S^*}{\omega_{m0}-\omega_{10}-\omega_S}\Big)
\end{aligned}
\tag{B.27}
$$

Integration of equation B.23 after setting $n_m = 0$, gives:

$$
\begin{aligned}
Q_{m0}(t) = Q_{m0}(0) &+ \frac{1}{\hbar}\mu_{0m}n_0\Big(\\
&\frac{E_L e^{-i(\omega_{m0}-\omega_L)t}}{\omega_{m0}-\omega_L} - \frac{E_L}{\omega_{m0}-\omega_L} \\
&+ \frac{E_L^* e^{-i(\omega_{m0}+\omega_L)t}}{\omega_{m0}+\omega_L} - \frac{E_L^*}{\omega_{m0}+\omega_L} \\
&+ \frac{E_S e^{-i(\omega_{m0}-\omega_S)t}}{\omega_{m0}-\omega_S} - \frac{E_L}{\omega_{m0}-\omega_S} \\
&+ \frac{E_S^* e^{-i(\omega_{m0}+\omega_S)t}}{\omega_{m0}+\omega_S} - \frac{E_L^*}{\omega_{m0}+\omega_S}\Big) \\
&- \frac{1}{\hbar}\mu_{01}Q_{m1}\Big(\\
&\frac{E_L e^{-i(\omega_{m0}-\omega_{m1}-\omega_L)t}}{\omega_{m0}-\omega_{m1}-\omega_L} - \frac{E_L}{\omega_{m0}-\omega_{m1}-\omega_L} \\
&+ \frac{E_L^* e^{-i(\omega_{m0}-\omega_{m1}+\omega_L)t}}{\omega_{m0}-\omega_{m1}+\omega_L} - \frac{E_L^*}{\omega_{m0}-\omega_{m1}+\omega_L} \\
&+ \frac{E_S e^{-i(\omega_{m0}-\omega_{m1}-\omega_S)t}}{\omega_{m0}-\omega_{m1}-\omega_S} - \frac{E_S}{\omega_{m0}-\omega_{m1}-\omega_S} \\
&+ \frac{E_S^* e^{-i(\omega_{m0}-\omega_{m1}+\omega_S)t}}{\omega_{m0}-\omega_{m1}+\omega_S} - \frac{E_S^*}{\omega_{m0}-\omega_{m1}+\omega_S}\Big) \\
&+ \frac{1}{\hbar}\mu_{1m}Q_{10}\Big(\\
&\frac{E_L e^{-i(\omega_{m0}-\omega_{10}-\omega_L)t}}{\omega_{m0}-\omega_{10}-\omega_L} - \frac{E_L}{\omega_{m0}-\omega_{10}-\omega_L} \\
&+ \frac{E_L^* e^{-i(\omega_{m0}-\omega_{10}+\omega_L)t}}{\omega_{m0}-\omega_{10}+\omega_L} - \frac{E_L^*}{\omega_{m0}-\omega_{10}+\omega_L} \\
&+ \frac{E_S e^{-i(\omega_{m0}-\omega_{10}-\omega_S)t}}{\omega_{m0}-\omega_{10}-\omega_S} - \frac{E_S}{\omega_{m0}-\omega_{10}-\omega_S} \\
&+ \frac{E_S^* e^{-i(\omega_{m0}-\omega_{10}+\omega_S)t}}{\omega_{m0}-\omega_{10}+\omega_S} - \frac{E_S^*}{\omega_{m0}-\omega_{10}+\omega_S}\Big)
\end{aligned}
\tag{B.28}
$$

Integration of equation B.24 after setting $n_m = 0$, gives:

$$
\begin{aligned}
Q_{1m}(t) = Q_{1m}(0) &+ \frac{1}{\hbar}\mu_{m1}n_1\Big(\\
&\frac{E_L e^{i(\omega_{m1}+\omega_L)t}}{\omega_{m1}+\omega_L} - \frac{E_L}{\omega_{m1}+\omega_L} \\
&+ \frac{E_L^* e^{i(\omega_{m1}-\omega_L)t}}{\omega_{m1}-\omega_L} - \frac{E_L^*}{\omega_{m1}-\omega_L} \\
&+ \frac{E_S e^{i(\omega_{m1}+\omega_S)t}}{\omega_{m1}+\omega_S} - \frac{E_L}{\omega_{m1}+\omega_S} \\
&+ \frac{E_S^* e^{i(\omega_{m1}-\omega_S)t}}{\omega_{m1}-\omega_S} - \frac{E_L^*}{\omega_{m1}-\omega_S}\Big) \\
&- \frac{1}{\hbar}\mu_{01}Q_{0m}\Big(\\
&\frac{E_L e^{i(\omega_{m1}-\omega_{m0}+\omega_L)t}}{\omega_{m1}-\omega_{m0}+\omega_L} - \frac{E_L}{\omega_{m1}-\omega_{m0}+\omega_L} \\
&+ \frac{E_L^* e^{i(\omega_{m1}-\omega_{m0}-\omega_L)t}}{\omega_{m1}-\omega_{m0}-\omega_L} - \frac{E_L^*}{\omega_{m1}-\omega_{m0}-\omega_L} \\
&+ \frac{E_S e^{i(\omega_{m1}-\omega_{m0}+\omega_S)t}}{\omega_{m1}-\omega_{m0}+\omega_S} - \frac{E_S}{\omega_{m1}-\omega_{m0}+\omega_S} \\
&+ \frac{E_S^* e^{i(\omega_{m1}-\omega_{m0}-\omega_S)t}}{\omega_{m1}-\omega_{m0}-\omega_S} - \frac{E_S^*}{\omega_{m1}-\omega_{m0}-\omega_S}\Big) \\
&+ \frac{1}{\hbar}\mu_{m0}Q_{10}\Big(\\
&\frac{E_L e^{i(\omega_{m1}+\omega_{10}+\omega_L)t}}{\omega_{m1}+\omega_{10}+\omega_L} - \frac{E_L}{\omega_{m1}+\omega_{10}+\omega_L} \\
&+ \frac{E_L^* e^{i(\omega_{m1}+\omega_{10}-\omega_L)t}}{\omega_{m1}+\omega_{10}-\omega_L} - \frac{E_L^*}{\omega_{m1}+\omega_{10}-\omega_L} \\
&+ \frac{E_S e^{i(\omega_{m1}+\omega_{10}+\omega_S)t}}{\omega_{m1}+\omega_{10}+\omega_S} - \frac{E_S}{\omega_{m1}+\omega_{10}+\omega_S} \\
&+ \frac{E_S^* e^{i(\omega_{m1}+\omega_{10}-\omega_S)t}}{\omega_{m1}+\omega_{10}-\omega_S} - \frac{E_S^*}{\omega_{m1}+\omega_{10}-\omega_S}\Big)
\end{aligned}
\tag{B.29}
$$

Integration of equation B.25 after setting $n_m = 0$, gives:

$$
\begin{aligned}
Q_{m1}(t) = Q_{m1}(0) &+ \frac{1}{\hbar}\mu_{1m} n_1 \Big(\\
&\frac{E_L e^{-i(\omega_{m1}-\omega_L)t}}{\omega_{m1}-\omega_L} - \frac{E_L}{\omega_{m1}-\omega_L} \\
&+ \frac{E_L^* e^{-i(\omega_{m1}+\omega_L)t}}{\omega_{m1}+\omega_L} - \frac{E_L^*}{\omega_{m1}+\omega_L} \\
&+ \frac{E_S e^{-i(\omega_{m1}-\omega_S)t}}{\omega_{m1}-\omega_S} - \frac{E_L}{\omega_{m1}-\omega_S} \\
&+ \frac{E_S^* e^{-i(\omega_{m1}+\omega_S)t}}{\omega_{m1}+\omega_S} - \frac{E_L^*}{\omega_{m1}+\omega_S} \Big) \\
&- \frac{1}{\hbar}\mu_{10} Q_{m0} \Big(\\
&\frac{E_L e^{-i(\omega_{m1}-\omega_{m0}-\omega_L)t}}{\omega_{m1}-\omega_{m0}-\omega_L} - \frac{E_L}{\omega_{m1}-\omega_{m0}-\omega_L} \\
&+ \frac{E_L^* e^{-i(\omega_{m1}-\omega_{m0}+\omega_L)t}}{\omega_{m1}-\omega_{m0}+\omega_L} - \frac{E_L^*}{\omega_{m1}-\omega_{m0}+\omega_L} \\
&+ \frac{E_S e^{-i(\omega_{m1}-\omega_{m0}-\omega_S)t}}{\omega_{m1}-\omega_{m0}-\omega_S} - \frac{E_S}{\omega_{m1}-\omega_{m0}-\omega_S} \\
&+ \frac{E_S^* e^{-i(\omega_{m1}-\omega_{m0}+\omega_S)t}}{\omega_{m1}-\omega_{m0}+\omega_S} - \frac{E_S^*}{\omega_{m1}-\omega_{m0}+\omega_S} \Big) \\
&+ \frac{1}{\hbar}\mu_{0m} Q_{01} \Big(\\
&\frac{E_L e^{-i(\omega_{m1}+\omega_{10}-\omega_L)t}}{\omega_{m1}+\omega_{10}-\omega_L} - \frac{E_L}{\omega_{m1}+\omega_{10}-\omega_L} \\
&+ \frac{E_L^* e^{-i(\omega_{m1}+\omega_{10}+\omega_L)t}}{\omega_{m1}+\omega_{10}+\omega_L} - \frac{E_L^*}{\omega_{m1}+\omega_{10}+\omega_L} \\
&+ \frac{E_S e^{-i(\omega_{m1}+\omega_{10}-\omega_S)t}}{\omega_{m1}+\omega_{10}-\omega_S} - \frac{E_S}{\omega_{m1}+\omega_{10}-\omega_S} \\
&+ \frac{E_S^* e^{-i(\omega_{m1}+\omega_{10}+\omega_S)t}}{\omega_{m1}+\omega_{10}+\omega_S} - \frac{E_S^*}{\omega_{m1}+\omega_{10}+\omega_S} \Big) \Big)
\end{aligned}
\tag{B.30}
$$

Now those results can be inserted into equations B.18, B.19, B.20 and B.21. Then the equation B.18. becomes:

$$\begin{aligned} d_t n_0 = \Gamma_1 n_1 - \Gamma_0 n_0 + \frac{i}{\hbar} E(\mu_{10} Q_{10} e^{i\omega_{10} t} - \mu_{01} Q_{01} e^{-i\omega_{10} t}) \\ + \frac{i}{\hbar} E \sum_m \left(\mu_{m0} Q_{m0} e^{i\omega_{m0} t} - \mu_{0m} Q_{0m} e^{-i\omega_{m0} t}\right) \end{aligned} \tag{B.31}$$

By retaining only the terms that do not oscillate[2], one gets:

$$\begin{aligned} d_t n_0 = \Gamma_1 n_1 - \Gamma_0 n_0 + \frac{i}{\hbar} \sum_m \mu_{m0} \Big(\\ - \frac{1}{\hbar} \mu_{0m} n_0 \Big(\frac{|E_L|^2}{\omega_{m0} - \omega_L} + \frac{|E_L|^2}{\omega_{m0} + \omega_L} + \frac{|E_S|^2}{\omega_{m0} - \omega_S} + \frac{|E_S|^2}{\omega_{m0} + \omega_S} \Big) \\ - \frac{1}{\hbar} \mu_{1m} Q_{10} \Big(\frac{E_S E_L^*}{\omega_{m0} - \omega_{10} - \omega_S} + \frac{E_L^* E_S}{\omega_{m0} - \omega_{10} + \omega_L} \Big) \Big) \\ - \mu_{0m} \Big(\\ - \frac{1}{\hbar} \mu_{m0} n_0 \Big(\frac{|E_L|^2}{\omega_{m0} + \omega_L} + \frac{|E_L|^2}{\omega_{m0} - \omega_L} + \frac{|E_S|^2}{\omega_{m0} + \omega_S} + \frac{|E_S|^2}{\omega_{m0} - \omega_S} \Big) \\ - \frac{1}{\hbar} \mu_{m1} Q_{01} \Big(\frac{E_L E_S^*}{\omega_{m0} - \omega_{10} + \omega_L} + \frac{E_S^* E_L}{\omega_{m0} - \omega_{10} - \omega_S} \Big) \Big) \end{aligned} \tag{B.32}$$

The terms proportional to $|E_L|^2$ and $|E_S|^2$ or, at the same time, to $\mu_{0m}\mu_{m0}$ sum up to zero and if the equality $\omega_L = \omega_S + \omega_{10}$ is used, equation B.32.

[2]here $\frac{i}{\hbar} E(\mu_{10} Q_{10} e^{i\omega_{10} t} - \mu_{01} Q_{01} e^{-i\omega_{10} t})$ would correspond to infrared absorption if E would contain a component oscillating at frequency ω_{10}

becomes:

$$\begin{aligned} d_t n_0 &= \Gamma_1 n_1 - \Gamma_0 n_0 \\ &- \frac{i}{\hbar}\sum_m \frac{1}{\hbar}\mu_{1m}\mu_{m0}Q_{10}E_S E_L^*\Big(\frac{1}{\omega_{m0}-\omega_L}+\frac{1}{\omega_{m0}+\omega_S}\Big) \\ &+ \frac{i}{\hbar}\sum_m \frac{1}{\hbar}\mu_{0m}\mu_{m1}Q_{01}E_L E_S^*\Big(\frac{1}{\omega_{m0}-\omega_L}+\frac{1}{\omega_{m0}+\omega_S}\Big) \end{aligned} \tag{B.33}$$

or

$$d_t n_0 = \Gamma_1 n_1 - \Gamma_0 n_0 + \frac{i}{\hbar}\left(K_{01}Q_{01}E_L E_S^* - K_{10}Q_{10}E_S E_L^*\right) \tag{B.34}$$

if

$$K_{kl} = \frac{1}{\hbar}\sum_m \mu_{km}\mu_{ml}\left(\frac{1}{\omega_{m0}-\omega_L}+\frac{1}{\omega_{m0}+\omega_s}\right) \tag{B.35}$$

is defined. The same way, with use of relation $\omega_{m0} = \omega_{m1} + \omega_{10}$, equation B.19. becomes:

$$d_t n_1 = -\Gamma_1 n_1 + \frac{i}{\hbar}\left(K_{10}Q_{10}E_L^* E_S - K_{01}Q_{01}E_L E_S^*\right). \tag{B.36}$$

And by retaining only the terms that do not oscillate in equation B.20 one obtains:

$$\begin{aligned} d_t Q_{01} &= i\sum_m \frac{1}{\hbar}\mu_{m0}\Big(-\frac{1}{\hbar}\mu_{1m}n_1\Big(\frac{E_L^*E_S}{\omega_{m1}+\omega_L}+\frac{E_S E_L^*}{\omega_{m1}-\omega_s}\Big)\Big) \\ &- \frac{1}{\hbar}\mu_{1m}\Big(-\frac{1}{\hbar}\mu_{m0}n_0\Big(\frac{E_L^*E_S}{\omega_{m0}-\omega_L}+\frac{E_S E_L^*}{\omega_{m0}+\omega_s}\Big)\Big) \end{aligned} \tag{B.37}$$

or:

$$d_t Q_{01} = -iE_L^* E_S \left(n_1 - n_0\right) \sum_m \left(\frac{1}{\hbar}\right)^2 \mu_{1m}\mu_{m0} \left(\frac{1}{\omega_{m0} - \omega_L} + \frac{1}{\omega_{m0} + \omega_s}\right) \tag{B.38}$$

or finally:

$$d_t Q_{01} = -\frac{i}{\hbar} E_L^* E_S \left(n_1 - n_0\right) K_{10}, \tag{B.39}$$

Finally the system of equations for the two vibrational levels systems is:

$$\begin{aligned} d_t n_0 &= \Gamma_1 n_1 - \Gamma_0 n_0 + \frac{i}{\hbar}\left(K_{01} Q_{01} E_L E_S^* - K_{10} Q_{10} E_S E_L^*\right) \\ d_t n_1 &= -\Gamma_1 n_1 + \frac{i}{\hbar}\left(K_{10} Q_{10} E_L^* E_S - K_{01} Q_{01} E_L E_S^*\right) \\ d_t Q_{01} &= -\gamma_{01} Q_{01} - \frac{i}{\hbar} E_L^* E_S \left(n_1 - n_0\right) K_{10} \end{aligned} \tag{B.40}$$

B.3 Polarization

The equation 3.25. for the polarization can be expanded using equations B.28, B.30, B.27. and B.29.:

$$\begin{aligned} P_S(t) = \frac{1}{\hbar} \sum_m \Bigg(& \frac{\mu_{0m}\mu_{m0} n_0 E_S}{\omega_{m0} - \omega_S} + \frac{\mu_{1m}\mu_{m1} n_1 E_S}{\omega_{m1} + \omega_S} \\ & + \frac{\mu_{0m}\mu_{m0} n_0 E_S}{\omega_{m0} + \omega_S} + \frac{\mu_{0m}\mu_{m1} Q_{01} E_L}{\omega_{m0} - \omega_{10} + \omega_L} \\ & + \frac{\mu_{1m}\mu_{m1} n_1 E_S}{\omega_{m1} - \omega_S} + \frac{\mu_{0m}\mu_{m1} Q_{01} E_L}{\omega_{m1} + \omega_{10} - \omega_L} \Bigg) \end{aligned} \tag{B.41}$$

By neglecting the terms corresponding to the refraction (linear polarization proportional to E_S) one gets:

$$\begin{aligned} P_S(t) &= Q_{01}E_L \sum_m \frac{\mu_{0m}\mu_{m1}}{\hbar}\left(\frac{1}{\omega_{m0}+\omega_S}+\frac{1}{\omega_{m0}-\omega_L}\right) \\ &= K_{01}Q_{01}E_L \end{aligned} \tag{B.42}$$

and:

$$P_S^*(t) = K_{10}Q_{10}E_L^*. \tag{B.43}$$

B.4 Wave equation

The wave equation for electric field E in medium with refractive index n and nonlinear polarization P is:

$$\left(\nabla^2 - \frac{n^2}{c^2}\partial_t^2\right)E = \mu_0\partial_t^2 P \tag{B.44}$$

if amplitudes E_0 and P_0 are introduced the wave equation becomes:

$$\left(\nabla^2 - \frac{n^2}{c^2}\partial_t^2\right)E_0 e^{i(kz-\omega t)} = \mu_0\partial_t^2 P_0 e^{i(kz-\omega t)}, \tag{B.45}$$

where ω is the reference frequency and $k = \frac{\omega n}{c}$ is the wavevector. If a plane wave approximation is applied ($\nabla^2 = \partial_z^2$) above equation becomes:

$$\begin{aligned} \partial_z^2 E_0 - 2ik\partial_z E_0 - k^2 E_0 - \frac{n^2}{c^2}\left(\partial_t^2 E_0 + 2i\omega\partial_t E_0 - \omega^2 E_0\right) \\ = \mu_0\left(\partial_t^2 P_0 + 2i\omega\partial_t P_0 - \omega^2 P_0\right) \end{aligned} \tag{B.46}$$

If E_0 and P_0 are slowly varying in time and space: $|\partial_z E_0| << kE_0$, $|\partial_t E_0| << \omega E_0$, $|P_{0,t}| << \omega P_0$, the equation for the envelopes becomes:

$$\left(\partial_z + \frac{n}{c}\partial_t\right) E_0 = -i\frac{\mu_0}{2k}\omega^2 P_0 \tag{B.47}$$

additionally, if field over a single molecule is of interest the spatial dependence is small ($\partial_z E_0 \approx 0$), then:

$$\partial_t E_0 = -i\frac{\omega}{2\epsilon_0 n^2} P_0. \tag{B.48}$$

Solution of the above equation for $P_S(t) = K_{01}Q_{01}E_L$ is:

$$E_0(t) = E_0(0) - i\frac{\omega}{2\epsilon_0 n^2} K_{01}\int_0^t Q_{01}E_L dt' = E_0(0) + B(t), \tag{B.49}$$

where

$$B(t) = -i\frac{\omega}{2\epsilon_0 n^2} K_{01}\int_0^t Q_{01}E_L dt'. \tag{B.50}$$

The Stimulated Raman signal:

$$S'_{SRS} = \frac{I_{pump\ on} - I_{pump\ off}}{I_{pump\ off}} = \frac{I(t) - I(0)}{I(0)} \tag{B.51}$$

it is gathered by an integrating detector thus $I(t) \approx I(\infty)$:

$$S_{SRS} \approx \frac{I(\infty) - I(0)}{I(0)} \tag{B.52}$$

approximately:

$$I(\infty)\ |E_0(\infty)|^2 \approx |E_0(0)|^2 + 2|E_0(0)|B(\infty) = I(0) + 2|E_0(0)|B(\infty) \tag{B.53}$$

where B^2 was neglected, and $I(0) = |E_0(0)|^2$ Thus finally:

$$S_{SRS} = \frac{2B(\infty)}{|E_0(0)|} \tag{B.54}$$

For $P_S(t) = -iD_{10}|E_L|^2 E_S(n_1 - n_0)$:

$$E_0(t) = E_0(0) - \int_0^t \frac{\omega}{2\epsilon_0 n^2} D_{10}|E_L|^2(n_1 - n_0)E_S dt', \tag{B.55}$$

then $B(t)$ in equation B.54. is:

$$B(t) = -\int_0^t \frac{\omega}{2\epsilon_0 n^2} D_{10}|E_L|^2(n_1 - n_0)E_S dt'. \tag{B.56}$$

Bibliography

[1] G. Eckhardt, R. Hellwarth, F. McClung, S. Schwarz, D. Weiner, and E. Woodbury, "Stimulated Raman Scattering From Organic Liquids," Physical Review Letters **9**, 455–457 (1962).

[2] R. Hellwarth, "Theory of Stimulated Raman Scattering," Physical Review **130**, 1850–1852 (1963).

[3] S. De Silvestri, J. Fujimoto, E. Ippen, E. B. Gamble, L. R. Williams, and K. A. Nelson, "Femtosecond time-resolved measurements of optic phonon dephasing by impulsive stimulated raman scattering in α-perylene crystal from 20 to 300 K," Chemical Physics Letters **116**, 146–152 (1985).

[4] Y.-X. Yan, E. B. Gamble, and K. A. Nelson, "Impulsive stimulated scattering: General importance in femtosecond laser pulse interactions with matter, and spectroscopic applications," The Journal of Chemical Physics **83**, 5391 (1985).

[5] M. Born and K. Huang, *Dynamical Theory of crystal lattices* (Clarendon Press, Oxford, 1962), 2nd ed.

[6] B. Ratajska-Gadomska, "Influence of the interaction between dipoles, optically induced in a crystal lattice, on the nonlinear refractive index of crystals," Physical Review B **26**, 1942–1958 (1982).

[7] J. D. Jackson, *Classical Electrodynamics* (John Wiley, New York, 1962), 1st ed.

[8] W. Demtröder, *Laser Spectroscopy Basic Concepts and Instrumentation* (Springer-Verlag, Warsaw, 1993), 3rd ed.

[9] D. J. Griffiths, *Introduction to Electrodynamics* (Prentice Hall, New Jersey, 1999), 3rd ed.

[10] L. F. Mollenauer and J. C. White, *Topics in Applied Physics: Tunable Lasers* (Springer-Verlag, Berlin, 1987), 1st ed.

[11] R. Merlin, "Generating coherent THz phonons with light pulses," Solid State Communications **102**, 207–220 (1997).

[12] G. Garrett, T. Albrecht, J. Whitaker, and R. Merlin, "Coherent THz Phonons Driven by Light Pulses and the Sb Problem: What is the Mechanism?" Physical Review Letters **77**, 3661–3664 (1996).

[13] I. Harald, *A Modern Approach to Classical Mechanics* (World Scientific Pub Co Inc, Singapore, 2002), 1st ed.

[14] G. Placzek, *In Marx Handbuch der Radiologie* (Akademische Verlagsgesellschaft, Leipzig, 1934).

[15] R. A. Bartels, S. Backus, M. M. Murnane, and H. C. Kapteyn, "Impulsive stimulated Raman scattering of molecular vibrations using nonlinear pulse shaping," Chemical Physics Letters **374**, 326–333 (2003).

[16] K. Ishioka, M. Hase, M. Kitajima, and H. Petek, "Coherent optical phonons in diamond," Applied Physics Letters **89**, 231916 (2006).

[17] A. Nazarkin and G. Korn, "Raman self-conversion of femtosecond laser pulses and generation of single-cycle radiation," Physical Review A **58**, R61–R64 (1998).

[18] B. Ratajska-Gadomska, W. Gadomski, P. Wiewior, and C. Radzewicz, "A femtosecond snapshot of crystalline order in molecular liquids," The Journal of Chemical Physics **108**, 8489 (1998).

[19] W. J. Jones and B. P. Stoicheff, "Inverse Raman spectra: Induced absorption at optical frequencies," Phys. Rev. Lett. **13**, 657–659 (1964).

[20] B. Stoicheff, "Characteristics of stimulated raman radiation generated by coherent light," Physics Letters **7**, 186–188 (1963).

[21] A. Cheung, D. Rank, R. Chiao, and C. Townes, "Phase Modulation of Q-Switched Laser Beams in Small-Scale Filaments," Physical Review Letters **20**, 786–789 (1968).

[22] T. Gustafson, J. Taran, H. Haus, J. Lifsitz, and P. Kelley, "Self-Modulation, Self-Steepening, and Spectral Development of Light in Small-Scale Trapped Filaments," Physical Review **177**, 306–313 (1969).

[23] F. Shimizu, "Frequency Broadening in Liquids by a Short Light Pulse," Physical Review Letters **19**, 1097–1100 (1967).

[24] R. Alfano and S. L. Shapiro, "Emission in the region 4000 to 7000 A via four-photon coupling in glass," Physical Review Letters **24**, 584–588 (1970).

[25] R. R. Alfano and S. L. Shapiro, "Observation of self-phase modulation and small-scale filaments in crystals and glasses," Physical Review Letters **24**, 592 (1970).

[26] R. Brewer, "Frequency Shifts in Self-Focused Light," Physical Review Letters **19**, 8–10 (1967).

[27] N. Bloembergen and P. Lallemand, "Complex Intensity-Dependent Index of Refraction, Frequency Broadening of Stimulated Raman Lines, and Stimulated Rayleigh Scattering," Physical Review Letters **16**, 81–84 (1966).

[28] J. Marburger, "Self-focusing: Theory," Progress in Quantum Electronics **4**, 35–110 (1975).

[29] Y. Shen, "Self-focusing: Experimental," Progress in Quantum Electronics **4**, 1–34 (1975).

[30] C. Lin, V. Nguyen, and W. French, "Wideband near-I.R. continuum (0.7-2.1 ÎĽm) generated in low-loss optical fibres," Elect. Lett. **14**, 822–823 (1978).

[31] R. R. Alfano, P. L. Baldeck, F. Raccah, and P. P. Ho, "Cross phase modulation measured in optical fibers." Applied optics **26**, 3491–2 (1987).

[32] G. P. Agraval, *Nonlinear Fiber Optics* (Academic Press, San Diego, 2001), 3rd ed.

[33] R. R. Alfano, *The Supercontinuum Laser Source* (Springer-Verlag, New York, 2006), 2nd ed.

[34] J. Manassah, M. Mustafa, and R. Alfano, "Spectral extent and pulse shape of the supercontinuum for ultrashort laser pulse," IEEE Journal of Quantum Electronics **22**, 197–204 (1986).

[35] J. T. Manassah, R. R. Alfano, and M. Mustafa, "Spectral distribution of an ultrafast supercontinuum laser source," Physics Letters A **107**, 305–309 (1985).

[36] G. Yang and Y. R. Shen, "Spectral broadening of ultrashort pulses in a nonlinear medium," Optics Letters **9**, 510 (1984).

[37] B. Gross and J. T. Manassah, "Supercontinuum in the anomalous group-velocity dispersion region," Journal of the Optical Society of America B **9**, 1813–1818 (1992).

[38] N. Bloembergen, "The influence of electron plasma formation on superbroadening in light filaments," Optics Communications **8**, 285–288 (1973).

[39] M. Mlejnek, E. M. Wright, and J. V. Moloney, "Dynamic spatial replenishment of femtosecond pulses propagating in air." Optics letters **23**, 382–384 (1998).

[40] A. L. Gaeta, "Catastrophic collapse of ultrashort pulses," Physical review letters **84**, 3582–3585 (2000).

[41] J. R. Gulley and W. M. Dennis, "Ultrashort-pulse propagation through free-carrier plasmas," Physical Review A **81**, 033818 (2010).

[42] S. Jin, "A Fast Method in Simulations of Supercontinuum Generation in Photonic Crystal Fibers," Ph.D. thesis, Concordia University Montreal,Quebec, Canada (2005).

[43] F. Silva, D. R. Austin, A. Thai, M. Baudisch, M. Hemmer, D. Faccio, A. Couairon, and J. Biegert, "Multi-octave supercontinuum generation

from mid-infrared filamentation in a bulk crystal." Nature communications **3**, 807 (2012).

[44] N. Y. Vislobokov and A. P. Sukhorukov, "Supercontinuum generation by ultra-high power femtosecond laser pulses in dielectrics," Physics of Wave Phenomena **17**, 11–14 (2009).

[45] A. Q. Wu, I. H. Chowdhury, and X. Xu, "Femtosecond laser absorption in fused silica: Numerical and experimental investigation," Physical Review B **72**, 085128 (2005).

[46] P. Whalen, J. V. Moloney, A. C. Newell, K. Newell, and M. Kolesik, "Optical shock and blow-up of ultrashort pulses in transparent media," Physical Review A **86**, 033806 (2012).

[47] R. H. Stolen and I. E. P., "Raman gain in glass optical waveguides," Applied Physics Letters **22**, 276 (1973).

[48] J.-P. M. Feve, K. E. Shortoff, M. J. Bohn, and J. K. Brasseur, "High average power diamond Raman laser." Optics express **19**, 913–22 (2011).

[49] M. Zhi, X. Wang, and A. V. Sokolov, "Broadband coherent light generation in diamond driven by femtosecond pulses." Optics express **16**, 12139–47 (2008).

[50] N. Akozbek, M. Scalora, C. M. Bowden, and S. L. Chin, "White-light continuum generation and filamentation during the propagation of ultra-short laser pulses in air," Optics Communications **191**, 353–362 (2001).

[51] C. Brée, A. Demircan, and G. Steinmeyer, "Saturation of the All-Optical Kerr Effect," Physical Review Letters **106**, 183902 (2011).

[52] T. M. Kardaś, B. Ratajska-Gadomska, W. Gadomski, A. Lapini, and R. Righini, "The role of stimulated Raman scattering in supercontinuum generation in bulk diamond," Optics Express **21**, 24201 (2013).

[53] A. Brodeur and S. L. Chin, "Ultrafast white-light continuum generation and self-focusing in transparent condensed media," Journal of the Optical Society of America B **16**, 637–650 (1999).

[54] M. Bradler, P. Baum, and E. Riedle, "Femtosecond continuum generation in bulk laser host materials with sub-μJ pump pulses," Applied Physics B **97**, 561–574 (2009).

[55] A. Brodeur and S. L. Chin, "Band-Gap Dependence of the Ultrafast White-Light Continuum," Physical Review Letters **80**, 4406–4409 (1998).

[56] G. Arisholm, "second-order nonlinear interactions in birefringent media," JOSA B. **14**, 2543–2549 (1997).

[57] T. Brabec and F. Krausz, "Nonlinear Optical Pulse Propagation in the Single-Cycle Regime," Physical Review Letters **78**, 3282–3285 (1997).

[58] M. Kolesik and J. V. Moloney, "Nonlinear optical pulse propagation simulation: From Maxwell's to unidirectional equations," Physical Review E **70**, 036604 (2004).

[59] M. Kolesik, J. V. Moloney, and M. Mlejnek, "Unidirectional Optical Pulse Propagation Equation," Physical Review Letters **89**, 283902 (2002).

[60] M. Trippenbach, W. Wasilewski, P. Kruk, G. W. Bryant, G. Fibich, and Y. Band, "An improved nonlinear optical pulse propagation equation," Optics Communications **210**, 385–391 (2002).

[61] R. Ghosh, J. A. Mondal, and D. K. Palit, "Ultrafast dynamics of the excited states of curcumin in solution." The journal of physical chemistry. B **114**, 12129–43 (2010).

[62] W. E. Schiesser and G. W. Griffiths, *A Compedium of Partial Differential Equation Models: Method of Lines Analysis with Matlab* (Cambridge University Press, New York, 2009), 1st ed.

[63] Y. Xiao, D. N. Maywar, and G. P. Agrawal, "Time-transformation approach to pulse propagation in nonlinear dispersive media: Inclusion of delayed Raman nonlinearity," Physical Review A **87**, 063816 (2013).

[64] Y. Xiao, D. N. Maywar, and G. P. Agrawal, "New approach to pulse propagation in nonlinear dispersive optical media," Journal of the Optical Society of America B **29**, 2958 (2012).

[65] M. Matuszewski, W. Wasilewski, M. Trippenbach, and Y. Band, "Self-consistent treatment of the full vectorial nonlinear optical pulse propagation equation in an isotropic medium," Optics Communications **221**, 337–351 (2003).

[66] M. D. Feit, "Effect of refraction on spot-size dependence of laser-induced breakdown," Applied Physics Letters **24**, 169 (1974).

[67] M. R. Junnarkar, "Short pulse propagation in tight focusing conditions," Optics Communications **195**, 273–292 (2001).

[68] G. Ghosh, *Handbook of Optical Constants of Solids: Handbook of Thermo-Optic Coefficients of Optical Materials with ApplicationsÂ (Google eBook)* (Academic Press, 1998).

[69] R. R. Alfano and S. L. Shapiro, "Direct distortion of electronic clouds of rare-gas atoms in intense electric fields," Physical Review Letters **24**, 1217 (1970).

[70] V. Loriot, E. Hertz, O. Faucher, and B. Lavorel, "Measurement of high order Kerr refractive index of major air components." Optics express **17**, 13429–13434 (2009).

[71] V. L. Kalashnikov, E. Podivilov, A. Chernykh, S. Naumov, A. Fernandez, R. Graf, and A. Apolonski, "Approaching the microjoule frontier with femtosecond laser oscillators: theory and comparison with experiment," New Journal of Physics **7**, 217 (2005).

[72] A. M. Zheltikov, "Understanding the nonlinear phase and frequency shift of an ultrashort light pulse induced by an inertial third-order optical nonlinearity," Physical Review A **79**, 023823 (2009).

[73] M. D. Levenson and N. Bloembergen, "Dispersion of the nonlinear optical suseptibility tensor in centrosymmetric media," Physical Review B **10**, 4447–4463 (1974).

[74] K. Lee, B. J. Sussman, J. Nunn, V. Lorenz, K. Reim, D. Jaksch, I. Walmsley, P. Spizzirri, and S. Prawer, "Comparing phonon dephasing lifetimes in diamond using Transient Coherent Ultrafast Phonon Spectroscopy," Diamond and Related Materials **19**, 1289–1295 (2010).

[75] L. V. Keldysh, "Ionization in the field of a strong electromagnetic wave," J. Exptl. Theoret. Phys. **47**, 1945–1957 (1964).

[76] M. Lenzner, J. Krüger, S. Sartania, Z. Cheng, C. Spielmann, G. Mourou, W. Kautek, and F. Krausz, "Femtosecond Optical Breakdown in Dielectrics," Physical Review Letters **80**, 4076–4079 (1998).

[77] V. E. Gruzdev, "Analysis of the transparent-crystal ionization model developed by L V Keldysh*," Journal of Optical Technology **71**, 504–508 (2004).

[78] H. Löfås, A. Grigoriev, J. Isberg, and R. Ahuja, "Effective masses and electronic structure of diamond including electron correlation effects in first principles calculations using the GW-approximation," AIP Advances **1**, 032139 (2011).

[79] D. Gordon, "Vibronic spectra in diamond," J. Phys. C: Solid State Phys. **7**, 3797 (1974).

[80] V. M. Huxter, T. A. A. Oliver, D. Budker, and G. R. Fleming, "Vibrational and electronic dynamics of nitrogen-vacancy centers in diamond revealed by two-dimensional ultrafast spectroscopy," Nature Physics **9**, 744–749 (2013).

[81] B. Sapoval and C. Hermann, *Physics of semiconductors* (Springer, 2003).

[82] P. Ščajev, V. Gudelis, E. Ivakin, and K. Jarašiūnas, "Nonequilibrium carrier dynamics in bulk HPHT diamond at two-photon carrier generation," Physica Status Solidi (a) **208**, 2067–2072 (2011).

[83] J. P. Boyd, *Chebyshev and Fourier Spectral Methods* (DOVER Publications, Inc., 31 East 2nd Street Mineola, New York 11501, 2000), 2nd ed.

[84] A. E. Siegman, "Quasi fast Hankel transform." Optics letters **1**, 13–15 (1977).

[85] G. P. Agrawal and M. Lax, "End correction in the quasi-fast Hankel transform for optical propagation problems." Optics letters **6**, 171–3 (1981).

[86] M. Abramovitz and I. A. Stegun, *Handbook of Mathematical Functions* (United States Department of Commerce, 1972), tenth ed.

[87] O. V. Sinkin, R. Holzlöhner, J. Zweck, and C. R. Menyuk, "Optimization of the Split-Step Fourier Method in Modeling Optical-Fiber Communications Systems," Journal of Lightwave Technology **21**, 61–68 (2003).

[88] E. Hairer and G. Wanner, *Solving Ordinary Differential Equations II Stiff and Differential-Algebraic Problems* (Springer-Verlag, 1980).

[89] B. Schmidt, M. Hacker, G. Stobrawa, and T. Feurer, "Lab2-a virtual femtosecond laser lab," .

[90] T. Polívka and V. Sundstrom, "Ultrafast Dynamics of Carotenoid Excited States - From Solution to Natural and Artificial Systems," Chem. Rev. **104**, 2021–2071 (2004).

[91] H. A. Frank, A. J. Young, G. Britton, and R. J. Cogdell, *The Photochemistry of Carotenoids* (Kluwer Academic Publishers, New York, 1999), 2nd ed.

[92] H. J. Dutton, W. M. Manning, and B. M. Duggar, "Chlorophyll Fluorescence and Energy Transfer in the Diatom Nitzschia Closterium." The Journal of Physical Chemistry **47**, 308–313 (1943).

[93] K. Schulten and M. Karplus, "On the origin of a low-lying forbidden transition in polyenes and related molecules," Chemical Physics Letters **14**, 305–309 (1972).

[94] B. Hudson and B. Kohler, "A low-lying weak transition in the polyene α,ω-diphenyloctatetraene," Chemical Physics Letters **14**, 299–304 (1972).

[95] C.-P. Hsu, P. J. Walla, M. Head-Gordon, and G. R. Fleming, "The Role of the S 1 State of Carotenoids in Photosynthetic Energy Transfer: The Light-Harvesting Complex II of Purple Bacteria," J. Phys. Chem. B **105**, 11016–11025 (2001).

[96] L. Berkeley, V. Tassle, and A. Justin, "Lawrence Berkeley National Laboratory Excited State Structural Dynamics of Carotenoids and

Charge Transfer Systems by Aaron Justin Van Tassle B . S . (University of Illinois at Chicago) 2000 A dissertation submitted in partial satisfaction of the requir," (2006).

[97] Y. Pang, M. A. Prantil, A. J. V. Tassle, G. A. Jones, and G. R. Fleming, "Excited-State Dynamics of 8'-Apo-b-caroten-8'-al and 7',7'-Dicyano-7'-apo-b-carotene Studied by Femtosecond Time-Resolved Infrared Spectroscopy," J. Phys. Chem. B **113**, 13086–13095 (2009).

[98] Y. Pang and G. R. Fleming, "Branching relaxation pathways from the hot S(2) state of 8'-apo-beta-caroten-8'-al." Physical chemistry chemical physics : PCCP **12**, 6782–8 (2010).

[99] D. Zigmantas, T. Polívka, R. G. Hiller, A. Yartsev, and V. Sundström, "Spectroscopic and Dynamic Properties of the Peridinin Lowest Singlet Excited States," The Journal of Physical Chemistry A **105**, 10296–10306 (2001).

[100] M. Yoshizawa, H. Aoki, M. Ue, and H. Hashimoto, "Ultrafast relaxation kinetics of excited states in a series of mini- and macro-β-carotenes," Physical Review B **67**, 174302 (2003).

[101] M. Yoshizawa, R. Nakamura, O. Yoshimatsu, K. Abe, K. Nakagawa, R. Fujii, M. Nango, and H. Hashimoto, "Femtosecond stimulated Raman spectroscopy of the dark S 1 excited state of carotenoid in photosynthetic light harvesting complex *," Acta Biochimica Polonica **59**, 49–52 (2012).

[102] J. A. Bautista, R. E. Connors, B. B. Raju, R. G. Hiller, F. P. Sharples, D. Gosztola, M. R. Wasielewski, and H. a. Frank, "Excited State Properties of Peridinin:Â Observation of a Solvent Dependence of the Lowest Excited Singlet State Lifetime and Spectral Behavior Unique among Carotenoids," The Journal of Physical Chemistry B **103**, 8751–8758 (1999).

[103] D. Zigmantas, R. G. Hiller, A. Yartsev, and V. Sundström, "Dynamics of Excited States of the Carotenoid Peridinin in Polar Solvents : Dependence on Excitation Wavelength , Viscosity , and Temperature," J Phys Chem A. **107**, 5339–5348 (2003).

[104] M. Durchan, M. Fuciman, V. Sundström, and T. Polívka, "Excited-State Dynamics of Monomeric and Aggregated Carotenoid 8'-Apo-b-carotenal," The Journal of Physical Chemistry A **116**, 12330 (2012).

[105] E. E. Ostroumov, M. G. Müller, M. Reus, and A. R. Holzwarth, "On the nature of the "dark S*" excited state of β-carotene." The journal of physical chemistry. A **115**, 3698–712 (2011).

[106] A. E. Jailaubekov, M. Vengris, S.-H. Song, T. Kusumoto, H. Hashimoto, and D. S. Larsen, "Deconstructing the excited-state dynamics of β-carotene in solution." The journal of physical chemistry. A **115**, 3905–16 (2011).

[107] F. Ehlers, D. A. Wild, T. Lenzer, and K. Oum, "Investigation of the S1/ICT f S0 Internal Conversion Lifetime of 4'-apo-b-caroten-4'-al and 8'-apo-B-caroten-8'-al: Dependence on Conjugation Length and Solvent Polarity," J. Phys. Chem. A **111**, 2257–2265 (2007).

[108] M. Kopczynski, F. Ehlers, T. Lenzer, and K. Oum, "Evidence for an intramolecular charge transfer state in 12'-apo-beta-caroten-12'-al and 8'-apo-beta-caroten-8'-al: influence of solvent polarity and temperature." The journal of physical chemistry. A **111**, 5370–81 (2007).

[109] F. Ehlers, T. Lenzer, and K. Oum, "Excited-State Dynamics of 12'-Apo-b-caroten-12'-al and 8'-Apo-b-caroten-8'-al in Supercritical CO2,N2O, and CF3H," J. Phys. Chem. B **112**, 16690–16700 (2008).

[110] H. Nagae, M. Kuki, J.-P. Zhang, T. Sashima, Y. Mukai, and Y. Koyama, "Vibronic Coupling through the In-Phase, CdC Stretching Mode Plays a Major Role in the 2A," J Phys Chem A. **104**, 4155–4166 (2000).

[111] Z. He, D. Gosztola, Y. Deng, G. Gao, M. R. Wasielewski, and L. D. Kispert, "Effect of Terminal Groups, Polyene Chain Length, and Solvent on the First Excited Singlet States of Carotenoids," The Journal of Physical Chemistry B **104**, 6668–6673 (2000).

[112] G. Cerullo, G. Lanzani, M. Zavelani-Rossi, and S. De Silvestri, "Early events of energy relaxation in all-trans-β-carotene following sub-10 fs optical-pulse excitation," Physical Review B **63**, 1–4 (2001).

[113] R. Fujii, T. Inaba, Y. Watanabe, Y. Koyama, and J.-P. Zhang, "Two different pathways of internal conversion in carotenoids depending on the length of the conjugated chain," Chemical Physics Letters **369**, 165–172 (2003).

[114] E. Papagiannakis, D. S. Larsen, I. H. M. V. Stokkum, M. Vengris, and R. G. Hiller, "Accelerated Publications Resolving the Excited State Equilibrium of Peridinin in Solution," Bochemistry **43** (2004).

[115] D. Zigmantas, R. G. Hiller, F. P. Sharples, H. a. Frank, V. Sundström, and T. Polívka, "Effect of a conjugated carbonyl group on the photophysical properties of carotenoids," Physical Chemistry Chemical Physics **6**, 3009 (2004).

[116] P. Chábera, M. Fuciman, P. Hríbek, and T. Polívka, "Effect of carotenoid structure on excited-state dynamics of carbonyl carotenoids." Physical chemistry chemical physics : PCCP **11**, 8795–803 (2009).

[117] S. Akimoto, I. Yamazaki, T. Sakawa, and M. Mimuro, "Temperature Effects on Excitation Relaxation Dynamics of the Carotenoid -Carotene and Its Analogue -Apo-8'-carotenal , Probed by Femtosecond Fluorescence Spectroscopy," J Phys Chem A. **106**, 2237–2243 (2002).

[118] T. Buckup, J. Hauer, J. Möhring, and M. Motzkus, "Multidimensional spectroscopy of beta-carotene: vibrational cooling in the excited state." Archives of biochemistry and biophysics **483**, 219–23 (2009).

[119] T. Siebert, V. Engel, A. Materny, W. Kiefer, and M. Schmitt, "Probing the Kinetics of a Nonadiabatic Transition Initiating Out of Vibrationally Excited as Well as Ground State Modes with Femtosecond Time-Resolved Transient Gratings," The Journal of Physical Chemistry A **107**, 8355–8362 (2003).

[120] M. Sugisaki, K. Yanagi, R. Cogdell, and H. Hashimoto, "Unified explanation for linear and nonlinear optical responses in β-carotene: A sub-20-fs degenerate four-wave mixing spectroscopic study," Physical Review B **75**, 155110 (2007).

[121] M. Sugisaki, M. Fujiwara, K. Yanagi, R. J. Cogdell, and H. Hashimoto, "Four-wave mixing signals from beta-carotene and its n = 15 homologue." Photosynthesis research **95**, 299–308 (2008).

[122] M. Fujiwara, K. Yamauchi, M. Sugisaki, A. Gall, B. Robert, R. Cogdell, and H. Hashimoto, "Energy dissipation in the ground-state vibrational manifolds of β-carotene homologues: A sub-20-fs time-resolved transient grating spectroscopic study," Physical Review B **77**, 205118 (2008).

[123] T. Polívka and V. Sundström, "Dark excited states of carotenoids: Consensus and controversy," Chemical Physics Letters **477**, 1–11 (2009).

[124] T. R. Calhoun, J. A. Davis, M. W. Graham, and G. R. Fleming, "The separation of overlapping transitions in -carotene with broadband 2D electronic spectroscopy," Chemical Physics Letters **523**, 1–5 (2012).

[125] M. Yoshizawa and M. Kurosawa, "Femtosecond time-resolved Raman spectroscopy using stimulated Raman scattering," Physical Review A **61**, 013808 (1999).

[126] M. Yoshizawa and H. Aoki, "Vibrational relaxation of the 2A À g excited state in all-trans-b-carotene obtained by femtosecond time-resolved Raman spectroscopy," Physical Review B **63**, 1–4 (2001).

[127] D. W. McCamant, J. E. Kim, and R. A. Mathies, "Vibrational Relaxation in beta-Carotene Probed by Picosecond Stokes and Anti-Stokes Resonance Raman Spectroscopy." The journal of physical chemistry. A **106**, 6030–8 (2002).

[128] M. Kloz, R. van Grondelle, and J. T. M. Kennis, "Wavelength-modulated femtosecond stimulated Raman spectroscopy-approach towards automatic data processing." Physical chemistry chemical physics : PCCP **13**, 18123–33 (2011).

[129] S. Shim and R. A. Mathies, "Development of a tunable femtosecond stimulated raman apparatus and its application to beta-carotene." The journal of physical chemistry. B **112**, 4826–32 (2008).

[130] P. Kukura, D. W. Mccamant, and R. A. Mathies, "Femtosecond Time-Resolved Stimulated Raman Spectroscopy of the S2 (1Bu+) Excited State of b-Carotene," The Journal of Physical Chemistry A **108**, 5921–5925 (2004).

[131] T. Sashima, H. Nagae, M. Kuki, and Y. Koyama, "A new singlet-excited state of all-trans-spheroidene as detected by resonance-Raman excitation profiles," Chemical Physics Letters **299**, 187–194 (1999).

[132] K. Furuichi, T. Sashima, and Y. Koyama, "The first detection of the 3Ag- state in carotenoids using resonance-Raman excitation profiles," Chemical Physics Letters **356**, 547–555 (2002).

[133] C. C. Gradinaru, J. T. Kennis, E. Papagiannakis, I. H. van Stokkum, R. J. Cogdell, G. R. Fleming, R. A. Niederman, and R. van Grondelle, "An unusual pathway of excitation energy deactivation in carotenoids: singlet-to-triplet conversion on an ultrafast timescale in a photosynthetic antenna." Proceedings of the National Academy of Sciences of the United States of America **98**, 2364–9 (2001).

[134] P. Tavan and K. Schulten, "Electronic excitations," **36**, 4337–4358 (1987).

[135] M. Kleinschmidt, C. M. Marian, M. Waletzke, and S. Grimme, "Parallel multireference configuration interaction calculations on mini-beta-carotenes and beta-carotene." The Journal of chemical physics **130**, 044708 (2009).

[136] M. R. Wasielewski and L. D. Kispert, "Direct measurement of the lowest excited singlet state lifetime of all-trans-β-carotene and related carotenoids," Chemical Physics Letters **128**, 238–243 (1986).

[137] J.-P. Zhang, T. Inaba, Y. Watanabe, and Y. Koyama, "Excited-state dynamics among the 1Bu+, 1Bu- and 2Ag- states of all-trans-neurosporene as revealed by near-infrared time-resolved absorption spectroscopy," Chemical Physics Letters **332**, 351–358 (2000).

[138] G. Cerullo, D. Polli, G. Lanzani, S. De Silvestri, H. Hashimoto, and R. J. Cogdell, "Photosynthetic light harvesting by carotenoids: detection of an intermediate excited state." Science (New York, N.Y.) **298**, 2395–8 (2002).

[139] F. S. Rondonuwu, Y. Kakitani, H. Tamura, and Y. Koyama, "Singlet internal conversion processes in the order of in all-trans-spheroidene and lycopene as revealed by subpicosecond time-resolved Raman spectroscopy," Chemical Physics Letters **429**, 234–238 (2006).

[140] D. Polli, G. Cerullo, G. Lanzani, S. De Silvestri, K. Yanagi, H. Hashimoto, and R. Cogdell, "Conjugation Length Dependence of Internal Conversion in Carotenoids: Role of the Intermediate State," Physical Review Letters **93**, 163002 (2004).

[141] F. S. Rondonuwu, Y. Watanabe, R. Fujii, and Y. Koyama, "A first detection of singlet to triplet conversion from the 11Bu- to the 13Ag state and triplet internal conversion from the 13Ag to the 13Bu state in carotenoids: dependence on the conjugation length," Chemical Physics Letters **376**, 292–301 (2003).

[142] F. L. de Weerd, I. H. van Stokkum, and R. van Grondelle, "Subpicosecond dynamics in the excited state absorption of all-trans-β-Carotene," Chemical Physics Letters **354**, 38–43 (2002).

[143] H. Hörvin Billsten, D. Zigmantas, V. Sundström, and T. Polívka, "Dynamics of vibrational relaxation in the S1 state of carotenoids having 11 conjugated C=C bonds," Chemical Physics Letters **355**, 465–470 (2002).

[144] D. W. McCamant, P. Kukura, and R. A. Mathies, "Femtosecond Time-Resolved Stimulated Raman Spectroscopy: Application to the Ultrafast Internal Conversion in β-Carotene," J Phys Chem A. **107**, 8208–8214 (2003).

[145] D. Kosumi, M. Fujiwara, R. Fujii, R. J. Cogdell, H. Hashimoto, and M. Yoshizawa, "The dependence of the ultrafast relaxation kinetics of the S(2) and S(1) states in beta-carotene homologs and lycopene on conjugation length studied by femtosecond time-resolved absorption and Kerr-gate fluorescence spectroscopies." The Journal of chemical physics **130**, 214506 (2009).

[146] B. Ratajska-Gadomska and W. Gadomski, "Quantum theory of the vibronic solid-state laser," Journal of the Optical Society of America B **16**, 848 (1999).

[147] M. G. Raymer and J. Mostowski, "Stimulated Raman scattering: Unified treatment of spontaneous initiation and spatial propagation," Physical Review A **24**, 1980–93 (1981).

[148] S. Mukamel and J. D. Biggs, "Communication : Comment on the effective temporal and spectral resolution of impulsive stimulated Raman signals Communication : Comment on the effective temporal and spectral resolution of impulsive stimulated Raman signals," The Journal of chemical physics **134**, 161101 (2011).

[149] P. Kukura, D. W. McCamant, P. H. Davis, and R. A. Mathies, "Vibrational structure of the S2 (1Bu) excited state of diphenyloctatetraene observed by femtosecond stimulated Raman spectroscopy," Chemical Physics Letters **382**, 81–86 (2003).

[150] K. Niu, B. Zhao, Z. Sun, and S.-Y. Lee, "Analysis of femtosecond stimulated Raman spectroscopy of excited-state evolution in bacteriorhodopsin." The Journal of chemical physics **132**, 084510 (2010).

[151] P. Kukura, D. W. McCamant, S. Yoon, D. B. Wandschneider, and R. A. Mathies, "Structural observation of the primary isomerization in vision with femtosecond-stimulated Raman." Science (New York, N.Y.) **310**, 1006–9 (2005).

[152] A. L. Smeigh, M. Creelman, R. A. Mathies, and J. K. McCusker, "Femtosecond time-resolved optical and Raman spectroscopy of photoinduced spin crossover: temporal resolution of low-to-high spin optical switching." Journal of the American Chemical Society **130**, 14105–7 (2008).

[153] F. Han, W. Liu, and C. Fang, "Excited-state proton transfer of photoexcited pyranine in water observed by femtosecond stimulated Raman spectroscopy," Chemical Physics **422**, 204–219 (2013).

[154] W. Liu, F. Han, C. Smith, and C. Fang, "Ultrafast Conformational Dynamics of Pyranine during Excited State Proton Transfer in Aqueous Solution Revealed by Femtosecond Stimulated Raman Spectroscopy," The Journal of Physical Chemistry B (2012).

[155] R. R. Frontiera, S. Shim, and R. A. Mathies, "Origin of negative and dispersive features in anti-Stokes and resonance femtosecond stimulated Raman spectroscopy." The Journal of chemical physics **129**, 064507 (2008).

[156] S. Dobner, C. Cleff, C. Fallnich, and P. Groß, "Interferometric background reduction for femtosecond stimulated Raman scattering loss spectroscopy." The Journal of chemical physics **137**, 174201 (2012).

[157] M. Kloz, R. V. Grondelle, and J. T. Kennis, "Correction for the time dependent inner filter effect caused by transient absorption in femtosecond stimulated Raman experiment," Chemical Physics Letters **544**, 94–101 (2012).

[158] Z. Sun, B. Fu, D. H. Zhang, and S.-Y. Lee, "Theoretical investigation of the direct observation of anharmonic coupling in CDCl(3) in the time domain with femtosecond stimulated Raman scattering." The Journal of chemical physics **130**, 044312 (2009).

[159] B. Zhao, Z. Sun, and S.-Y. Lee, "Quantum theory of time-resolved femtosecond stimulated Raman spectroscopy : Direct versus cascade processes and application to Quantum theory of time-resolved femtosecond stimulated Raman spectroscopy : Direct versus cascade processes and application to C," The Journal of Chemical Physics **024307** (2011).

[160] S. Laimgruber, H. Schachenmayr, B. Schmidt, W. Zinth, and P. Gilch, "A femtosecond stimulated raman spectrograph for the near ultraviolet," Applied Physics B **85**, 557–564 (2006).

[161] K. C. Wilson, B. Lyons, R. Mehlenbacher, R. Sabatini, and D. W. McCamant, "Two-dimensional femtosecond stimulated Raman spectroscopy: Observation of cascading Raman signals in acetonitrile." The Journal of chemical physics **131**, 214502 (2009).

[162] B. Zhao, Z. Sun, and S.-Y. Lee, "Quantum theory of time-resolved femtosecond stimulated Raman spectroscopy: direct versus cascade processes and application to CDCl3." The Journal of chemical physics **134**, 024307 (2011).

[163] R. D. Mehlenbacher, B. Lyons, K. C. Wilson, Y. Du, and D. W. McCamant, "Theoretical analysis of anharmonic coupling and cascading

Raman signals observed with femtosecond stimulated Raman spectroscopy." The Journal of chemical physics **131**, 244512 (2009).

[164] E. Pontecorvo, C. Ferrante, C. G. Elles, and T. Scopigno, "Spectrally tailored narrowband pulses for femtosecond stimulated Raman spectroscopy in the range 330-750 nm." Optics express **21**, 6866–72 (2013).

[165] M. Nejbauer and C. Radzewicz, "Efficient spectral shift and compression of femtosecond pulses by parametric amplification of chirped light." Optics express **20**, 2136–42 (2012).

[166] S. Shim and R. A. Mathies, "Femtosecond Raman-induced Kerr effect spectroscopy," Journal of Raman Spectroscopy **39**, 1526–1530 (2008).

[167] E. Treacy, "Optical pulse compression with diffraction gratings," IEEE Journal of Quantum Electronics **5**, 454–458 (1969).

[168] G. Orlandi, F. Zerbetto, and M. Z. Zgierski, "Theoretical Analysis of Spectra of Short Polyenes," Chem. Rev. **91**, 867–891 (1991).

[169] M. G. Vivas, D. L. Silva, L. D. Boni, R. Zalesny, W. Bartkowiak, and C. R. Mendonca, "Two-photon absorption spectra of carotenoids compounds," Journal of Applied Physics **109**, 103529 (2011).

[170] A. Meyers Kelley, *Condensed-Phase Molecular Spectroscopy and Photophysics* (Wiley, New York, 2013).

[171] H. A. Frank, J. A. Bautista, J. Josue, Z. Pendon, R. G. Hiller, F. P. Sharples, D. Gosztola, and M. R. Wasielewski, "Effect of the Solvent Environment on the Spectroscopic Properties and Dynamics of the Lowest Excited States of Carotenoids," The Journal of Physical Chemistry B **104**, 4569–4577 (2000).

[172] H. M. Vaswani, C.-P. Hsu, M. Head-Gordon, and G. R. Fleming, "Quantum Chemical Evidence for an Intramolecular Charge-Transfer State in the Carotenoid Peridinin of Peridinin-Chlorophyll-Protein," The Journal of Physical Chemistry B **107**, 7940–7946 (2003).

[173] N. Tschirner, M. Schenderlein, K. Brose, E. Schlodder, M. A. Mroginski, P. Hildebrandt, and C. Thomsen, "Raman excitation profiles of β -carotene - novel insights into the nature of the ν1-band," Physica Status Solidi (B) **245**, 2225–2228 (2008).

[174] T. Noguchi, H. Hayashi, M. Tasumi, and G. H. Atkinson, "Solvent Effects on the ag C=C Stretching Mode in the 21Ag- Excited State of b-Carotene and Two Derivatives: Picosecond Time-Resolved Resonance Raman Spectroscopy," J. Phys. Chem. pp. 3167–3172 (1991).

[175] A. Lapini. Private communication.

[176] P. Atkins and J. de Paula, *Physical Chemistry* (W. H. Freeman and Company, 41 Madison Avenue, New York, NY 10010, 1999), eighth ed.

[177] Z. Sun, J. Lu, D. H. Zhang, and S.-Y. Lee, "Quantum theory of (femtosecond) time-resolved stimulated Raman scattering." The Journal of chemical physics **128**, 144114 (2008).

[178] K. Niu, S. Cong, and S.-Y. Lee, "Femtosecond stimulated Raman scattering for polyatomics with harmonic potentials: application to rhodamine 6G." The Journal of chemical physics **131**, 054311 (2009).

[179] Z. Sun, Z. Jin, J. Lu, D. H. Zhang, and S.-Y. Lee, "Wave packet theory of dynamic stimulated Raman spectra in femtosecond pump-probe spectroscopy." The Journal of chemical physics **126**, 174104 (2007).

[180] X. Qiu, X. Li, K. Niu, and S.-Y. Lee, "Femtosecond stimulated Raman spectroscopy modeled with a delta probe pulse: application to rhodamine 6G," Journal of Raman Spectroscopy **42**, 563–575 (2011).

[181] W. Zinth, H.-J. Polland, A. Laubereau, and W. Kaiser, "New results on ultrafast coherent excitation of molecular vibrations in liquids," Applied Physics B Photophysics and Laser Chemistry **26**, 77–88 (1981).

[182] I. Białonicki-Birula, M. Cieplak, and J. Kamiński, *Teoria kwantów* (PWN, Warszawa, 2001), 2nd ed.

[183] H. Haken, *Światło: fale, fotony, atomy* (Wydawnictwo Naukowe PWN,, 1993).

[184] P. Meystre and M. Sargent III, *Elements of Quantum Optics* (Springer-Verlag, Berlin Heidelberg, 2007), 4th ed.

[185] S. Williams and D. G. Imre, "Raman Spectroscopy : Time-Dependent Pictures," The Journal of chemical physics **95** (1988).

[186] M. Spanner and P. Brumer, "Two-pulse control of Raman scattering in liquid methanol: The dominance of classical nonlinear optical effects," Physical Review A **73**, 023810 (2006).

[187] OriginLab Corp., *Origin Reference v8*.

[188] J. T. Fourkas, H. Kawashima, and K. A. Nelson, "Theory of nonlinear optical experiments with harmonic oscillators," The Journal of Chemical Physics **103**, 4393 (1995).

[189] J.-P. Zhang, C.-H. Chen, Y. Koyama, and H. Nagae, "Vibrational Relaxation and Redistribution in the 2A g - State of all - trans -Lycopene As Revealed by Picosecond Time-Resolved Absorption Spectroscopy," The Journal of Physical Chemistry B **102**, 1632–1640 (1998).

[190] J.-P. Zhang, R. Fujii, Y. Koyama, and F. S. Rondonuwu, "The 1B u -type singlet state of b-carotene as a precursor of the radical cation found in chloroform solution by sub-picosecond time-resolved absorption spectroscopy," Chemical Physics Letters **348**, 235–241 (2001).

[191] S. Maruta, D. Kosumi, T. Horibe, R. Fujii, M. Sugisaki, R. Cogdell, and H. Hashimoto, "Unusual enhancement of triplet carotenoid formation in pigmentprotein complexes as revealed by femtosecond pump-probe spectroscopy," Physics Procedia **13**, 58–61 (2011).

[192] T. M. Kardaś, B. Ratajska-Gadomska, a. Lapini, E. Ragnoni, R. Righini, M. Di Donato, P. Foggi, and W. Gadomski, "Dynamics of the time-resolved stimulated Raman scattering spectrum in presence of transient vibronic inversion of population on the example of optically excited trans-β-apo-8'-carotenal." The Journal of chemical physics **140**, 204312 (2014).

[193] NVIDIA, http://www.nvidia.pl/, *NVIDIA CUDA getting started guide for Microsoft Windows*.

[194] K. Ahnert and M. Mulansky, *Boost Numeric Odeint library documentation*, http://www.boost.org/.

[195] K. Ahnert, M. Mulansky, D. Demidov, K. Rupp, and P. Gottschling, "Solving odes with cuda and opencl using boost.odeint," in "FOSDEM 2013," (2013).

[196] D. Demidov, K. Ahnert, K. Rupp, and P. Gottschling, "Programming CUDA and OpenCL: A Case Study Using Modern C++ Libraries," SIAM Journal of Scientific Computing **35** (2013).

[197] E. Hairer and G. Wanner, *Solving Ordinary Differential Equations I Nonstiff Problems* (Springer, 1993), 2nd ed.

[198] T. M. Kardaś, "Parallel implicit ordinary differential equation solver for cuda." .